Faculty of Engineering of the University of Porto

Analysis of metallic foams with meshless methods: a homogenisation technique

Damián González de Chávez Pérez

Thesis submitted to the Faculty of Engineering of the University of Porto as a requirement to obtain the MSc degree in Computational Mechanics.

Under the supervision of

Professor Jorge Américo Oliveira Pinto Belinha

and

Professor Renato Manuel Natal Jorge

Porto, September 2018

Abstract

This project aims to study and obtain the expressions that define the mechanical properties of an aluminium cell with different relative densities. The goal is to allow the extrapolation of these properties for large scale models, as a core, namely for sandwich structures.

Preliminary research was done to decide the lower level that composes the foam structure, that is, the cell. Regarding the objective of the thesis, there are four important questions that need to be answered. The first one is to know how the mechanical properties behave with the variation of the relative density. The second one, to compare the behaviour of FEM – a mesh-based method - with that of meshless methods such as RPIM, and NNRPIM, when applied under the same situations. Third, to compare the behaviour of the mechanical properties of a sandwich beam structure at different relative densities within its core. Fourth, to compare the results for a sandwich beam structure under increasing relative densities from the inside to the outside part of the beam, for each numerical method applied.

In order to obtain the behaviour of the aluminium cells, elastic and elastoplastic simulations were carried out, applying a displacement to the top of the cell and with the boundary conditions as being confined and non-confined. The beam case study employed the characteristics of a cantilever beam, meaning it was embedded on one end and with a displacement in the free end. The numerical simulations were performed using the FEM, RPIM, with two different formulations, and the NNRPIM.

The technique applied to obtain the mechanical properties was a '*homogenisation technique,*' that allows, with a simple procedure, to group all of the properties obtained in each node in a single property for all of the cellular solid. The results obtained using homegenisation were compared to those obtained using an interest point.

After 400 simulations, the graphics that represent the behaviour of Young's modulus, the tangent modulus and the Poisson's coefficient were produced as a function of the relative density for the confined and non-confined cases. Also, the yield stress was obtained as a function of the relative density. Through these graphics, it was possible to obtain the properties for a range of relative densities between 0.4 and 0.7. This property was applied in the core of the sandwich structure.

In view of the results, it was possible to conclude that the difference between the methods is not relevant. Furthermore, similarities between the FEM and the NNRPIM results and between the RPIM with the first and second formulation were observed. Also, having holes in the cell structure and treating it under meshed and no-meshed aproaches produces the same results.

The main conclusion reached was that the properties obtained in the interest point present better results than the ones obtained with the homogenisation technique.

The behaviour of the cases with relative densities outside the range between of 0.4 and 0.7 is considered undefined with the techniques used and the results obtained in this study.

Resumo

Este projecto pretende estudar e obter as expressões que definem as propriedades mecânicas de uma célula de alumínio com diferentes densidades relativas. A meta é permitir a extrapolação destas propriedades para modelos a uma escala maior, no seu interior, nomeadamente para estruturas tipo-sanduíche.

Após um trabalho preliminar de pesquisa, decidiu-se começar pelo nível mais baixo em termos da composição da estrutura da espuma, isto é, a célula.

No que respeita aos objectivos da tese, há quatro questões importantes às quais dar resposta. O primeiro consiste em saber como as propriedades mecânicas se comportam com a variação da densidade relativa. O segundo objectivo é comparar o comportamento dos métodos numéricos FEM, RPIM e NNRPIM, quando ulizados em situações idênticas. Em terceiro lugar, pretende-se comparar o comportamento das propriedades mecâncias de uma estrutura tipo sanduíche com difentes densidades relativas dentro do seu núcleo. O quarto objectivo é comparar os resultados para uma viga em sanduíche sob densidades relativas crescentes, do interior para o exterior e para cada método numérico aplicado.

Para se obter o comportamento das células de alumínio,foram realizadas simulações elásticas e elastoplásticas, aplicando-se um deslocamento no topo da célula, com condições – fronteira confinadas e não-confinadas. Para o estudo de caso com a viga de alumínio, foram utilizadas as características de uma viga cantiléver, isto é, embutida numa extremidade e com deslocamento na extremidade livre. As simulações numéricas foram realizadas utilizando os métodos FEM, o RPIM com duas formulações diferentes e o NNRPIM.

A técnica aplicada para se obterem as propriedasde mecânicas foi a da homogenização, que permite, com um procedimento simples, o agrupar de todas as propriedades obtidas para cada nó num única propriedade para a globalidade do sólido celular. Os resultados obtidos com a homogeneização foram comparados com os obtidos utilizando a abordagem ao ponto de interesse.

Após 400 simulações, os gráficos que representam o comportamento do Módulo de Young, do Módulo tangente e do Coeficiente de Poisson foram construídos em função da densidade relativa para os casos confinados e não-confinados. Além disso, a tensão de cedência foi obtida em função da densidade relativa. Através destes gráficos, foi possível obter-se as propriedades para uma gama de densidades relativas entre 0.4 e 0.7. Esta propriedade foi aplicada no núcleo da estrutura sanduíche.

Tendo em conta os resultados, foi possível concluir que a diferença entre os métodos utilizados não é relevante. Adicionalmente, observaram-se também semelhanças entre os resultados do FEM e do NNRPIM e entre ambas as formulações para o RPIM. Além disso, tratar uma estrutura celular com orifícios segundo uma abordagem com malha e sem malha produz os mesmos resultados.

A principal conclusão conseguida neste estudo foi a de que as propriedades obtidas através da abordagem ponto de interesse apresentam melhores resultados do que com a técnica da homogeneização.

Considera-se também que o comportamento dos casos em que as densidades relativas estão fora do intervalo 0.4 a 0.7 é indefinido com as técnicas utilizadas e para os resultados obtidos neste estudo.

Acknowledgements

To my parents, Male and Juan, who have supported me in the awkward moments, always showing me positivism and much love despite being separated by distance and knowing that it is never easy to be far from home.

A special acknowledgement to my supervisor, Professor Jorge Belinha who, from the beginning of the master awoke in me the interest for the study of computational mechanics and pushed me to improve myself, to overcome my obstacles and tobecome a more complete and autonomous person.

To my best friend since I arrived in Porto, Nina Costa, who always explained to me that she was available for anything I would need. For guiding me and showing me how the faculty worked and of course, for the great moments that we spent during breaks at work. Also, I would like to include Cecília Carvalho, who was as a big sister to me. also contributing to great moments at the faculty.

To my laboratory team, Bruno Areias, Edwin Ocana, Leonardo Santana, Marco Marques for their help, support and teaching me, while creating an enjoyable work atmosphere.

Finally, to my colleagues of the master programme, which also allowed me to improve and increase my skills through the knowledge absorbed form each one.

Institutional Acknowledgments and Funding

The author truly acknowledges the work conditions provided by the Applied Mechanics Division (SMAp) of the Department of Mechanical Engineering (DEMec) of the Faculty of Engineering of the University of Porto (FEUP), and by the MIT-Portugal project "MIT-EXPL/ISF/0084/2017", funded by Massachusetts Institute of Technology (USA) and "Ministério da Ciência, Tecnologia e Ensino Superior - Fundação para a Ciência e a Tecnologia" (Portugal).

Additionally, the authors gratefully acknowledge the funding of Project NORTE-01-0145-FEDER-000022 - SciTech - Science and Technology for Competitive and Sustainable Industries, cofinanced by Programa Operacional Regional do Norte (NORTE2020), through Fundo Europeu de Desenvolvimento Regional (FEDER).

Finally, the author acknowledges the synergetic collaboration with the Researchers of "Computational Mechanics Research Laboratory CMech-Lab" (ISEP/FEUP/INEGI), and its director, Prof. Dr. Jorge Belinha, and its senior advisors, Prof. Dr. Renato Natal Jorge and Prof. Dra. Lúcia Dinis.

Table of Contents

List of Figures

List of Tables

Chapter 1

INTRODUCTION

The study of cellular solid is nowadays one of the most relevant fields for study in the engineering world, because of its wide range of physical and mechanical properties. Having the possibility to understand and reproduce the internal structures of a few natural cellular solids, which combine a high rigidity with a low relative density (e.g.: trabecular bone, wood, cork, sponges, wools, honeycomb), is really important in order to understand why these types of structures occur in nature. The work presented herein follows the knowledge provided by Lorna J.Gibson and Michael F.Ashby, who have extensively studied the behaviour of the cellular solids (L. Gibson & Ashby, 1997).

Nowadays, cellular solids have been reproduced in many areas such as human prostheses, sandwich structures and also significant structures as building materials and components. In order to understand these structures, it is necessary to begin the study at the cellular level. Cells present many different forms: regular and repetitive as the honeycomb, or irregular and random as the trabecular bone. Also, they may be closed or open. The main aspect is that every single cellular form in nature has a reason to be. Engineering must apply its knowledge to answer the question as to why that is the case.

These types of structures require proper mathematical models capable of simulating their behaviour. This is where these types of materials present their most challenging aspect. Suitable numerical methods included the Finite Element Method (FEM), (Ziennkiewicz & Taylor, 2005) and the Radial Point Interpolator Method (RPIM) or Natural Neighbour Radial Point Interpolator Method (NNRPIM), both meshless methods (Jorge Belinha, 2014b). Their ability to discretise the geometry of cellular solids and their computational efficiency allows to reproduce the behaviour of these types of structures.

Because of the broad world that the cellular solids present, this project had to be limited to understanding one single cell geometry, with a simple shape as a circle. The work focused on, varying the size and the number of the circle to reproduce the variation of the relative density in the same specimen.

This work aims to fulfill two different objectives. First, to obtain the mathematical model that represents the mechanical behaviour of the cell geometry with the variation of relative density with the elastic behaviour and the elastoplastic behaviour.The second objective is to compare the differences in the results from applying different numerical methods - such as FEM, and meshless (RPIM/NNRPIM).

Taking into account the first objective, having the models that define the behaviour of the cellular solid allow to apply their properties to any geometry, having the possibility to change the relative density along the solid. Focusing on the second objective, it will be possible to verify whether the meshless method presents better results than the FEM, knowing that both meshless methods are more flexible with regards to the geometry, an aspect that is essential in these types of structures.

This work is composed of seven chapters:

- The **first chapter** correspond with the introduction, where the principal concepts of the thesis are announced.
- The **second chapter** presents the bibliographic review, where a few of the fabrication processes are explained. The chapter also addresses how the understanding of cellular solids behaviour has been evolving, given the appearance of new and more robust mathematical models and the discovery of new cell structures.
- The **third chapter** explains how the two types of numerical methods will be used. The chapter presents the FEM (Finite Element Method) and meshless methods -RPIM (Radial Point Interpolator Method) and NNRPIM (Natural Neighbour Radial Point Interpolator Method). The formulation behind both types opf methods will be presented.
- The **fourth chapter** presents the fundamentals of solid mechanics , addressing the strong and weak form formulation, the yield criteria (continuum solid and cellular solid) and the elastoplastic fundamentals, along with their formulation as well.
- The **fifth chapter** summarises the bibliographic review conducted for the numerical methods applied and highlights how nowadays these methods already contribute to the understanding of cellular solids behaviour.
- The **sixth chapter** describes how the model for this work was done, which boundary conditions were applied, the simulations that were performed and the results that were obtained for the elastic and elastoplastic studies together with the graphics and the expressions of the behaviour of the models.
- The **seventh chapter** presents the study of a sandwich panel, and the elastoplastic results for the different cores as a function of the relative density, presented through the force-displacement graphics.
- The **eighth chapter** presents the conclusions and recommendations for future work.

Chapter 2

CELLULAR SOLIDS

Cellular solids are a type of material that is characterised as such because of is internal structure: an assembly of porous cells with solid edges or faces, packed together so that they fill space. They have been known in their natural form for a very long time (trabecular bone, wood, cork, sponges, wools). These cells can be open or closed, and their dimensions can span over several order magnitudes, from nanometers to centimetres. Their microstructure has widely inspired engineers to produce highly porous engineering solids such as wool (glass or rock wool) and foam (metal, polymer and ceramic foams). Over the last 20-years, interest in these materials has grown. They have numerous interesting properties, qualifying them as multifunctional materials. Thanks to their low relative density and excellent mechanical properties, they can be uses as a lightweight sandwich core. Their high fracture strain, together with their damaging behaviour when compressed, induces a significant energy absorption capacity for packaging applications and shock absorbers. Their low thermal and acoustic conductivity are interesting for hear and sound insulation. The high-volume fraction of open porosity favours their use as filters and bone substitutes. Presently, these types of materials have a potential application in new fields, specifically in aeronautics and aerospace.

However, the highly porous nature of cellular solids induces experimental difficulties regarding 2D and 3D characterisation. Different morphological parameters, such as density distribution and cell and pore size, are difficult to measure because of sample preparation problems. To understand the application requirements, several design methods are adapted to generate the topology of highly porous composites, such as continuing improved material bounds approach for multiphase, multi-dimensional, isotropic/anisotropic and periodic/non-periodic composites with different physical properties and topology optimisation approach to material design. Frequently, this is performed within a finite element framework and typically involves large numbers of design variables, homogenisation or inverse homogenisation approaches in the design of microstructural materials, which has permitted an increased level of design capability and understanding of underlying material mechanisms.

Characterisation of cellular materials is an important process, allowing the examination of their physical and mechanical properties. While mechanical tests provide insight into material properties, they are not cost-effective and are time-consuming. Alternatively, mathematical and numerical models can assist the mechanical characterisation of such natural materials. This approach is more versatile, allowing refinement of the loading and environmental conditions to appreciate better both the ideal workings of the materials and to assess how the beneficial features of the material can be adapted to different engineering applications. Besides, the introduction of the material property measurements taking into account the material's density, such as specific modulus or specific strength, will help to understand and to assess the performance of the cellular structural composites. In this context, computational topology design and characterisation have become a prevalent tool in the fields of the structural and material composition.

2.1. CELLS STRUCTURE

The increasing interest in cellular materials is due to the possibility of combining the mechanical properties of the solid material with cellular microstructures. The result is a material with high specific strength with respect to the weight.

The main disadvantage of this type of material is the difficulty in obtaining models that reliably predict its properties, caused by the high complexity of foam geometry and its irregularity. Moreover, the foam presents a structure with a characteristic three-dimensional variability.

Macroscopic properties of a material such as elasticity, thermal conductivity or permeability are profoundly affected by its microstructure. Therefore, the design of modern high-performance materials requires insight into the microstructure of a given material as well as an understanding of its influence on physical properties. Geometric models are essential tools for studying these complex structure-property relations.

Using a model structure, the physical properties of the corresponding material are simulated. Repeated calculations with varying model parameters allow investigating how the material's properties change with altering microstructure. Thus, instead of producing many sample structures and choosing the best one for a given application, recommendations for good candidates can be obtained by simulation. The increasing capability of simulation algorithms, as well as computer power, allows for higher precision in the simulation results. In return, this requires more and more sophisticated model structures and model-fitting procedures.

The challenge then becomes one of introducing the porosity in such a manner that the mechanical behaviour is optimised for that level of density. The microstructure of the porosity becomes the most important feature controling the macroscale mechanical behaviour. Much of the current and future research intimately relates to understanding and managing the morphological microstructure of the low-density material to achieve specific levels of performance.

The most widely known and used reference is that of L. Gibson & Ashby (1997) and L.J. Gibson (1989). These authors, through their body of work on cellular solids, could be called the pioneers of the modern era in this field. Historically, the interest in ultra-porous materials arose through the fluid side in general and through liquid-induced foams in particular. Cellular forms dominated by surface tension effects have been of interest and even fascination for a very long time going back to the formulation of the basic rules for geometric stability given by Maxwell & Plateau (1874). The modern side has had developments progressing in unison in both the fluids and the solids sides. The fluidic aspects of the subject include the behaviours of liquid foams, types of emulsions, suspensions and a variety of related forms. The solid type applications have already been mentioned. A. M. Kraynik (1998) has given an exceptional review of both, the fluids and the solids forms entitled. The present references should be supplemented with those from that source. Also, M. Kraynik & Warren (1994) have given a review of mechanical behaviour for cellular solids.

One of the principal aspects that has to be mentioned is the concept of minimal surfaces. Cellular forms admit a geometric characterisation regarding the surface content or surface per unit volume. Opening the subject in this manner will give the first differentiation between cellular structures that, ultimately, will be very useful.

2.1.1. MANUFACTURING PROCESS

Foams or cellular structures can be manufactured from any material such as metal, polymeror ceramic. The properties of metal foams and other cellular metal structures depend on the properties of the metal, the relative density and cell topology (Section 2.1.2). This work efocuses on metallic cellular solids, so the manufacturing process is going to be centred on this type of material.

Frequently, the process of obtaining is divided into four categories, depending on how they are processed. The foam is formed:

- By vapour phase deposition.
- By electrodeposition.
- By processing during the liquid state.
- From the liquid state.

Nowadays, the most common processes are:

- Bubbling gas through the metallic union in the liquid state.
- Using an agent that releases gas while decomposing, promoting the formation of foam.
- Consolidating a metal powder with an agent that promotes foam formation, followed by heating to activate the agent.
- "Investment casting."
- Vapour phase deposition or electrodeposition of metal onto a polymer foam precursor, which is subsequently burned out, leaving cell edges with hollow cores.

Each one of these methods is applied to a specific group of materials, allowing for different relative densities and cells sizes.

Melt gas injection (air bubbling)

Pure liquid metals cannot easily be formed to foam by bubbling gas into them. This is because the resulting foam it is not stable long enough and collapses before the solidification of the metal. In order to solve this inconvenient, small, insoluble, or slowly dissolving particles, such as aluminium oxide or silicon carbide, are added. This increases the viscosity of the aluminium melt and prevents drainage in the bubble membrane, stabilising the foam. The following step is gas-injection through the metal. Several gases can be applied: air, carbon dioxide, oxygen and also water. Bubbles formed in this process tend to float to the melt surface, drain, and then begin to solidify rising to the metal foam, Figure 1.

The thermal gradient in the foam has the function to determine how long the foam remains liquid or semi-solid, and thus the extent of the drainage. Carefully controlling the gas injection process and the cooling rate of the foam allows the production of low relative density, closed-cell foams.

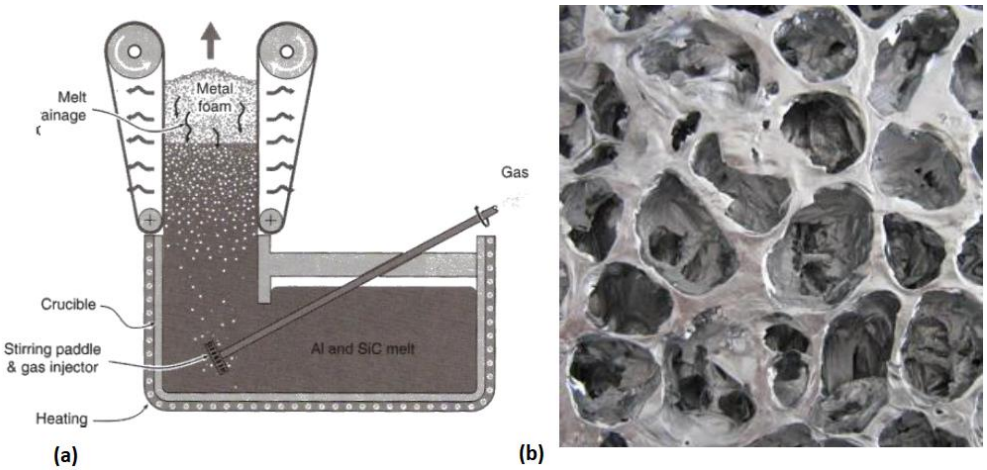

Figure 1(a) A schematic illustration of the manufacture of an aluminium foam by the melt gas injection method (CYMAT and HYDRO processes) (b) CYMAT foam microstructure. (M.F. Ashby, A.G. Evans, N.A. Fleck, L.J. Gibson, n.d.)

Gas-releasing particle decomposition in the melt

This process is the same in all the aspect to the one described above, with the exception that the gas is not injected in the melt. An agent of titanium hydride (TiH_2) is used.When the titanium hydride is heated, it begins to decompose into Ti and H_2, releasing the gas.

The process begins with the addition of calcium to raise the viscosity when the metal is in liquid state. After that, the titanium hydride particles are added and mixed with the metal. Because of the quick decomposition of the particles, the hydrogen gas is rapidly produced, created bubbles and giving origin to the foam, Figure 2.

The process is controlled by the volume fraction of calcium and titanium hydride, by the cooling conditions and the overpressure. Also, it is possible to obtain closed cell foams, since the viscosity is high enough to prevent the link between the bubbles.

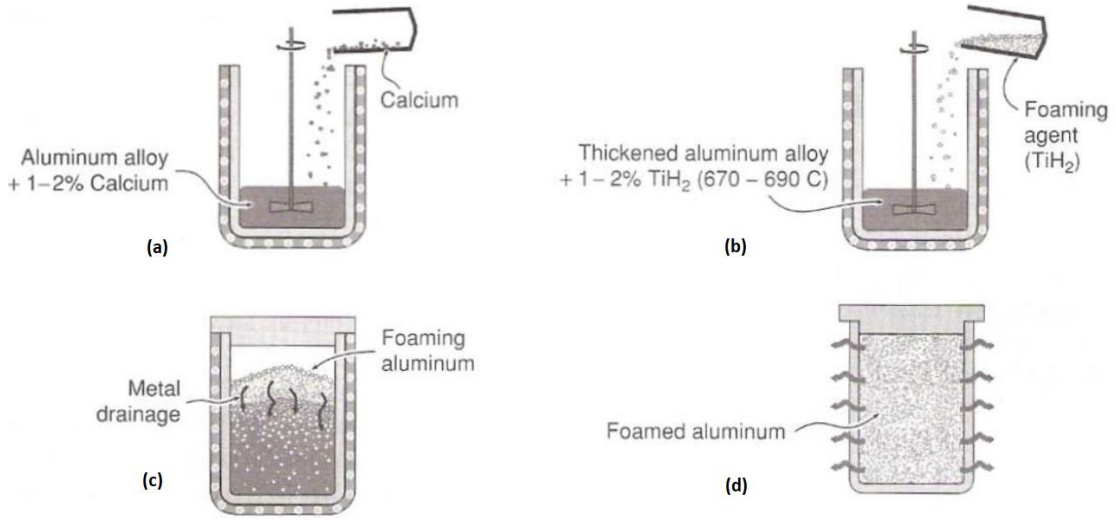

Figure 2 The process steps used in the manufacture of aluminium foams by gas-releasing particle decomposition in the melt (Alporas process) (a) Viscosity modification (b) foaming agent addition (c) isothermal foaming (d) cooling of foamed aluminium. (M.F. Ashby, A.G. Evans, N.A. Fleck, L.J. Gibson, n.d.)

Consolidation of a metal powder with an agent that promotes the formation of foam

This process employs a mixture of the metallic powder and the gas-releasing agent, TiH_2, as mentioned above. The mixture obtained is compacted and extruded, generating a solid that is made up of aluminium and TiH_2 particles. This solid is placed inside a shaped mold and heated. During the heating stage, the agent begins to decompose, releasing gas that expands the melt-solid and forms the foam, Figure 3.

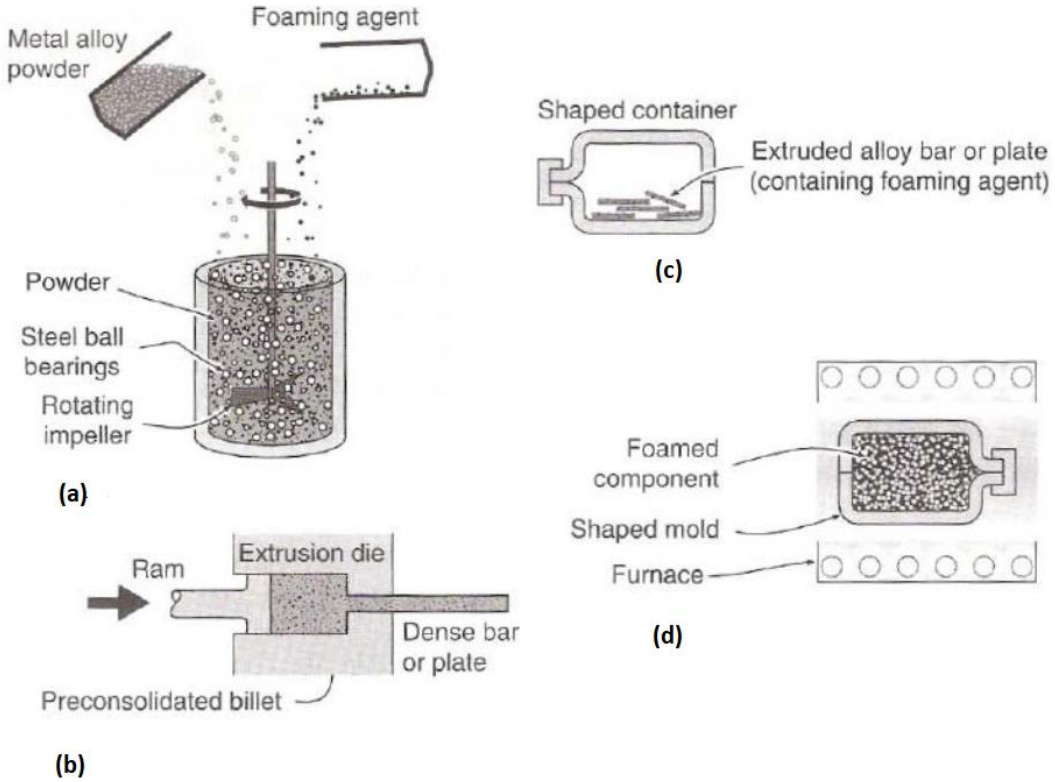

Figure 3 The sequence of powder metallurgy steps used to manufacture metal foams by gas-releasing particles in semi-solids (the Fraunhofer and the Alulight process) (a) Select ingredient and mix (b) Consolidation and extrusion (c) Shaped mold (d) Foaming. (M.F. Ashby, A.G. Evans, N.A. Fleck, L.J. Gibson, n.d.)

Casting using a polymer or wax precursor as a template. "Investment casting."

This process uses a polymeric foam, with open cells, as the mold for the metallic foam to be produced. The mold is coated with a ceramic slip and then sprayed with ceramic particles. This way, a ceramic shell is obtained. It acts as a negative of the foam that is intended to be made. The next step is to expose the ceramic shell to a thermal cooking cycle where the polymeric material decomposes, leaving the empty space for the introduction of the metal. After the solidification and cooling, the mold materials are removed leaving behind the metal equivalent of the original polymer foam, Figure 4.

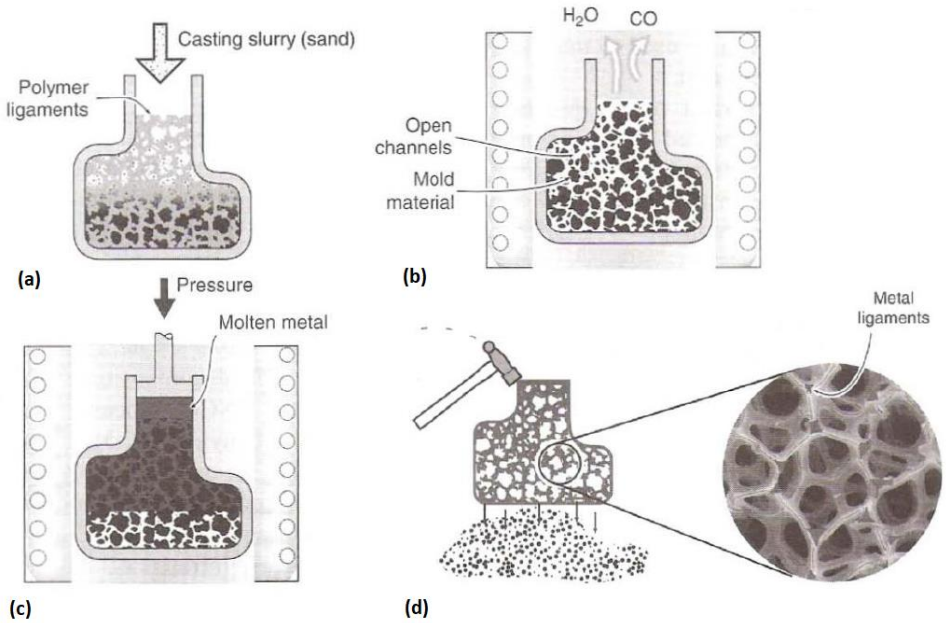

Figure 4 Investment casting method to manufacture open cell foams (DUOCEL process) (a) Preform (b)Burnout (c) Infiltrate (d) Remove mold material. (M.F. Ashby, A.G. Evans, N.A. Fleck, L.J. Gibson, n.d.)

Metal deposition on cellular preforms

This process entails the same steps to produce the negative for the metal foam described above, where a polymeric foam is employed as a mold for the metal foam. The difference is that, in this process, the metal foam is directly introduced into the polymeric matrix instead of in the investment casting that uses a ceramic negative. This deposition is done by chemical vapour decomposition (CVD), by evaporation or by electrodeposition. The polymeric matrix is burned very rapidly, leaving only the metallic foam.

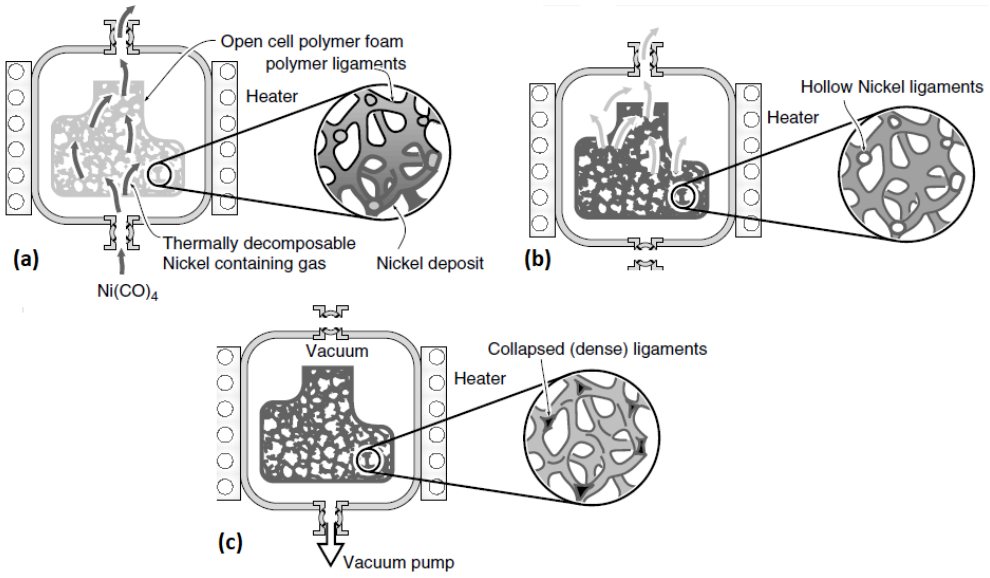

Figure 5 Schematic illustration of the CVD process used to create open-cell nickel foams (INCO process) (a) Vapor deposition of Nickel (b) Burnout polymer (c) Sinter (Ligament densification). (M.F. Ashby, A.G. Evans, N.A. Fleck, L.J. Gibson, n.d.)

2.1.2. MINIMAL SURFACES

The interest in minimal surfaces has existed for a very long time and has been deeply examined, mostly by mathematicians and physicists. The fundamental question is this: what is the repeating cellular form that subdivides space into cells, with the cells having a minimal surface area?. This traditional topic has been advanced into the modern developments and has become of high relevance in understanding the mechanical behaviour of cellular forms. Examining minimal surfaces begins the connection with the effect of microstructure variation, and this approach invests a high degree of order and logic into the proceedings.

Lord Kelvin (1887), (Thomson, 2008), proposed a minimal surface cellular form and it stood uncontested for over 100 years. The proposed Kelvin cell is that of a truncated octahedron, the tetrakaidekahedron, containing 14 faces, eight hexagons and six squares, as illustrated in Figure 6. The form periodically fills 3-space and repeats.

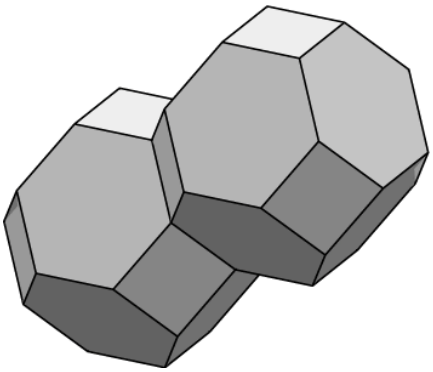

Figure 6 Kelvin cell (L. Gibson & Ashby, 1997)

In a recent and much-recognised development, (D. Weaire and R. Phelan, 1994) have identified a form with a lower surface content than that of the Kelvin cell. This form contains combinations of two cell types, a 14-sided structure with faces of pentagons and hexagons combined with the 12-sided regular dodecahedron. The average number of sides of the Weaire-Phelan form is 13-1/2.

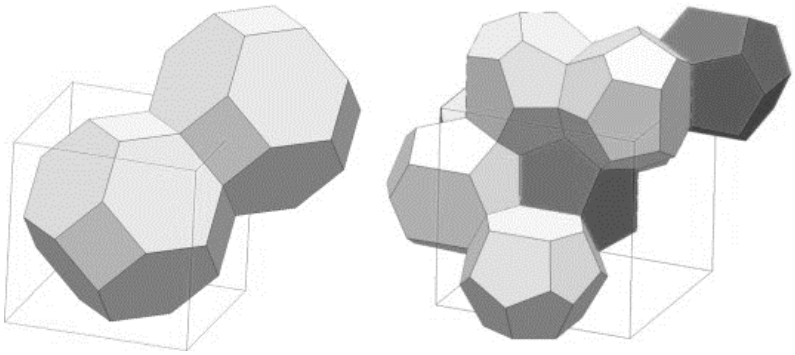

Figure 7 Weaire and Phelan cell (Buffel, Desplentere, Bracke, & Verpoest, 2014)

A nondimensional measure is needed to compare the surface content of different cell types. A convenient measure is given by

$$\zeta_{3D} = \frac{A}{V^{\frac{2}{3}}} \tag{2.1}$$

Where A is the cell area and V is the volume. When two or more cell types are involved, as with the Weaire-Phelan form, the values of ζ is found by averaging on $\zeta^{3/2}$ with volume weighting of the different cell types.

Table 1 3-D surface properties. Planar faces (warped faces) (Christensen, 2000)

Cell	Faces (Average)	$\frac{A}{V^{2/3}}$
Tetrahedra + Octahedra	5-1/3	6.234
Cube	6	6
Rhombic Dodecahedron	12	5.345
Weaire-Phelan	13-1/2	5.310 (5.290)
Kelvin	14	5.315 (5.306)

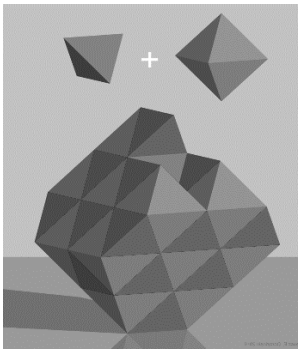

Figure 8 Tetrahedra + Octahedra cell

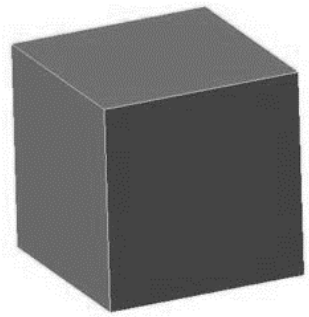

Figure 9 Cube cell

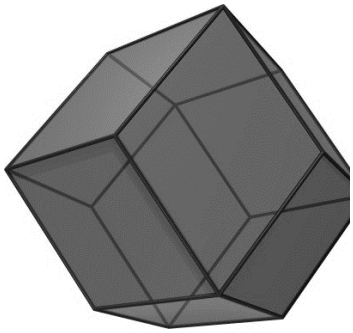

Figure 10 Rhombic Dodecahedron

Table 1 presents the surface measure for different cellular forms that fill space. All cases have cubic symmetry, and this is the highest order symmetry that can be obtained by a space-filling periodic repeating cell pattern. The proximity of the Kelvin cell and the Weaire-Phelan cell make them ideal candidates for the study of mechanical properties. Also note that the values of ζ in Table 1 are for planar faces. Allowing the faces to warp can reduce the surface area even a little further as shown by the values for the Kelvin cell and the Weaire-Phelan cell, taken from (D. Weaire and R. Phelan, 1994).

Table 2 2-D surface properties (Christensen, 2000).

Cell	Sides (Average)	$\frac{L}{A^{2/3}}$
Triangular	3	4.56
Square	4	4
Hex-Triang	4	3.95
Hexagonal	6	3.72
Star (Star + Hex)	8	4.56

The quest for minimal surface forms can go further. Polydisperse cell forms can be constructed and evaluated. The standard approach begins with either regular or random point placements, and this involves the construction of Voronoi cells,(A. M. Kraynik, 1998). The resulting forms can be taken in one step further by relaxing the geometry to obtain minimal

surfaces using the surface evolver program of Brakke (1992). It has been found that some polydisperse cell forms can have even slightly lower surface content than the forms in Table 1.

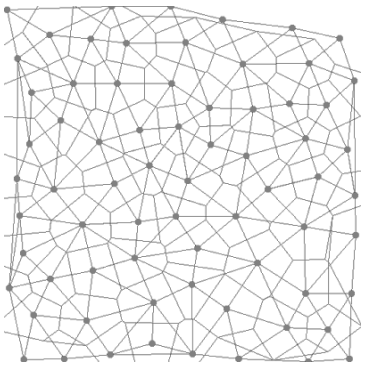

Figure 11 Voronoi cell 2-D

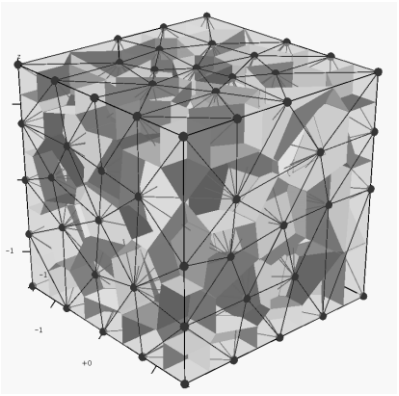

Figure 12 Voronoi cell 3-D

Thus far, the three-dimensional case has been discussed. The corresponding two-dimensional case is equally well posed, although, historically, the significant interest in the three-dimensional case came first. Table 2 shows the two-dimensional cellular forms with the surface measure (surface per unit thickness) given by

$$\zeta_{2D} = \frac{L}{A^{\frac{1}{2}}} \tag{2.2}$$

Where L is the cell perimeter and A is the cell area. The cell types are shown in Figure 6. In the cases where two cell forms are combined, the average ζ is found by averaging ζ^2 with area weighting. The hexagonal cell has minimal surface content, as is well understood and propagated as the ubiquitous 'honeycomb'. Many other two-dimensional cellular forms could be considered even non-periodic but repeating forms such as the Penrose pattern (Penrose, 1979).

The term relative density is often used being:

$$\frac{\rho^*}{\rho_s} = \frac{\rho}{\rho_m} = (1 - c) \tag{2.3}$$

With ρ being the density of the low material form and ρ_m being the density of the composing material. Polymeric foams used for cushioning, packaging and insulation have relative densities that are usually between 0.05 and 0.2; cork is about 0.14, and most softwoods are between 0.15 and 0.40. As the relative density increases, the cell walls thicken and the pore space shrinks; above about 0.3 there is a transition from a cellular structure to one which is better considered as a solid containing isolated pores.

The required local minimal characteristics in two and three-dimensions are well understood. In 2-D, three cell sides must meet at 120° angles. In 3-D, four cell edges meet at tetrahedral angles, and three surfaces intersect at 120° angles to form the edges. A mathematically-related minimum length (not surface) problem has been formulated by Christensen (1996).

Table 3 2-D Mechanical properties (Christensen, 2000)

Microstructure	$\frac{\mu}{E_m}$	$\frac{K}{E_m}$	$\frac{E}{E_m}$	v
Triangular	$\frac{1}{8}(1-c)$	$\frac{1}{4}(1-c)$	$\frac{1}{3}(1-c)$	1/3
Hexagonal	$\frac{3}{8}(1-c)^3$	$\frac{1}{4}(1-c)$	$\frac{3}{2}(1-c)^3$	1
Star Shaped	$\frac{3}{16}(1-c)^3$	$\frac{9}{16}(1-c)^3$	$\frac{9}{16}(1-c)^3$	½
GSCM	$\frac{1}{16}(1-c)^3$	$\frac{1}{4}(1-c)$	$\frac{1}{4}(1-c)^3$	1
Holes, Triangle Pattern $C_M = \frac{\pi}{3\sqrt{3}}$	$\frac{1}{12_{C_M}}(1-\frac{c}{C_M})^{1/2}$	$\frac{1}{6_{C_M}}(1-\frac{c}{C_M})^{1/2}$	$\frac{2}{9_{C_M}}(1-\frac{c}{C_M})^{1/2}$	1/3
Holes, Hex Pattern $C_M = \frac{\pi}{2\sqrt{3}}$	$\frac{1}{9_{C_M}}(1-\frac{c}{C_M})^{3/2}$	$\frac{1}{12_{C_M}}(1-\frac{c}{C_M})^{1/2}$	$\frac{4}{9_{C_M}}(1-\frac{c}{C_M})^{3/2}$	1

These minimal surface forms are of high relevance to the mechanical performance problem because, in many cases, the methods of synthesis and manufacture are controlled by phase separation processes with surface tension being the controlling physical effect. Blown foams are the perfect example of this effect. The fundamental question to be answered is this: how do mechanical properties relate to these minimal surfaces, and how would the mechanical properties be affected by cellular forms that are far removed from the minimal surface forms?

It is advantageous to begin the examination of mechanical behaviour with the two-dimensional case because the path to understanding is less complicated than for 3-D. Nevertheless, the 2-D case is of great interest and importance.

2.1.3. 2-D Mechanical Behaviour

It is appropriate to begin with the 2-D microstructure that is shown in Figure 6 and Table 2. Two-dimensional properties refer to states of plane stress or plane strain. Much of the concern here will be with the case of 2-D isotropy since the state of isotropy is the backbone for understanding all types of behaviour. Hexagonal symmetry assures isotropy of the mechanical properties. Much of the work in this area was initiated by L. J. Gibson & Ashby (1982b). The subject is broadly covered in the book by L. Gibson & Ashby (1997).

Table 3 shows the model for the elastic modulus for different microstructures in the range where the volume fraction of the voids is almost at the limit beyond which material collapse occurs. Properties μ, K, E and v, are the effective 2-D plane stress shear modulus, bulk modulus, Young's modulus, and Poisson's ratio, respectively. The quantity $(1-c)$ is the volume fraction of material, which is taken to be very small compared with one, for $c \to 1$.

Gibson and Ashby first outlined the hexagonal case in Table 3. The triangular and star microstructure properties were given by Christensen (1995), (M.Naghdi, 2013). A great variety of behaviours are evidence in Table 3. Properties proportional to $(1-c)$ are recognised to be due to the direct extension or contraction of the material members, while properties proportional to $(1-c)^3$, at orders of magnitude of lower levels, are due to bending of the material members. The triangular, hexagonal and star microstructure forms are probably the three classical forms delineating a variety of properties. Certainly, the first two are so standard as to be conventional, and the third may complete the different picture of different types of behaviour. Probably the properties form in Table 3 for the triangular case have been known for a very long time, but the original credit for these explicit formulas is unknown at this time. The GSCM case is that of the Generalized Self Consistent Method, (Richard M. Christensen, 1993), involving the packing of circular forms of a distribution of sizes. A few of these same cases, as well as others, are analysed and discussed by Torquato, Gibiansky, Silva, & Gibson (1998).

There is an unlimited number of physical arrangements that give isotropic behaviour. The consideration of anisotropic forms is now beginning to be considered in a manner that leads to applications. This is well illustrated by the work of Overaker, Cuitino & Langrana (1998). These authors have examined highly anisotropic 6-sided cellular forms involving re-entrant angles. They show that the negative Poisson's ratio effect itself is highly anisotropic, with negative values only occurring concerning specific directions of loading relative to the microstructure. They discuss applications of such forms using the 'anchoring' effect related to negative Poisson's ratios.

Consideration of strength is equally important as that of the stiffness and compliance properties. In the very low-density region, the buckling of the micro-material members is the dominant mechanism. This occurs not only in a state of compression but can occur in tension also. With regards to the periodic microstructure, the strength properties can be highly anisotropic, even when the symmetry is not available. This remains to be developed. Specific discussions of failure mechanisms and behaviour are given by L. Gibson & Ashby (1997).

The physical reality of most cellular forms is that they seldom conform to the idealised microstructure, due to manufacturing methods and tolerances and due to general aspects of usage. The corrupting influences include imperfect connectedness and non-aligned micro-member geometry. Grenestedt (1998), has performed a study on the effect of the 'waviness'. It was shown that such imperfections, within the realistic range, have a sharply degrading impact upon properties. The implications of this are equally crucial to the three-dimensional case.

The most significant example of this class of materials is that of the honeycomb core for sandwich materials. As shown by Allen (1969), Noor (1996) and Vinson (1999), the core in sandwich construction can be a limiting factor for this type of design.

The in-plane strength and failure mechanisms of honeycomb materials have been extensively studied by Papka & Kyriakides (1998). In general, instabilities develop locally and spread with increased loading. The stress-strain curve typically exhibits a plateau region. These same authors also have studied cellular forms involving single size circular rings or cylinders packed in a hexagonal manner. The same general features of behaviour evolve in this case. The out of plane compression of these types of materials involves a kind of buckling followed by plastic deformation. Large amounts of energy can be absorbed during crushing, making such

forms ideal for crash protection. This important topic is accosted by Santosa & Wierzbicki (1998).

Returning to sandwich forms, there is an opportunity to develop different core material forms for various types of applications. For example, honeycomb does not easily conform to curved shapes, other types of cores are more suitable for this application.

2.1.4. 3-D Mechanical Behaviour

The full-blown case of low-density materials in 3-D forms and applications is a vibrant, active and diverse field. In contrast to the 2-D case, a significant new distinction arises in the 3-D case. This is the circumstance of the open cell form versus the closed cell form. Both cases are of great importance and must be treated separately. At first consideration, it can be said that the open cell form favours strength, and the closed cell form favours stiffness, as idealisations. However, the problem is much subtler than that. Much depends on the technique and quality of manufacture, and often other design requirements take precedence, such as using closed cell forms to prevent moisture penetration.

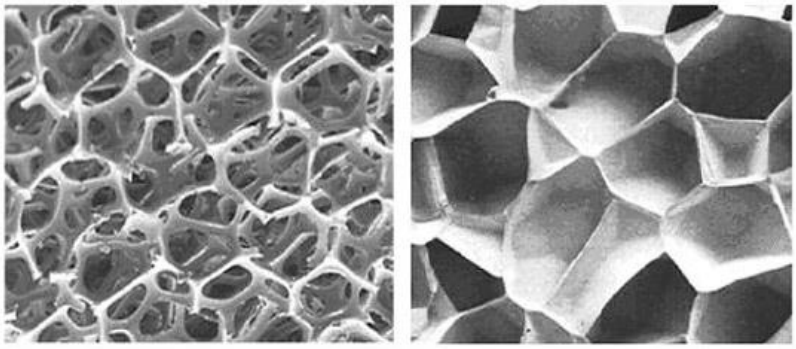

Figure 13 Open-cell (left), Closed-cell (right) (L. Gibson & Ashby, 1997)

First, consider the open cell case. The relevant cell type to consider would be the Kelvin cell, a truncated octahedron. This has been done by Warren and Kraynik (1997). Several new ingredients arise in the 3-D case that do not exist in the 2-D case. First, for those materials that are synthesised by a phase separation process, there is a process sequence of forming minimal surface cell followed by evacuation of the material from the faces into an aggregation along the cell edges, leaving the open cell form. The consequence of this process is that the intersection of three Plateau borders forms the cross-section of the material members, (A. M. Kraynik, 1998), involving convex circular arcs or some approximation thereof. Another complication is that the micro-material members can not only undergo bending as in the 2-D case but can undergo torsion as well. It can be shown that the torsion effects are of the same order as the bending effects and cannot be neglected.

The Kelvin cell aggregation has cubic symmetry, with three independent elastic properties. Warren and Kraynik (Warren & Kraynik, 1997), show that the properties are almost isotropic, to within a few percents. In one of the most important results, they reveal the particular case in which the cubic properties form reduces precisely and identically to the case of isotropy. This case is that which occurs when the material members have a circular cross-section and when the material Poisson's ratio is $v_m = 0$. In this case, their results give the isotropic bulk modulus and shear modulus as

$$\frac{k}{E_m} = \frac{1}{9}(1-c) \tag{2.4}$$

and

$$\frac{\mu}{E_m} = \frac{4\sqrt{2}}{9\pi}(1-c)^2 \cong \frac{1}{5}(1-c)^2 \tag{2.5}$$

The fact that this case involves cross-section members, rather than those with Plateau borders does not detract from its significance. The circular case can be taken as the base-line behaviour. The shear properties of the Plateau border case are considerably larger than the above value due to the increased bending and torsional rigidity. A. M. Kraynik (1998) discusses results for the cell types, such as the Weaire-Phelan cell and poly-disperse forms.

It is seen that the properties just stated involve the bulk modulus dominated by the direct mechanism of deformation, while the shear modulus is given by the bending (and torsion) mechanism. The situation is akin to that which occurred in the 2-D case, both cases with cell forms simulating the minimal surface cell.

As with the 2-D case, there is a behaviour that involves only the direct mechanism. This isotropic result was first given by Gent & Thomas (1959), as deduced, not from any particular cell type. The bulk modulus is the same as provided above, but the shear modulus and Young's are given by

$$\frac{\mu}{E_m} = \frac{1}{15}(1-c) \tag{2.6}$$

and

$$\frac{E}{E_m} = \frac{1}{6}(1-c) \tag{2.7}$$

It should also be noted that Ko (1965) was one of the very early contributors to the field with studies of several cell types. L. J. Gibson & Ashby (1982a) analyse and discuss 3-D material behaviour regarding all properties involving the bending mechanism. Table 4 provides a summary of the different bending mechanics study by L.J. Gibson and Ashby.

Table 4 Elastic moduli and strength of foams (L.J. Gizbson, 1989)

Deformed cell	*Analysis*	*Foam property*
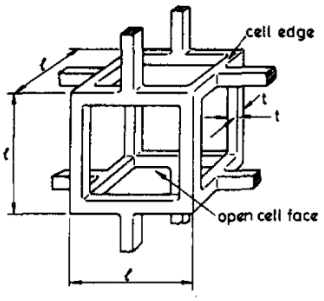	Solid cell Wall properties: Density ρ_s Young's modulus E_s Yield strength σ_{ys} Modulus of rupture σ_{fs}	$\frac{\rho^*}{\rho_s} \propto \left(\frac{t}{l}\right)^2$ (2.8) $l \propto t^4$

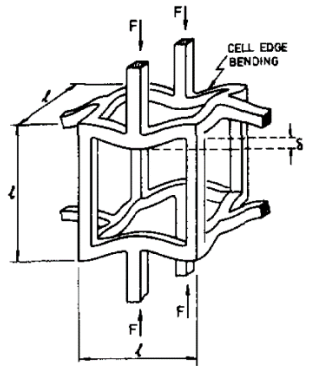

$$\sigma \propto \frac{P}{l^2}$$

$$\varepsilon \propto \frac{\delta}{l}$$

$$\delta \propto \frac{Pl^3}{E_s I}$$

$$\frac{E^*}{E_s} = C_1\left(\frac{\rho^*}{\rho_s}\right)^2 \approx \left(\frac{\rho^*}{\rho_s}\right)^2 \qquad (2.9)$$

$$\frac{G^*}{E_s} = C_2\left(\frac{\rho^*}{\rho_s}\right)^2 \approx \frac{3}{8}\left(\frac{\rho^*}{\rho_s}\right)^2 \qquad (2.10)$$

$$v^* = C_3 \approx \frac{1}{3}$$

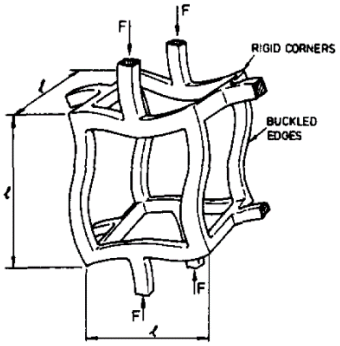

$$\sigma^*_{el} \propto \frac{P_{cr}}{l^2}$$

$$P_{cr} \propto \frac{E_s I}{l^2}$$

$$\frac{\sigma^*_{el}}{E_s} = C_4\left(\frac{\rho^*}{\rho_s}\right)^2 = 0.05\left(\frac{\rho^*}{\rho_s}\right)^2 \qquad (2.11)$$

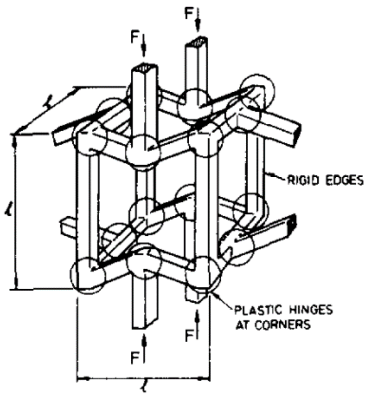

$$\sigma^*_{pl} \propto \frac{P^*}{l^2}$$

$$P^* \propto \frac{M_p}{l}$$

$$M_p \propto \sigma_{ys} t^3$$

$$\frac{\sigma^*_{pl}}{\sigma_{ys}} = C_5\left(\frac{\rho^*}{\rho_s}\right)^{\frac{3}{2}} = 0.3\left(\frac{\rho^*}{\rho_s}\right)^{\frac{3}{2}} \qquad (2.12)$$

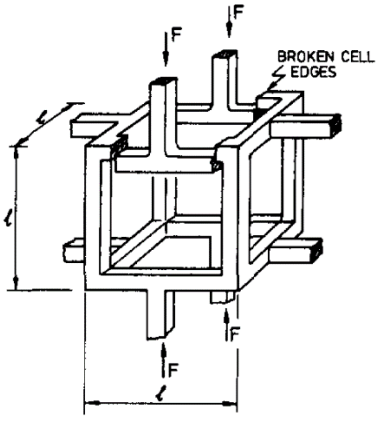

$$\sigma^*_{cr} \propto \frac{P^*}{l^2}$$

$$P^* \propto \frac{M_f}{l}$$

$$M_f \propto \sigma_{fs} t^3$$

$$\frac{\sigma^*_{cr}}{\sigma_{fs}} = C_6\left(\frac{\rho^*}{\rho_s}\right)^{\frac{3}{2}} = 0.65\left(\frac{\rho^*}{\rho_s}\right)^{\frac{3}{2}} \qquad (2.13)$$

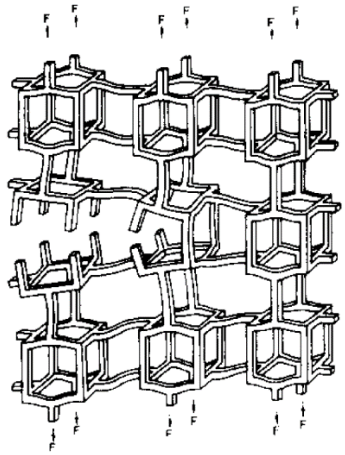

$$\sigma_{loe} \propto \frac{\sigma_1(\pi a)^{1/2}}{(\pi l)^{1/2}} \propto \frac{M_f}{l^3}$$

$$M_f \propto \sigma_{fs} t^3$$

$$K_{le}^* \propto \sigma_l(\pi a)^{1/2}$$

$$\frac{K_{le}^*}{\sigma_{fs}} C_7(\pi l)^{\frac{1}{2}} \left(\frac{\rho^*}{\rho_s}\right)^{\frac{3}{2}} = 0.65(\pi l)^{\frac{1}{2}} \left(\frac{\rho^*}{\rho_s}\right)^{\frac{3}{2}} \quad (2.14)$$

Now consider closed cell forms. The work of Christensen (1998) has used the Generalized Self Consistent Method to obtain the following predictions for the isotropic bulk and shear moduli.

$$\frac{k}{E_m} = \frac{2}{9(1-v_m)}(1-c) \quad (2.15)$$

and

$$\frac{\mu}{\mu_m} = \frac{1}{3}(1-c) \quad (2.16)$$

A. M. Kraynik (1998) has used and discussed finite element models to obtain results for the case of $v_m = 0.49$. These results for the Kelvin cell and the Weaire-Phelan cell are nearly isotropic and in quite close agreement with the above analytical solution results. The shear moduli involve a direct resistance mechanism as shown by the $(1-c)$ dependence in contrast to the open cell case. It is quite interesting to note that the above analytical solution predicts the value for μ/μ_m to be independent of Poisson's ratio v_m. This unexpected result could be checked against numerical solutions. It is seen that the closed cell form, from the point of view of effective moduli, provides a much more efficient material utilisation than does the open cell form.

The large deformation properties of low-density material present a challenge. Budiansky & Kimmel (1987) considered forms appropriate for the behaviour of lung tissue. Zhu, Mills & Knott (1997) have studied open cell forms using the Kelvin cell and performing elastic type analyses with local material buckling at large compressive strains. They found a strong dependence of the nonlinear stress-strain curve upon the direction of deformation. Even though the form is nearly isotropic in the small strain range, there is no reason to expect any form of isotropy in the vast deformation range. Although typical stress-strain curves often show a plateau type behaviour at sufficiently large strains, A. M. Kraynik (1998) and Zhu et al. (1997) found a few cases in which no plateau region exists. Strength considerations are not extensively treated for these materials, and this represents a significant opportunity area. Compressive strength is the limiting condition due to bucking of the micro-material thickness will be much less in the closed cell form than in the open cell form, favouring the open cell form for strength. General considerations on the effect of imperfections as seen in Grenestedt (1998), are probably even more critical in the three-dimensional case than in 2-D.

Low-density material forms, both closed and open cell, are made with the full spectrum of material types, metals, polymers and ceramics. Polymers have been the traditional materials for these forms, but other materials are also rapidly progressing. A survey of opportunities with cellular metallic forms is given by Evans, (Anthony G. Evans, Hutchinson, & Ashby, 1998). Related studies by Evans, (A. G. Evans, Hutchinson, & Ashby, 1998), and Sugimura, Rabiei, Evans, Harte, & Fleck, (1999) have given detailed morphology characterisation using synchrotron X-ray tomography for aluminium open cell forms and shown the mechanical behaviour to be as predicted by the theoretical forms in the literature. It is likely that an extensive variety of forms and applications will emerge using all material types in cellular forms.

As mentioned in connection with two-dimensional behaviour, negative Poisson's ratio effects can be induced by controlling the material microstructure. Choi & Lakes (1992) and Choi & Lakes (1995) have shown how the re-entrant angle form can produce these effects and how the effect can be employed. This is, in fact, an excellent example of how cellular materials can be designed to produce specific desired effects.

Up until this point, all low-density material types have been based upon specific cellular forms. This characteristic is not required; low-density forms can exist with no discernible cellular morphology. Aerogel materials are the perfect example of such forms. These materials exist in the ultra-low-density range, and the morphological characteristic is best described on a scale not too much larger than that of angstroms, with forms sometimes called a 'string of pearls'. Mechanical characterisation of these materials has been given by Scherer, Smith, & Stein (1995).

Cellular forms would not be complete without mentioning the mechanics of bio-materials in general. However, this topic is too extensive, and it is not the central aspect of this work. More information on this topic is presented in Kinney & Ladd (1998) and Yang et al. (1998).

2.1.5. SIZE EFFECTS

One important characteristic that is essential to take into account is the mechanical properties upon which size depends. The stiffness of the sample depends significantly on relation between cell size and the size of the sample. The state of the surface as either homogenous or heterogeneous and the way how the surfaces are interconnected or loaded in the tests also have an influence..

In the case of the traction, compression and bending test, it has been verified that the measured modulus decreases when the size of the sample decreases. In the shear test, the opposite occurs, with decreasing sample sizes leading to increasing shear moduli.

2.1.6. UNIAXIAL COMPRESSION AND TRACTION TEST

The tension curve deformation of an uniaxial compression test L. J. Gibson & Ashby (1989) is illustrated in Figure 14.

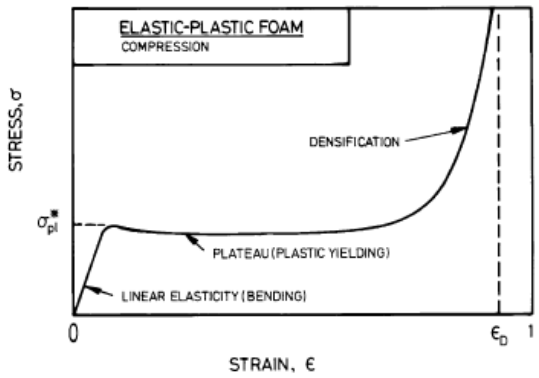

Figure 14 Stress-strain graphic representation of a compression test (L. Gibson & Ashby, 1997)

It is possible to differentiate three characteristic zones. In the first zone, the material presents an elastic deformation, thereby exhibiting a linear evolution of stresses and strains. The internal distribution of the cells represents an essential influence in the deformations mechanisms. For foams with low density and open-cells, the elastic deformation occurs because of the bending of the cells unions. With respect to the increase in density, the contributions of the cells unions are more significant. In the case of closed-cells, the stiffness increases because of the contribution of the wall. The air compression inside the cells also plays a significant part in the stiffness increase in closed-cells.

The second zone corresponds to deformation with almost constant stress. This is because of the collapse of the cells. This type of collapse depends on the material being either fragile or plastic. The collapsing occurs when the stress exceeds acertain value, and it spreads in a plane perpendicular to the stress direction. The collapsed zone increases as far the strain increases. The plastic collapse in elastic-plastic foams results in a horizontal development in the stress-strain graphic. This is one of the principal characteristics of cellular materials, as it concerns energy absorption.

The third zone is related to the densification of the material. As the strain increases, the cell walls come in contact generating a rapid increase of the stress to the strain.

Figure 15 shows the values of the strain stress in a traction test L. J. Gibson & Ashby (1989).

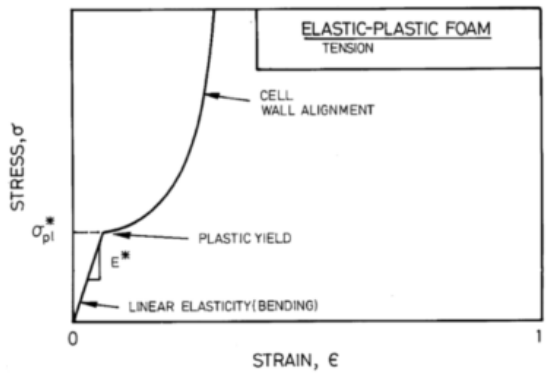

Figure 15 Stress-strain graphic representation of a traction test (L. Gibson & Ashby, 1997)

The initial response in the traction test is linearly elastic; this is because of bending of the cell walls. In ductile materials and as the strain increases, the cells walls suffer rotations, trying to align with the direction of the stress. These rotations generate an increment in the foam stiffness until fracturing occurs.

2.1.7. MATERIAL PROPERTIES

As mentioned above, the properties of cellular solids have two significant reliable parameters. There are those that describe the geometric structure of the foam- the size and shape of the cells. And there are parameters that define the intrinsic properties of the material of which the cells are made.

Regarding the composition of cellular solids, there are three large groups of materials: polymers, ceramics and metal.

Polymeric foams were the first developed into cellular solids. Their large energy absorption capacity enables them to be to used for packaging or for protection against shock (such as helmets). This explains a large number of recent studies on the compressive behaviour of this type of foams: PVC, polyurethane and polypropylene (for the 3D rendering of these materials). Polymer foams are also widely used as templates to process ceramic metal foams.

Ceramic foams are used in a wide range of applications: filters, solid oxide fuel cells, construction materials (cellular concrete plasterboards) and biomaterials. Many publications describe work with bone substitutes and attempt to compare their mechanical properties or focus on the interaction between bone substitutes and natural bones.

Metal foams constitute the relatively recent class of cellular solids. As polymeric foams, their lightness and energy absorption capacity is absorbing, but they can be used at higher temperatures. Moreover, cellular metals are stronger than cellular polymers and tougher than cellular ceramics. This combination of properties is very interesting in load-bearing applications (sandwich cores) or in applications that require shock absorption (automobile, helmet, packaging and cushions). Several authors have thus investigated the mechanical behaviour of aluminium alloy foams because of their set of interesting properties: low weight, high strength, ductility, corrosion, resistance, and recyclability. More recently, metallic materials based on other metals (copper alloy, nickel, steel and titanium) have also been investigated.

2.2. HONEYCOMB (2-D CELLULAR SOLID)

The honeycomb of the bee, since it is a regular array of prismatic hexagonal cells, epitomises the two dimensional cellular solid. The term honeycomb is a way to describe any array with identical prismatic cells that nest together to fill a plane. The cells are usually hexagonal in section, just like they are in the bee's honeycomb, but they can also be triangular, or square, or rhombic.

One of the reasons for studying honeycombs is that the results shed light on the mechanics of the much more complicated three-dimensional foams. Analysing foams is a challenging topic: the cell walls form an intricate three-dimensional network that distorts during deformation in ways that are hard to identify. In this aspect, honeycombs are much easier. Large-scale models can be made of rubber, metal or ceramic; and their deformations modes observed and classified. Because the honeycomb has a regular geometry, its deformations can be analysed more or less precisely with five equations that describe their properties. Finally, the results can be checked by experimental models.

2.2.1. DEFORMATION MECHANISMS IN HONEYCOMB

If a honeycomb is compressed in-plane, the cell walls bend at first, giving linear elastic deformations. Beyond a point of critical strain, the cells collapse by elastic buckling, plastic yielding, creep or brittle fracture, depending on the nature of the cell wall material. Cell collapse ends once the opposing cell walls begin to touch each other; as the cells close up, the structure densifies, and its stiffness increases rapidly. In tension, the cell walls bend at first (as in compression) but elastic buckling is not possible. If the cell wall material yields plastically,the honeycomb itself shows excellent plasticity; if the cells are brittle it fractures. On loading out-of-plane (such that a component of stress acts parallel to the axis of the prismatic cells) the cell walls suffer extension or compression, and the module and collapse stresses are much more significant.

2.2.2. IN-PLANE DEFORMATION

In Figure 16,(L.J. Gibson & Ashby, 1989), shows the compressive and tensile stress-strain curves for an elastomeric honeycomb (a rubber), and elastic-plastic honeycomb (a metal) and one that is elastic-brittle (a ceramic). It is possible to observe that they have similar shapes, but for different reasons.

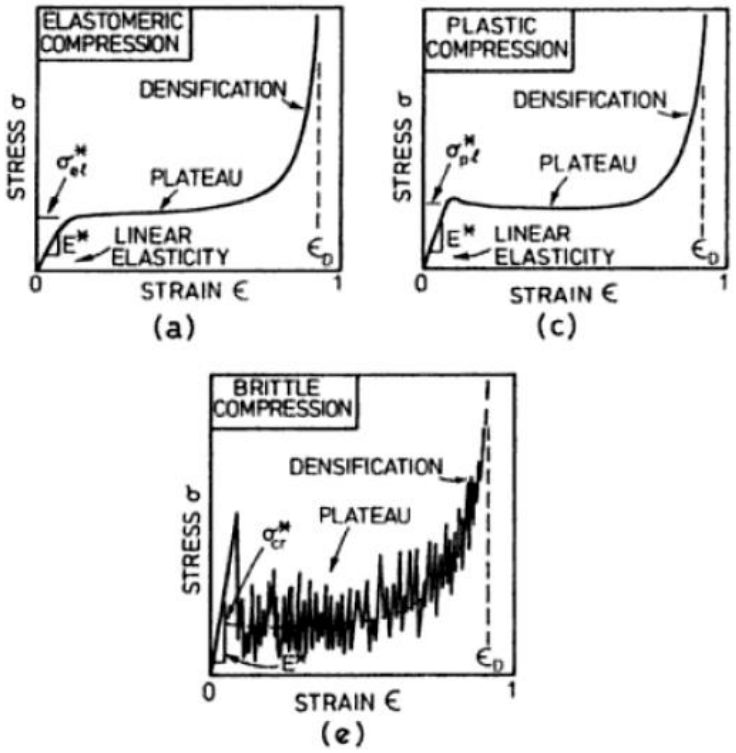

Figure 16 Compressive curve for honeycombs (a) elastomeric, (c) elastic-plastic and (e) elastic-brittle, (L.J. Gibson & Ashby, 1989).

In compression, all show a linear-elastic regime followed by a plateau of roughly constant stress. Each regime is associated with a mechanism of deformation. On the first loading, the cell walls bend, giving linear elasticity, because the cell wall material is linear-elastic. However, when critical stress is reached, the cells begin to collapse: in elastomeric materials, the collapse is due to elastic buckling of the cell walls and so is recoverable. In materials with

a plastic yield point, the collapse occurs by the formation of plastic hinges at the section of the maximum moment in the bent member, while in brittle materials, the collapse is casued by brittle fracture of the cell walls. These last two are not recoverable. Eventually, at high strains, the cells collapse sufficiently for opposing cell walls to touch (or broken pieces pack together) and further deformation compresses the cell wall material itself. This gives the final stage, a steeply rising portion of the stress-strain curve labelled densification.

An increase in the relative density of a honeycomb increases the relative thickness of the cell walls.

Tensile deformation can be different,as shown in Figure 17.

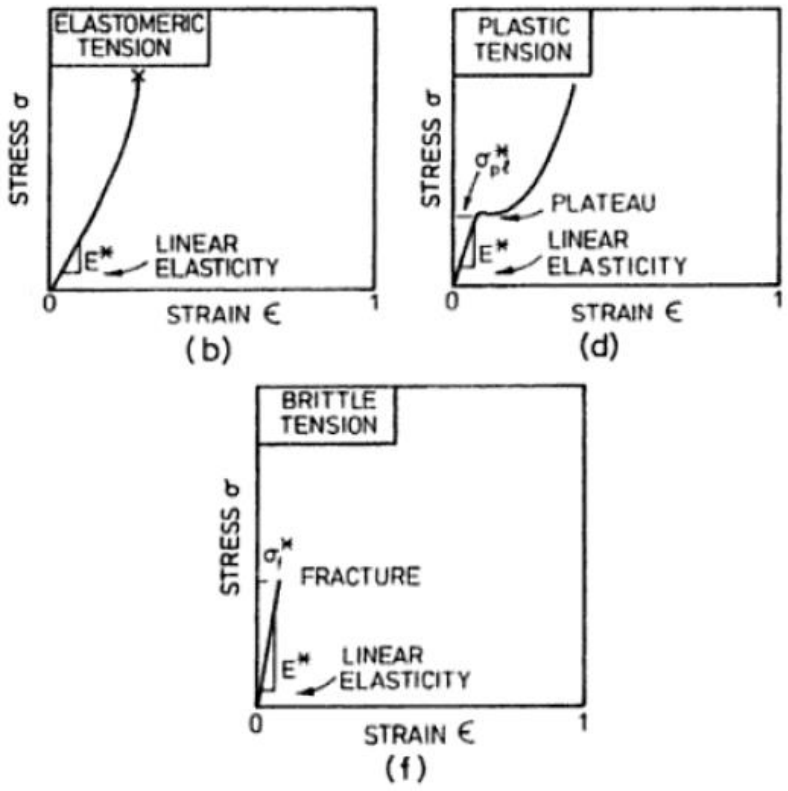

Figure 17 Tension curve for honeycombs (b) elastomeric, (d) elastic-plastic and (f) elastic-brittle,(L.J. Gibson & Ashby, 1989).

Initially, the cell walls bend producing a linear-elastic deformation with the same slope (and so the same modulus) as in compression. In tension, however, an elastomeric honeycomb does not buckle; instead, the cell walls rotate towards the tensile axis, and the stiffness rises. Plastic honeycombs behave in almost the same way as they do in compression: plastic hinges form, allowing large deformations at a nearly constant 'plateau' stress; only the geometry change introduces a difference usually pushing the tensile curve above the compressive one. Brittle honeycombs fail abruptly in tension, at a stress that is usually lower than the real crushing strength. Increasing the relative density has a similar effect to that observed for compression: the elastic moduli, plastic yield stress and brittle fracture stress all increase.

2.2.3. OUT-PLANE DEFORMATION

Honeycombs are much stiffer and stronger when loaded along the cell axis- the X3 direction. The same is true for honeycombs loaded in out-of-plane shear (as they are in sandwich panels loaded in bending). In these cases, the initial linear-elastic deformation involves significant axial or shear deformations of the cell walls. In compression, the linear-elastic regime is truncated by buckling (elastic for an elastomer, plastic for metal or rigid for polymer) and final failure is caused by tearing or crushing, giving a stress-strain curve like that shown in Figure 18, (L.J. Gibson & Ashby, 1989). In tension, the honeycomb is elastic until is broken, yields plastically or fractures.

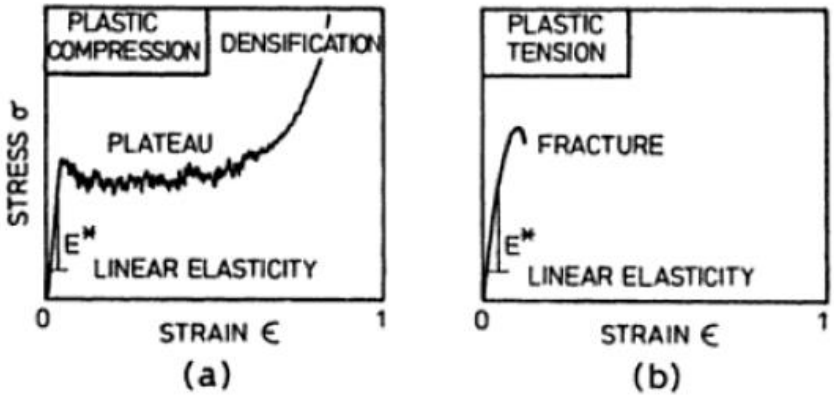

Figure 18 Stress-strain curves for the axial (X3) loading of a honeycomb, (a) compression, (b) tension, (L.J. Gibson & Ashby, 1989).

2.2.4. THE IN-PLANE AND OUT-OF-PLANE PROPERTIES OF HONEYCOMBS: UNIXIAL LOADING

In the case of in-plane, the load is applied in the $X_1 - X_2$ plane. If the hexagon is regular (that is, the sides are equal, and the angles are all 120º) and the cell walls are all the same thickness, then the in-plane properties are isotropic: they do not depend on direction. In the case where the hexagon presents irregularities in the angles and in the thickness of the walls, the properties are anisotropic.

Table 5 In-plane elastic moduli of honeycombs (L.J. Gibson, 1989)

Deformed cell	***Analysis***	***Honeycomb property***	***Value of property for h/l and $\theta = 30^o$***
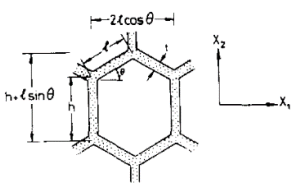	Solid cell Wall properties: Density ρ_s Young's modulus E_s Yield strength σ_{ys} Modulus of rupture σ_{fs}	$\frac{\rho^*}{\rho_s} = \frac{t}{l}\frac{\frac{h}{l}+2}{2cos\theta(h/l+sin\theta)}$ (2.17) $I = \frac{bt^3}{12}$ (2.18)	$\frac{2}{3^{\frac{1}{2}}}\frac{t}{l}$

$$\sigma_1 = \frac{P}{b(h + lsin\theta)} \quad (2.19)$$

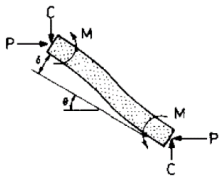

$$\varepsilon_1 = \frac{\delta sin\theta}{lcos\theta} \quad (2.20)$$

$$\varepsilon_2 = \frac{\delta cos\theta}{h + lsin\theta} \quad (2.21)$$

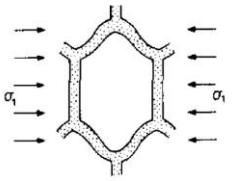

$$\delta = \frac{Pl^3 sin\theta}{12E_s I} \quad (2.22)$$

$$\frac{E_1^*}{E_s} = \left(\frac{t}{l}\right)^3 \frac{cos\theta}{(h + lsin\theta)sin^2\theta} \quad (2.23)$$

$$v_{12}^* = -\frac{\varepsilon_2}{\varepsilon_1} = \frac{cos^2\theta}{(h/l + sin\theta)sin\theta} \quad (2.24)$$

$$\frac{4}{3^{\frac{1}{2}}}\left(\frac{t}{l}\right)^3 1$$

$$C = 0$$

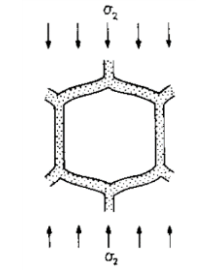

$$\sigma_2 = \frac{W}{blcos\theta} \quad (2.25)$$

$$\varepsilon_2 = \frac{\delta cos\theta}{h + lsin\theta} \quad (2.26)$$

$$\varepsilon_1 = \frac{\delta sin\theta}{lcos\theta} \quad (2.27)$$

$$\frac{E_2^*}{E_s} = \left(\frac{t}{l}\right)^3 \frac{h/l + sin\theta}{ccos^3\theta} \quad (2.28)$$

$$v_{21}^* = -\frac{\varepsilon_1}{\varepsilon_2} = \frac{(h/l + sin\theta)sin\theta}{cos^2\theta} \quad (2.29)$$

$$\frac{4}{3^{\frac{1}{2}}}\left(\frac{t}{l}\right)^3 1$$

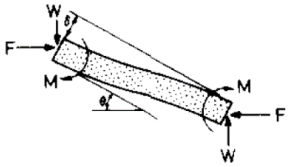

$$\delta = \frac{Wl^3 cos\theta}{12E_s I} \quad (2.30)$$

$$\tau = \frac{F}{2blcos\theta} \quad (2.31)$$

$$\gamma = \frac{2U_s}{h + lsin\theta} \quad (2.32)$$

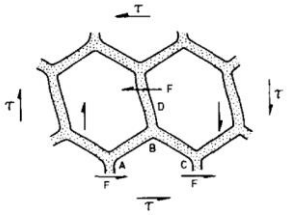

$$U_s = \frac{1}{2}\emptyset h + \frac{F\left(\frac{h}{2}\right)^3}{3E_s I} \quad (2.33)$$

$$\emptyset = \frac{Fhl}{24E_s I} \quad (2.34)$$

$$\frac{G_{12}^*}{E_s} = \left(\frac{t}{l}\right)^3 \frac{h/l + sin\theta}{\left(\frac{h}{l}\right)^2 (1 + 2h/\,l)cos\theta} \quad (2.35)$$

$$\frac{1}{3^{\frac{1}{2}}}\left(\frac{t}{l}\right)^3$$

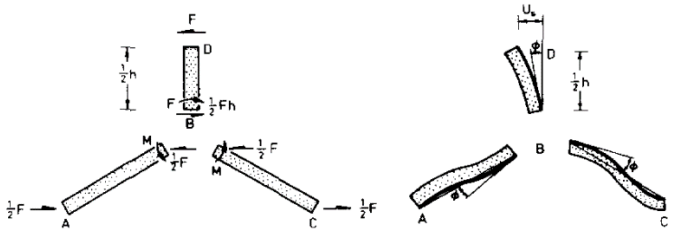

Table 6 In-plane strength of honeycombs (L.J. Gibson, 1989)

Deformed cell	*Analysis*	*Honeycomb property*	*Value of property for h/l and $\theta = 30^o$*
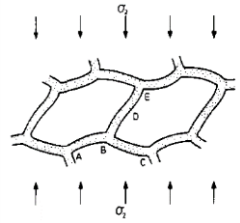	$P_{cr} = \frac{n^2\pi^2 E_s I}{h^2}$ (2.36)	$(\sigma^*_{el})_2 = \frac{n^2\pi^2}{24}\frac{t^3}{lh^2}\frac{1}{cos\theta}$ (2.38)	
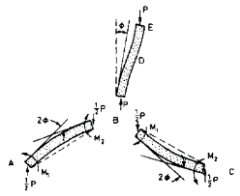	$(\sigma^*_{el})_2 = \frac{P_{cr}}{2blcos\theta}$ (2.37)	h/l | n 1 | 0.686 1.5 | 0.760 2.0 | 0.806	$0.22\left(\frac{t}{l}\right)^3 E_s$
	$\sigma_1 = \frac{P}{b(h + lsin\theta)}$ (2.39)	$\frac{(\sigma^*_{pl})_1}{\sigma_{ys}} = \left(\frac{t}{l}\right)^2 \frac{1}{2(h/l + sin\theta)sin\theta}$ (2.43)	
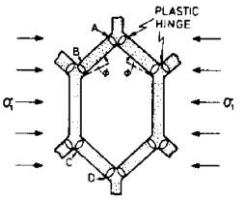	$M_{max} = \frac{Plsin\theta}{2}$ (2.40)	$\frac{(\sigma^*_{pl})_2}{\sigma_{ys}} = \left(\frac{t}{l}\right)^2 \frac{1}{2cos^2\theta}$ (2.44)	$\frac{2}{3}\left(\frac{t}{l}\right)^2$ $\frac{2}{3}\left(\frac{t}{l}\right)^2$
	$M_p = \frac{\sigma_{ys} bt^2}{4}$ (2.41)	$\frac{(\tau^*_{pl})_{12}}{\sigma_{ys}} = \left(\frac{t}{l}\right)^2 \frac{1}{(4h/l)cos\theta}$ (2.45)	$\frac{1}{2x3^{1/2}}\left(\frac{t}{l}\right)^2$
	$M_f = \frac{\sigma_{ys} bt^2}{6}$ (2.42)	$\frac{(\sigma^*_{cr})_1}{\sigma_{ys}} = \left(\frac{t}{l}\right)^2 \frac{1}{3(h/l + sin\theta)sin\theta}$ (2.46)	$\frac{4}{9}\left(\frac{t}{l}\right)^2$
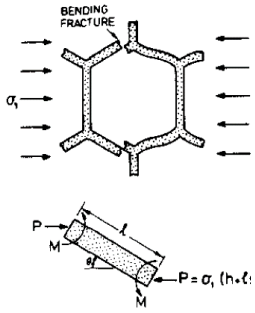		$\frac{(\sigma^*_{cr})_2}{\sigma_{fs}} = \left(\frac{t}{l}\right)^2 \frac{1}{3cos^2\theta}$ (2.47)	$\frac{4}{9}\left(\frac{t}{l}\right)^2$

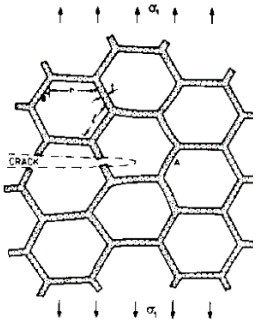

$$\sigma_1 = \frac{P}{b(h + lsin\theta)} \quad (2.48)$$

$$\sigma_{loc} = \sigma_1 \frac{(\pi c)^{\frac{1}{2}}}{(2\pi r)^{\frac{1}{2}}} \quad (2.49)$$

$$r = \frac{(h + lsin\theta)}{2} \quad (2.50)$$

$$M_1 \propto Plsin\theta$$

$$\propto = \frac{\sigma_{fs} bt^2}{6}$$

$$\frac{(\sigma_f^*)_1}{\sigma_{ys}} = \left(\frac{t}{l}\right)^2 \frac{1}{6(h/l + sin\theta)^{\frac{1}{2}} sin\theta} \left(\frac{l}{c}\right)^{\frac{1}{2}} \quad (2.51)$$

(1.51)

$$0.3\left(\frac{l}{c}\right)^{1/2}\left(\frac{t}{l}\right)^2$$

$$\frac{(\sigma_f^*)_2}{\sigma_{fs}} = \left(\frac{t}{l}\right)^2 \frac{1}{3x2^{\frac{1}{2}} cos^{\frac{3}{2}}\theta} \left(\frac{l}{c}\right)^{\frac{1}{2}} \quad (2.52)$$

$$0.3\left(\frac{l}{c}\right)^{1/2}\left(\frac{t}{l}\right)^2$$

If a load is applied uniaxially in the plane of the hexagonal cells, the cell walls of the honeycomb will bend initially (taking into account that the wall thickness, t, must be small in comparison with the wall length, l). The Young's modulus, E^* can be related with the relative density, ρ^*/ρ_s, the modulus solid, E_s, and the cell geometry $(h/l, \theta)$ using structural mechanics. A stress σ_1 acting in the x_1 direction induces a load P on the end of the inclined cell wall:

$$P = \sigma_1(h + lsin\theta)b \quad (2.53)$$

Where b is the wall thickness. The wall deflects by:

$$\delta = \frac{Pl^3 sin\theta}{12E_s I} \quad (2.54)$$

Where E_s is the Young's modulus of the solid cell wall material, and I is the moment of inertia of the wall cross section $(I = bt^3/12)$. The strain in the x_1 direction on is, then:

$$\varepsilon = \frac{\delta sin\theta}{lcos\theta} = \frac{\sigma_1(h + lsin\theta)bl^2 sin^2\theta}{12E_s I cos\theta} \quad (2.55)$$

The Young's modulus parallel to x_1 is then:

$$\frac{E_1^*}{E_s} = \left(\frac{t}{l}\right)^3 \frac{cos\theta}{(h + lsin\theta)sin^2\theta} \quad (2.56)$$

The Young's modulus for the loading in the x_2 direction and the shear modulus for loading in the $x_1 - x_2$ plane can be reviewed in the book of Gibson and Ashby, (L.J. Gibson & Ashby, 1989).

The Poisson's ratios are found by taking the negative ratio of the average strain to and parallel to the loading. Ignoring the shear and axial deformation, it is observed that they depend only upon the cell shape.

With a sufficiently high load, cells collapse by elastic buckling, plastic yielding or brittle crushing, depending on the properties of the cell wall material. The elastic buckling collapse stress is related to the Euler buckling load, P_{crit}, of the vertical column. Table 6 shows the Equation. (2.36).

The plastic collapse stress can be calculated from the plastic moment to form plastic hinges in the cell walls while the brittle crushing stress can be calculated from the modulus of rupture required to fracture walls, (L.J. Gibson & Ashby, 1989)(Table 6).

When applying the load in the primary axis, along the out-of-plane direction, the cell walls of a honeycomb initially compress axially. This means that Young's modulus varies merely with the volume fraction of solid, or with the relative density, Equation. (2.57) of Table 7.
If buckling is avoided, the yield strength and brittle crushing strength for loading in the x_3 the direction also vary directly with the relative density. The stresses corresponding to elastic and plastic buckling are presented in Table 7.

Table 7 Out-of-plane properties of honeycombs (Lorna J. Gibson, 2005)

Deformed cell	*Honeycomb property*	
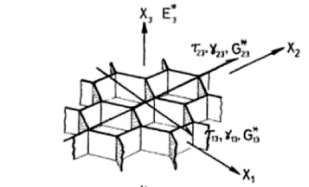	$\frac{E_3^*}{E_s} = \frac{\rho^*}{\rho_s}$	(2.57)
	$v_{31}^* = v_{32}^* = v_s^*$	(2.58)
	$v_{13}^* \sim v_{23}^* \sim 0$	(2.59)
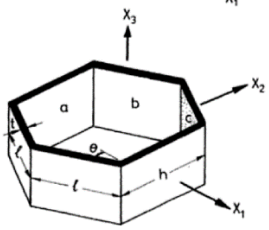	$\frac{G_{13}^*}{G_s} = \frac{G_{23}^*}{G_s} = 0.577\left(\frac{t}{l}\right)$	(2.60)
	$(regular\ hexagons)$	
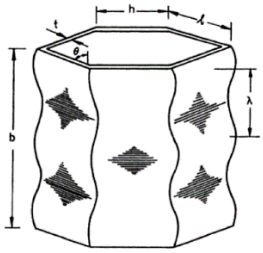	$\frac{(\sigma_{el}^*)_3}{E_s} \sim \left(\frac{t}{l}\right)^3 \frac{2}{1-v_s^2} \frac{\frac{l}{h}+2}{(h/l+sin\theta)cos\theta}$	(2.61)
	$(elastic\ buckling)$	
	$\frac{(\sigma_{pl}^*)_3}{\sigma_{ys}} = 5.6\left(\frac{t}{l}\right)^{\frac{5}{3}}$	(2.62)
	$plastic\ buckling: (regular\ hexagons)$	

2.3. TRIPLY PERIODIC MINIMAL SURFACE

Architecture foams that are based on the known mathematical triply periodic minimal surface (TPMS) have regular and smooth geometries without discontinuities and are being investigated as a novel and attractive alternative for their mechanical performance (Brakke, 1992),(Torquato, 2005). The TPMS-based foams can be used as lightweight cellular materials for many technological applications, including acoustic absorption, battery electrodes, and catalyst support. The successful use of TPMS-based architecture foams will require knowledge of their mechanical properties.

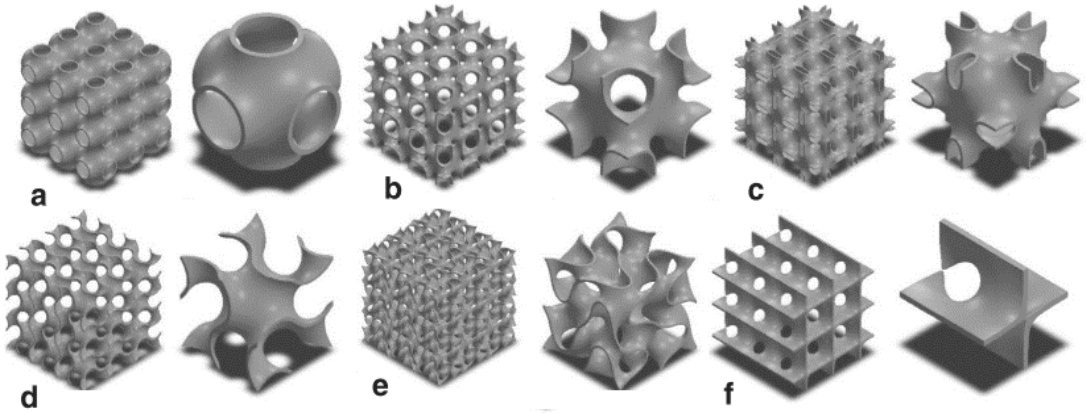

Figure 19 Triply periodic minimal surface (TPMS); (a) Primitive, (b) Neovius, (d) Gyroid, (e) Fischer-Koch, (f) CLP, (Abueidda et al., 2016).

Triply periodic minimal surfaces are minimal surfaces and have regular and smooth structures with symmetries of a crystallographic group such as cubic, tetragonal, rhombohedral, and orthorhombic symmetries. TPMS is infinite and periodic in three independent directions (Kapfer, Hyde, Mecke, Arns, & Schroder-Turk, 2011). Compared to lattice-based architectures, TPMS-sheets do not have joints and structs so that they might have a significant advantage over lattices regarding manufacturing and efficient properties of cellular materials. For example, Khaderi, Deshpande, & Fleck, (2014) investigated the mechanical properties of the gyroid lattice computationally under various loading conditions. They concluded that imperfections in the common locations within the lattice give rise to a harsh breakdown in elastic and plastic properties. TPMS-sheets are periodic microstructures continuously and smoothly interconnected in the 3D space as compared to the lattices, which provide better integrity for TPMS-sheets structures and composites.

TPMS are discovered in biological systems (weevils, butterfly and beetle shells) (M. G. Lee, Lee, Han, & Kang, 2016) (Kapfer et al., 2011). Researchers utilised TPMS to produce materials with superior physical and mechanical properties (Torquato, Hyun, & Donev, 2002). More specifically, TPMS have been used to produce multifunctional two-phase composites with enhanced properties (Kapfer et al., 2011). When TPMS are used in two-phase composites, TPMS can be used as TPMS-sheet based 3D reinforcements (Torquato et al., 2002). Based on level-set method topology optimization (Guest & Prévost, 2007) of TPMS surface based reinforced composites, it was found that the ones with the Schwartz Primitive (P) and Diamond (D) minimal surfaces as the phase interface possess maximal bulk modulus and conductivity (Guest & Prévost, 2007), (Torquato et al., 2002). Schwartz Primitive (P) TPMS surface based cellular solids were found to have maximum stiffness and fluid permeability (Guest & Prévost, 2006).

Recently, Primitive, Diamond and gyroid TPMS sheet-based metamaterials were studied (W. Lee, Kang, Song, Moon, & Kim, 2016). The effects of volume fraction and material properties on the stiffness of triply periodic bicontinuous structure were investigated. It was demonstrated that there exists a remarkable range of stiffness of triply periodic bicontinuous structures of mechanical metamaterials.

2.4. ULTRALOW-DENSITY MATERIAL (SHELLULAR)

Recently, a new ultralow-density material composed of continuous shells “Shellular” was introduced. Shellular has the typical hierarchical architecture across multiple scales, and its

constituent material is a plated metallic film with nano-sized grains, providing a great extent of strength well over 1GPa. This new material is developed for supporting loads at the very low density and considered to have modified geometry of Schwarz Primitive TPMS (M. G. Lee et al., 2016), (B. D. Nguyen, Cho, & Kang, 2016).

Furthermore, Shellular is expected to overcome the problems caused by geometrical incompleteness, stress concentration, and flaws or imperfections that were often found in previous ultralow-density-materials composed of hollow trusses.

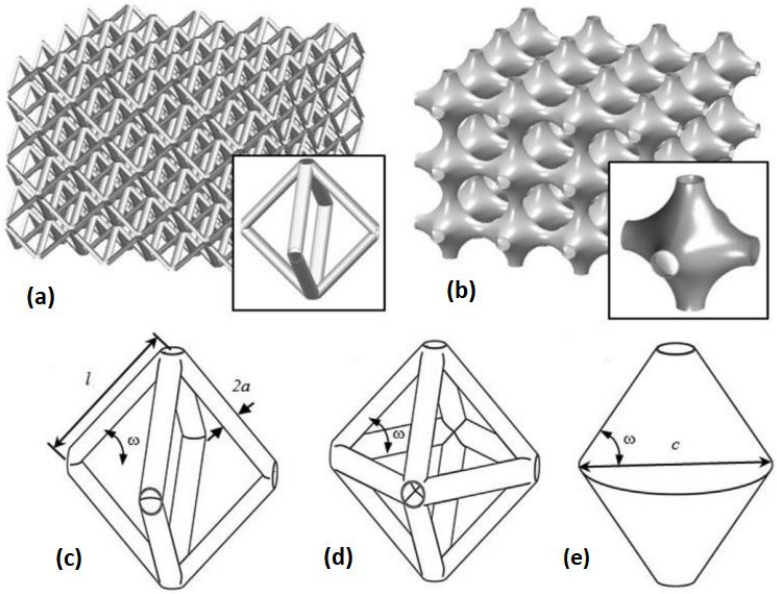

Figure 20 Configurations of (a) Microlattice and (b) Shellular with enlarged views of their unit cells, and configurations of single unit cells of (c) Microlattice, (d) a hollow octahedron truss PCM, and (e) a truncated conical shell as an idealized formation of. (M. G. Lee et al., 2016)

Chapter 3

NUMERICAL METHOD: FORMULATION

3.1. Finite element method

In order to create the mesh in FEM, it is fundamental to first divide the domain along its x and y directions in order to create the nodes. In some geometries, regular meshes are not available so it is necessary to create irregular meshes to avoid these geometriy issues. The following equation applies:

$$x_{irregular} = x_{regular} + \frac{rand - 0.5}{0.5} \cdot \frac{L}{\delta x * \lambda}$$
$$y_{irregular} = y_{regular} + \frac{rand - 0.5}{0.5} \cdot \frac{L}{\delta y * \lambda} \quad (3.1)$$

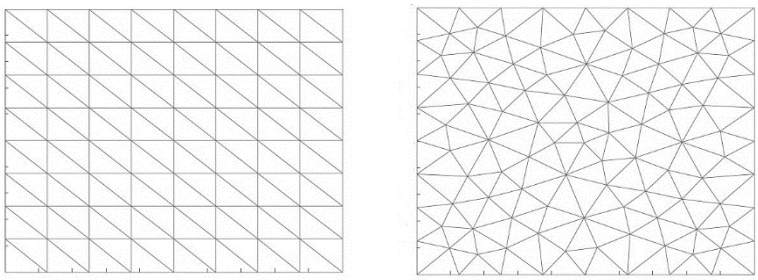

Figure 21 Regular mesh (left) and irregular mesh (right)

Where rand is a random number between 1 and -1 and λ a parameter to set the degree of irregularity, where lower values for this parameter generate a more irregular nodal mesh. Having created the nodes, it is time to establish the elements. For this, it is necessary to choose the type of element that will be used, taking into account the type of problem. The main difference is whether to work in 2D or 3D.

A two dimensional (2D) finite element has two standard geometries: quadrilateral or triangle. An example of the 2D triangle element and quadrilateral is,

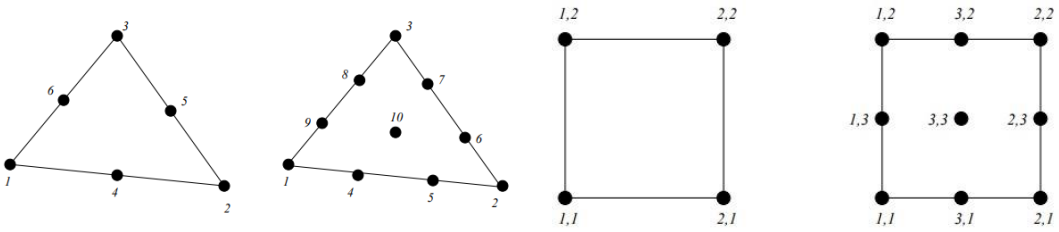

Figure 22 - Examples of different types of 2D elements (Eaton, 2005).

A three dimensional (3D) finite element offers more variety. There is an essential list of different types of elements, where the most representatives are the tetrahedron and the hexahedron. An example of a 3D element shown in Figure 23.

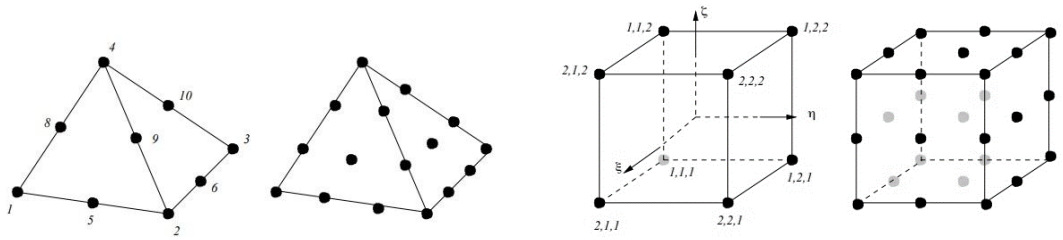

Figure 23 Examples of different types of 3D elements (Eaton, 2005).

3.1.1. Integration Points

With the elements already set, the following step is to create integration points for each element, using local coordinates. The number of integration points is chosen according to the difficulty of the problem, or because of the necessity to arrive at the most accurate result, as illustrated in Figure 24 - Example quadrilateral "element" with 2x2 integration points.

Table 8 - Gaussian quadrature coordinates and weights

Number of points (n)	Points (x_I)	Weights (w_I)
1	0	2
2	$\pm\sqrt{\frac{1}{3}}$	1
3	0	$\frac{8}{9}$
	$\pm\sqrt{\frac{3}{5}}$	$\frac{5}{9}$
4	$\sqrt{\frac{3}{7}-\frac{2}{7}\sqrt{\frac{6}{5}}}$	$\frac{18+\sqrt{30}}{36}$
	$\sqrt{\frac{3}{7}+\frac{2}{7}\sqrt{\frac{6}{5}}}$	$\frac{18-\sqrt{30}}{36}$
5	0	$\frac{128}{225}$
	$\pm\frac{1}{3}\sqrt{5-2\sqrt{\frac{10}{7}}}$	$\frac{322+13\sqrt{70}}{900}$
	$\pm\frac{1}{3}\sqrt{5+2\sqrt{\frac{10}{7}}}$	$\frac{322-13\sqrt{70}}{900}$

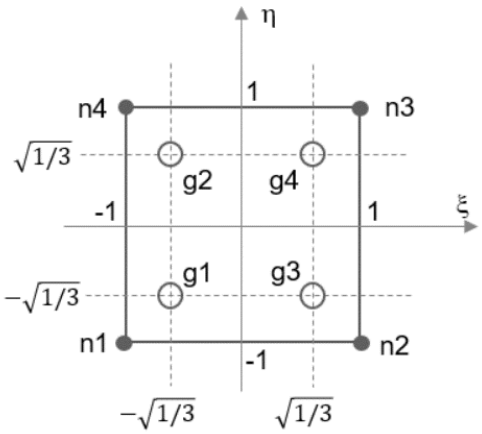

Figure 24 - Example quadrilateral "element" with 2x2 integration points

3.1.2. Shape Functions

The shape function is also dependent on the user. The central aspect of this function is that it converts values for any point in the element, from their local coordinate to the global coordinate values. It is recommended to review the Ziennkiewicz & Taylor (2005) book in order to deepen the concept of shape functions.

Taking into account the local coordinates of an element, ξ and η, the way to define the shape functions in FEM begins by defining a matrix [C] of size $n \times n$, being n the number of nodes of the element. For an element with four nodes the [C] matrix would look like:

$$[C] = \begin{bmatrix} 1 & \xi_1 & \eta_1 & \xi_1\eta_1 \\ 1 & \xi_2 & \eta_2 & \xi_2\eta_2 \\ 1 & \xi_3 & \eta_3 & \xi_3\eta_3 \\ 1 & \xi_3 & \eta_3 & \xi_4\eta_4 \end{bmatrix} \tag{3.2}$$

Depending on the element's number of nodes and their distribution, the terms of the matrix [C] have to be chosen using the Pascal triangle shown in Figure 25.

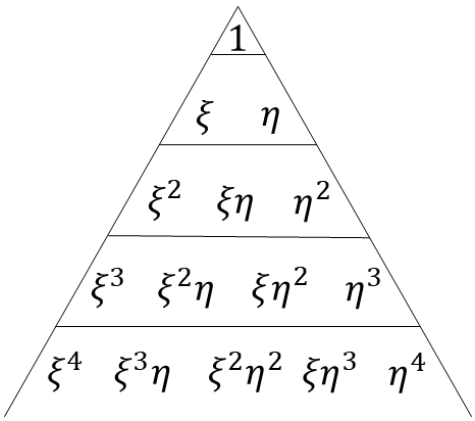

Figure 25 - 2D Pascal Triangle

The shape functions of the element are defined as follows:

$$N_n = \{P\}[C]^{-1} \tag{3.3}$$

Where {P} is a vector of polynomials, also dependent on the Pascal triangle, with size $1 \times n$. In the case of the four nodes element exemplified, the vector would be:

$$\{P\} = \{1 \quad \xi \quad \eta \quad \xi\eta\} \tag{3.4}$$

If the coordinates of a node are input in {P}, the values of the shape function should be equal to 0 for all the shape functions except the shape function corresponding to that node.

To obtain the derivatives of the shape function in ξ and η, the polynomial has to be derived in the corresponding variable and then multiplied by the inverse of [C]. The derivatives of the polynomial are shown as follows:

$$\begin{matrix} \{\partial P/\partial\xi\} = \{\partial 1/\partial\xi & \xi/\partial\xi & \eta/\partial\xi & \xi\eta/\partial\xi\} = \{0 & 1 & 0 & \eta\} \\ \{\partial P/\partial\eta\} = \{\partial 1/\partial\eta & \xi/\partial\eta & \eta/\partial\eta & \xi\eta/\partial\eta\} = \{0 & 0 & 1 & \xi\} \end{matrix} \tag{3.2}$$

The resulting derivatives of the shape functions would then be:

$$\begin{matrix} \partial N_n/\partial\xi = \{\partial P/\partial\xi\}[C]^{-1} \\ \partial N_n/\partial\eta = \{\partial P/\partial\eta\}[C]^{-1} \end{matrix} \tag{3.3}$$

Having calculated the derivatives, it is possible to calculate the Jacobian matrix of each Gauss point by the following operation:

$$[J_I] = \begin{bmatrix} \frac{\partial N_1}{\partial\xi} & \cdots & \frac{\partial N_n}{\partial\xi} \\ \frac{\partial N_1}{\partial\eta} & \cdots & \frac{\partial N_n}{\partial\eta} \end{bmatrix} \begin{bmatrix} x_1 & x_2 \\ \vdots & \vdots \\ x_n & y_n \end{bmatrix} \tag{3.4}$$

It is possible to obtain the integration weight after having calculated the Jacobian matrix for each Gauss point in the element.

$$W_I = |J_I| w_{\xi_I} w_{\eta_I} \tag{3.5}$$

Where w_ξ and w_η are the weights of the respective coordinate (Table 8), depending on the chosen number of integration points per axis.

The Jacobian matrix is also used to calculate the derivatives of the shape function with respect to x and y at each Gauss point:

$$\begin{bmatrix} \frac{\partial N_1}{\partial x} & \cdots & \frac{\partial N_n}{\partial x} \\ \frac{\partial N_1}{\partial y} & \cdots & \frac{\partial N_n}{\partial y} \end{bmatrix} = [J_I]^{-1} \begin{bmatrix} \frac{\partial N_1}{\partial\xi} & \cdots & \frac{\partial N_n}{\partial\xi} \\ \frac{\partial N_1}{\partial\eta} & \cdots & \frac{\partial N_n}{\partial\eta} \end{bmatrix} \tag{3.6}$$

The shape functions are also used in FEM to convert the coordinates of the Gauss points from their local coordinates to the global coordinates:

$$\{x_I \quad y_I\} = [N_1 \quad N_2 \quad N_3 \quad N_4] \cdot \begin{bmatrix} x_{n1} & y_{n1} \\ x_{n2} & y_{n2} \\ x_{n3} & y_{n3} \\ x_{n4} & y_{n4} \end{bmatrix} \tag{3.10}$$

3.2. Meshless method

3.2.1. Node Generation

The discretisation in meshless does not require a mesh, only the spatial location of each node that discretises the problem domain. This discretisation is very similar to mesh creation in FEM as explained in section 3.1.

First of all, the domain is divided along its x and y directions to create the nodes. The nodes can also be made regular and irregular, following Equation (3.1) and as illustrated in Figure 26.

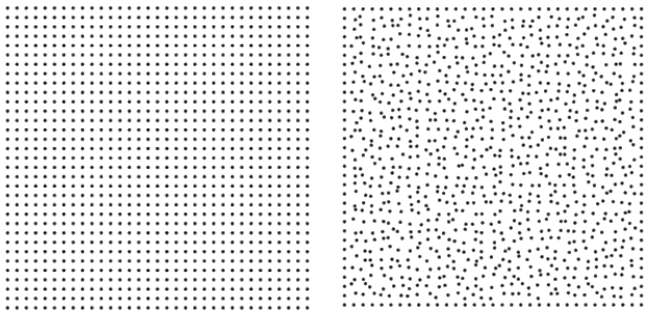

Figure 26 Regular mesh (left) and irregular mesh (right)

The nodal density discretisation affects the accuracy of the result as in FEM, but also affects the computational cost, so it is important to arrive at a balance between accuracy and computational cost. This is possible by just increasing the number of nodes in the areas that present a predictable stress concentration.

3.2.2. Integration Points

The following step is to create the integration mesh, that can be nodal dependent or independent, required for many numerical methods in order to numerically integrate the weak form equations that are governing the physics phenomenon.

Commonly, these interest points are the integration points and, in most meshless methods, use a background mesh to generate the integration points, as this is a simple and effective way to generate them. This provides some flexibility in the integration points generation and differs from the FEM where the integration points are mesh-dependent. The size of the integration mesh does not have a significant effect on the final results (T. Belytschko, Lu, & Gu, 1994).

Usually, Gaussian integration meshes are applied, as in the FEM (section 3.1.1). However, another approach is also valid for integrating the weak form equations using the nodal integration, which refers to the Voronoï diagrams used to obtain each node weight.

As can be perceived, using nodal integration, the nodal distribution acts as an integration mesh. This generates a decrease of the accuracy, and it becomes necessary to carry out a stabilisation process that increases the computational cost (J. Chen, Wu, & Yoon (2001); Elmer, Chen, Puso, & Taciroglu (2012)).

Having the nodal distribution and the integration mesh constructed, it is possible to impose the nodal connectivity. As it is known, the nodal connectivity in FEM is done by elements; however, in meshless methods, it is not. Because of this, for an interest point x_I, of the problem, it is characterised by areas or volumes that belong to the influence domain of node

x_i. In meshless, the interest point is equivalent with the integration point from the background of the integration mesh. However, there is a method that uses the nodes of the nodal discretisation as an interest point, such as the collocation point methodology or the nodal integration scheme. In meshless, it is recommended that all of the influence domain has the same number of nodes because the influence domain is dependent on the nodal density around the interest point.

Afterwards, using the interpolation or approximation function, the field variable can be obtained. In this method, $\boldsymbol{u_I} = (u_x u_y u_z)$, the displacement components in any interest point x_I, are approximated or interpolated using the nodal displacement of the nodes inside the influence domain around the interest point.

$$\boldsymbol{u}(\boldsymbol{x}_I) = \sum_{i=1}^{n} \varphi_i(\boldsymbol{x}_i)\boldsymbol{u}(\boldsymbol{x}_i) \tag{3.11}$$

Where n is the number of nodes inside the influence domain of the interest point, $u(x_i)$ represents the displacement components of each node inside the influence domain and $\varphi_i(x_i)$ is the interpolation or approximation function value of each node inside the influence domain.

The following step is establishing the equation system using the interpolation or approximation functions and applying to the strong or weak form formulation. The weak form Galerkin uses the meshless method, and the discrete equations can be obtained by applying to the differential equation governing the physic phenomenon the weighted residual method of Galerkin (B.G.Galerkin, 1915). Depending on whether it studies a static or a dynamic problem, the global result equation matrix will to be composed by an algebraic equation or differential equation.

3.2.3. Influence domain

The connectivity between nodes is obtained by the overlap of the influence domain of each node. This influence domain is going to change depending on the approximate function that will be used. It is typically a fixed area or fixed volume, independent of whether it is a2D or 3D problem. However, it has been demonstrated that the variation of the influence domain along the problem affects the performance and the final solution. For this reason, it is recommended that a convergence study is performed to find the better number of the nodes inside the influence domain, so that the subsequent work begins with these conditions. Previous works suggest that each influence domain should have between n= [9,16] it is mean [3,8,9,11]. The referential dimension d is established using the Equation. (3.12).

$$d = k \times h \tag{3.12}$$

Where h is the average of the nodal space in the surroundings of the interest point and k is the dimensionless parameter ranging between [1.5,2.5]. It is important to remark that it is not the most appropriate technique but it is the most commonly used to establish the nodal connectivity. Typically, the influence domains are: rectangular, fixed circular and variable circular. The first two types can lead to the loss of accuracy in the numerical analysis. For this reason, the third one was proposed as it allows to maintain the constant connectivity along the solid domain. This technique allows solving the problem that the fixed influence domain usually

presents at the boundary conditions. It also constructs shape functions with the same degree of complexity in the complete domain.

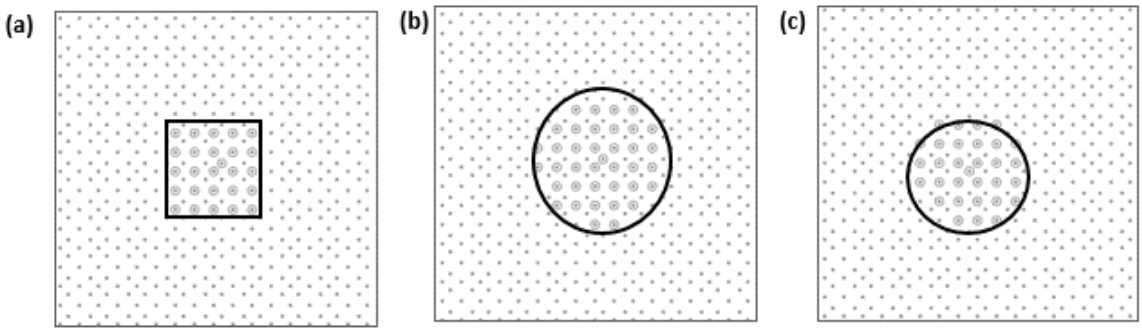

Figure 27 (a) Fixed rectangular influence domain. (b) Fixed circular influence domain. (c) Flexible circular influence domain

3.2.4. Integration mesh

In the FEM, the element mesh is coincident with the integration mesh. This is possible since the shape functions are known polynomial functions, so the number of integration points per integration cell can be determined using accurate relationships (J. Belinha, Dinis, & Jorge, 2009). In the case of the meshless method, the degree of the shape function usually is unknown, so it is not possible to define the background integration mesh.

The greatest challenge in the meshless method is to establishe the numerical integration. For this reason, it is so important to develop convergence studies to arrive at the optimal relationship between the density of the field node and the density of the background integration mesh. Also, the variation of the shape function forces testing through convergence studies for finding the best options or combinations between quadrature, influence domain and density of the field node.

3.2.5. Natural Neighbours and Influence Cells

As presented in the section 3.2.2, there is another approach other than using the influence domains: influence cells. This is performed using the Voronoï diagrams and Delaunay triangulation. Also, this constitutes the basis of the NNRPIM methods that are going to be the applied in this work (Dinis, Natal Jorge, & Belinha, 2007).

Consider the nodal set $\boldsymbol{N} = \{n_1, n_2, \dots, n_N\}$ discretising in the space domain $\Omega \subset \mathbb{R}^d$ with $\boldsymbol{X} = \{\boldsymbol{x_1}, \boldsymbol{x_2}, \dots, \boldsymbol{x_n}\} \in \Omega$. The Voronoï diagram of $\boldsymbol{N}$ is the partition of the function space discretised by $\boldsymbol{X}$ in sub-regions V_i, closed and convex, being each of those sub-regions associated with the node i, n_i, such that any point inside V_i is closer to n_i than any other node $n_j \in N \wedge j \neq i$. The set of these sub-regions $V = \{V_1, V_2, \dots, V_N\}$ defines the Voronoï diagram. Mathematically, the Voronoï cell is defined by:

$$V_i = \left\{x_I \in \Omega \subset \mathbb{R}^2 : \|x_I, x_i\| < \left\|x_I, x_j\right\|, \quad \forall\, i \neq j\right\} \tag{3.13}$$

Where x_I is an interest point of the domain, and $\|\cdot\|$ is the Euclidian metric norm.

In order to visualise how Voronoï diagrams can be obtained, space is going to be reduce to 2D because it makes it easier to understand. Firstly, consider the set of nodes in Figure 28(a).

To find the Voronoï cell of node n_o, one of the other nodes has to be selected first as a potential neighbour. If the node n_4 is selected, as in Figure 28(b), then the normal vector u_{40} given by:

$$u_{40} = \frac{x_0 - x_4}{\|x_0 - x_4\|} \tag{3.14}$$

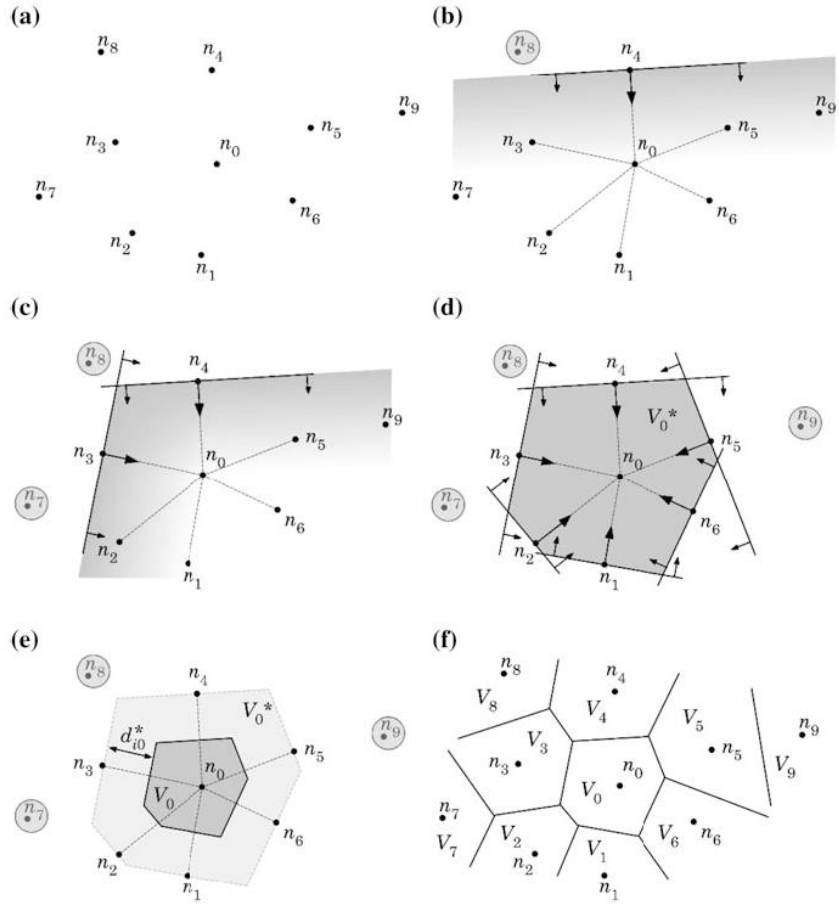

Figure 28 – (a) Initial nodal set of potential neighbour nodes of the node n_0. (b) First trial plane. (c) Second trial plane. (d) Final trial cell containing just the natural neighbours of node n_0. (e). Node n_0 Voronoï cell V_o. (f) Voronoï diagram (Jorge Belinha, 2014a)

Where $u_{40} = \{u_{40}, v_{40}, w_{40}\}$, and with is component, it is possible to define the plane π_{40}:

$$u_{40}x + v_{40}y + w_{40}z = (u_{40}x_4 + v_{40}y_4 + w_{40}z_4) \tag{3.15}$$

Having the plane defined, it is possible to exclude as natural neighbours all the nodes that not respect the following condition:

$$u_{40}x + v_{40}y + w_{40}z \leq (u_{40}x_4 + v_{40}y_4 + w_{40}z_4) \tag{3.16}$$

It is possible to see in Figure 28(b) the exclusion of n_8 as a natural neighbour of n_0. This process is then repeated using another node. Figure 28(d) shows the six natural neighbours of a node of n_0 that respect, simultaneously, the following six conditions:

$$\begin{cases} u_{10}x + v_{10}y + w_{10}z \leq (u_{10}x_1 + v_{10}y_1 + w_{10}z_1) \\ u_{20}x + v_{20}y + w_{20}z \leq (u_{20}x_2 + v_{20}y_2 + w_{20}z_2) \\ \vdots \\ u_{60}x + v_{60}y + w_{60}z \leq (u_{60}x_6 + v_{60}y_6 + w_{60}z_6) \end{cases} \tag{3.17}$$

Only the nodes on the perimeter of the domain V_0^* are considered neighbour nodes. The Voronoï cells of n_0 can then be seen in Figure 28(e) and it is the homothetic form of the auxiliary domain V_0^*, where:

$$d_{0i}^* = \frac{d_{0i}}{2} = \frac{\|x_0 - x_i\|}{2} \tag{3.18}$$

The same process is then used to determine the Voronoï cells of the rest of the nodes in the domain, and the result is seen in Figure 28(f).

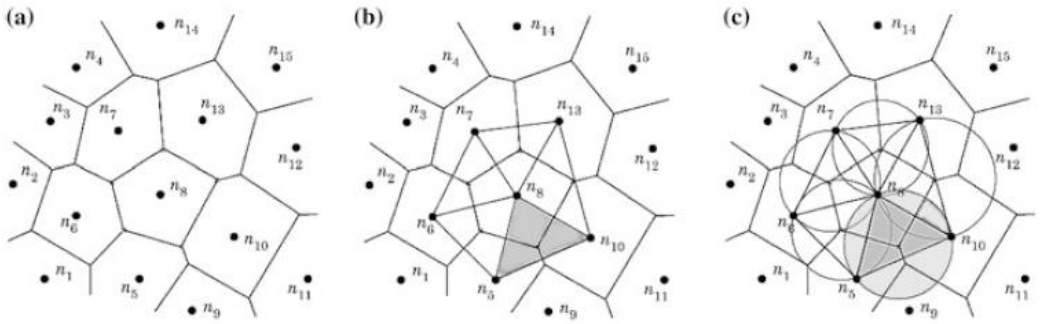

Figure 29 - (a) Voronoï diagram (b) Delaunay Triangulation (c) Natural neighbour circumcircle (Jorge Belinha, 2014a)

The Delaunay triangulation is the geometrical dual of the Voronoï diagram and it is constructed by connecting the nodes that have Voronoï cells with common boundaries. The duality between the Voronoï diagram and the Delaunay triangulation means that there is a Delaunay edge between two nodes in a plane, if and only if their Voronoï cells share a common edge. An important property of the Delaunay triangles is the "empty circumcircle criterion" (Jorge Belinha, 2014a). If a set of nodes $N_t = \{n_j, n_k, n_l\} \in \mathbf{N}$ forms a Delaunay triangle, then the circumcircle formed by that triangle contains only the nodes of N_t and no other nodes of the global set $\mathbf{N}$. The centre of the natural neighbour circumcircle is the vertex that is shared by all Voronoï cells. These properties of the Delaunay triangulation are shown in Figure 29.

In NNRPIM, the Voronoï diagram is used to create the "influence-cells", which enforce the nodal connectivity between the nodes that discretise the domain. In this method, there are two degrees of influence-cells.

The "first-degree influence-cell" of an interest point x_I is found by searching for its natural neighbours, following the Natural Neighbour Voronoï construction. So, the first-degree influence-cell is composed only by these first natural neighbours, as seen in Figure 30(a).

The "second-degree influence-cell" of an interest point x_I is found by following the same procedure to find the neighbour nodes as in the first-degree influence-cell. Then, based on the Voronoï diagram previously constructed, the natural neighbours of the first natural neighbours x_I are added to the influence-cell, Figure 30(b).

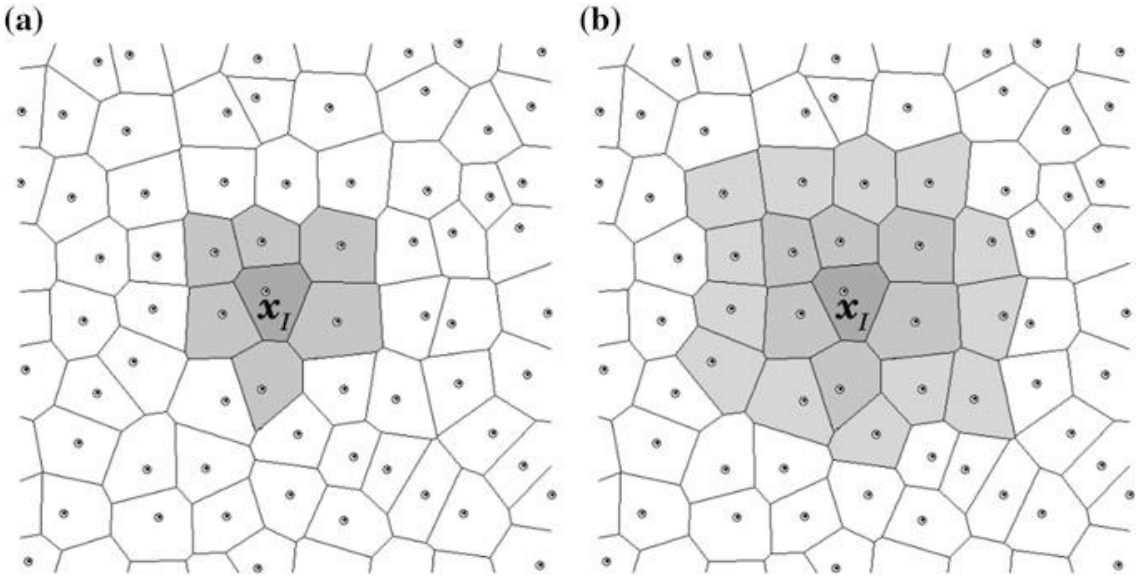

Figure 30 – (a) 1st degree influence-cells (b) 2nd degree influence-cells (Jorge Belinha, 2014a)

3.2.6. Shape functions

Shape functions are used to approximate the unknown field functions that permit solving the partial differential equations with which it is possible to obtain the numerical solution of a physical phenomenon.

That is known as the meshless method. The domain is discretised in a nodal mesh, which can have a regular distribution or not. Because the method does not have an element,it is necessary to use an interpolation or approximation technique that can move the local nodal domain, to allow the construction of the meshless shape function for the approximation of the field variable.

The two more-common shape function construction techniques are the approximation shape function approach and the interpolation shape function approach. In both cases, they are constructed for an arbitrary interest point that only uses a small set of field nodes. The area that forms the vicinity group of nodes with respect to the interest point is called the support domain, which usually coincides with the influence domain. The shape function assumes non-zero values inside the support-domain and it is null outside. It is important to remark that when working with solids, the shape function and the weight are usually the same; this is known as the Galerkin method (B.G.Galerkin, 1915).

One of the most important characteristics that the shape function must have is to be computationally efficient in order to be a proficient FEM alternative. Additionally, it has to be numerically stable, present a particular order of consistency, be compactly supported, compatible, and in the best case, satisfy the Kronecker delta property (J. Chen et al., 2001).

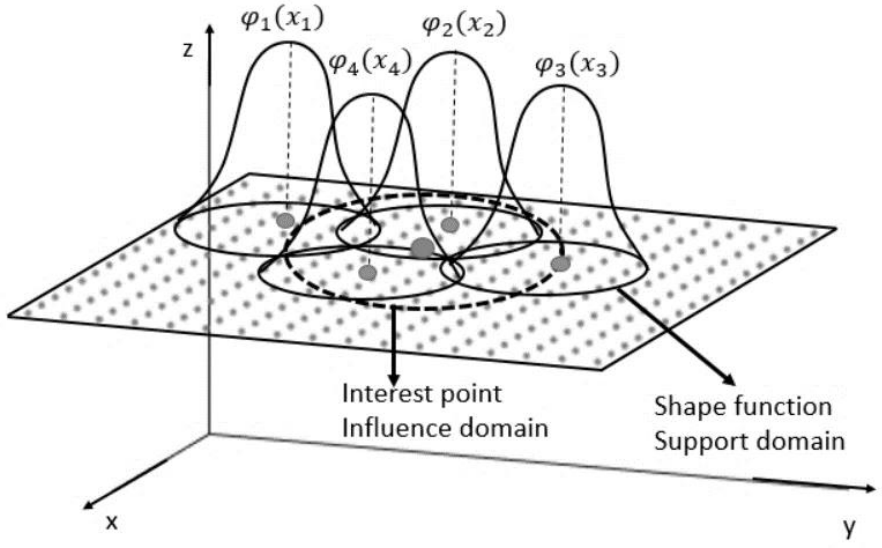

Figure 31 Representation of a generic influence domain

3.2.7. Natural Neighbours Radial Point Interpolation Method

Using the NNRPIM, the shape function construction presents more complexity than for the FEM. Considering $u(\boldsymbol{x_I})$ a function in the domain $\Omega \subset \mathbb{R}^{\mathrm{d}}$ discretised by a set of nodes N with coordinates $\boldsymbol{X} = \{\boldsymbol{x}_1, \boldsymbol{x}_2, \dots, \boldsymbol{x}_N\}$, it is possible to define, for an interest point $\boldsymbol{x_I} \in \mathbb{R}^d$, not necessarily coincident with X that defines the coordinates of a set of nodes N, the radial point interpolation function $u(\boldsymbol{x_I})$ as (Belinha, 2014):

$$u^h(\boldsymbol{x_I}) = \sum_{i=1}^{n} r_i(\boldsymbol{x_i} - \boldsymbol{x_I}) a_i(\boldsymbol{x_I}) + \sum_{j=1}^{m} p_j(\boldsymbol{x_I}) b_j\,(\boldsymbol{x_I}) = \boldsymbol{r}(\boldsymbol{x_I})^T \boldsymbol{a}(\boldsymbol{x_I}) + \boldsymbol{p}(\boldsymbol{x_I})^T \boldsymbol{b}(\boldsymbol{x_I}) \tag{3.19}$$

With $a_i(\boldsymbol{x_I})$ and $b_j(\boldsymbol{x_I})$ being the non-constant coefficients of $\boldsymbol{r}(\boldsymbol{x_I})$ and $\boldsymbol{p}(\boldsymbol{x_I})$ respectively, which can be defined as:

$$\boldsymbol{a}(\boldsymbol{x_I}) = \{a_1(\boldsymbol{x_I}) \quad a_2(\boldsymbol{x_I}) \quad \cdots \quad a_n(\boldsymbol{x_I})\}^T \tag{3.20}$$
$$\boldsymbol{b}(\boldsymbol{x_I}) = \{b_1(\boldsymbol{x_I}) \quad b_2(\boldsymbol{x_I}) \quad \cdots \quad b_m(\boldsymbol{x_I})\}^T \tag{3.21}$$

Where n is the number of nodes inside the influence cell of the interest point $\boldsymbol{x}_I$ and m is the number of a monomial of the complete polynomial basis $p_j(\boldsymbol{x}_I)$, which can be defined with the help of the Pascal triangle (Figure 25), having the following vector form:

$$\boldsymbol{p}(\boldsymbol{x_I}) = \{p_1(\boldsymbol{x_I}) \quad p_2(\boldsymbol{x_I}) \quad \cdots \quad p_m(\boldsymbol{x_I})\}^T \tag{3.22}$$

The radial basis function (RBF) can be defined as:

$$\begin{aligned} \boldsymbol{r}(\boldsymbol{x_I}) &= \{r_1(\boldsymbol{x_I}) \quad r_2(\boldsymbol{x_I}) \quad \cdots \quad r_n(\boldsymbol{x_I})\}^T \\ &= \{r(\boldsymbol{x_1} - \boldsymbol{x_I}) \quad r(\boldsymbol{x_2} - \boldsymbol{x_I}) \quad \cdots \quad r(\boldsymbol{x_n} - \boldsymbol{x_I})\}^T \end{aligned} \tag{3.23}$$

The only variable in the RBF is the Euclidean norm between the nodes and the integration point, d_{iI}, which can be defined, for three-dimensional space, as:

$$d_{iI} = \sqrt{(x_i - x_I)^2 + (y_i - y_I)^2 + (z_i - z_I)^2} \tag{3.24}$$

There are many different RBF that can be incorporated into the RPI formulation (Jorge Belinha, 2014a; J. G. Wang & Liu, 2002a, 2002b). The most commonly used globally supported RBFs are the multi-quadrics (MQ) function, the Gaussian function and the thin plate spline function (Jorge Belinha, 2014a). Because the work presented herein used a program that used the MQ to apply the meshless method, its mathematical expression is shown as follows:

$$r_i(\boldsymbol{x_I}) = (d_{il}^2 + (\gamma d_a)^2)^p \tag{3.25}$$

Where γ and p are shape parameters and $d_a = w_I$, the weight of the interest point $\boldsymbol{x}_I$. According to Liu and Wang, the shape parameters γ and p should be 1.03 and 1.42 using the RPIM (Wang & Liu, 2001). But using the NNRPIM formulation, Dinis et al. found that the optimal values for the shape parameters are $\gamma \leq 0.0001$ and $p \cong 1$ (Dinis et al., 2007). It is, however, important to note that γ must not be 0 because it leads to ill-conditioned or singular moment matrices and p must not be equal to or any other integer value, because it will make the moment matrix singular(Jorge Belinha, 2014a).

In order to obtain the non-constant coefficients $a(\boldsymbol{x}_I)$ and $b(\boldsymbol{x}_I)$, $u^h(\boldsymbol{x}_I)$ is imposed to pass through all the nodal values n of the support-domain of $\boldsymbol{x}_I$, obtaining the following system of equations, expressed in matrix form:

$$\boldsymbol{R}\, \boldsymbol{a}(\boldsymbol{x_I}) + \boldsymbol{P}\, \boldsymbol{b}(\boldsymbol{x_I}) = \boldsymbol{u}_s \tag{3.26}$$

Where, u_s is the vector containing the nodal parameters of the field function for each node inside the support-domain of the RPI shape function defined as:

$$\boldsymbol{u_s^T} = \{u_1 \quad u_2 \quad \cdots \quad u_n\} \tag{3.27}$$

Focused on the MQ RBF, the radial moment is defined as:

$$\boldsymbol{R} = \begin{bmatrix} (d_{11}^2 + (\gamma d_c)^2)^p & (d_{12}^2 + (\gamma d_c)^2)^p & \cdots & (d_{1n}^2 + (\gamma d_c)^2)^p \\ (d_{21}^2 + (\gamma d_c)^2)^p & (d_{22}^2 + (\gamma d_c)^2)^p & \cdots & (d_{2n}^2 + (\gamma d_c)^2)^p \\ \vdots & \vdots & \ddots & \vdots \\ (d_{n1}^2 + (\gamma d_c)^2)^p & (d_{n2}^2 + (\gamma d_c)^2)^p & \cdots & (d_{nn}^2 + (\gamma d_c)^2)^p \end{bmatrix} \tag{3.28}$$

Moreover, the polynomial moment matrix is defined as:

$$\boldsymbol{P} = \begin{bmatrix} p_1(\boldsymbol{x}_1) & p_2(\boldsymbol{x}_1) & \cdots & p_m(\boldsymbol{x}_1) \\ p_1(\boldsymbol{x}_2) & p_2(\boldsymbol{x}_2) & \cdots & p_m(\boldsymbol{x}_2) \\ \vdots & \vdots & \ddots & \vdots \\ p_1(\boldsymbol{x}_n) & p_2(\boldsymbol{x}_n) & \cdots & p_m(\boldsymbol{x}_n) \end{bmatrix} \tag{3.29}$$

In order to obtain a unique solution, another set of equations has to be used (Golberg, Chen, & Bowman, 1999), as a consequence of a theorem of Duchon (1977). Consequently, the following supplementary m equations can be added to the initial equations system, and can be written in matrix form as:

$$\boldsymbol{P^T}\, \boldsymbol{a}(\boldsymbol{x_I}) = 0 \tag{3.30}$$

Combining Equation. (3.26) and Equation.(3.30), it is possible to obtain the following set of equations, written in matrix form:

$$\begin{bmatrix} \boldsymbol{R} & \boldsymbol{P} \\ \boldsymbol{P^T} & \boldsymbol{Z} \end{bmatrix} \begin{Bmatrix} \boldsymbol{a(x_I)} \\ \boldsymbol{b(x_I)} \end{Bmatrix} = \boldsymbol{M_T} \begin{Bmatrix} \boldsymbol{a(x_I)} \\ \boldsymbol{b(x_I)} \end{Bmatrix} = \begin{Bmatrix} \boldsymbol{u_s} \\ \boldsymbol{z} \end{Bmatrix} \tag{3.31}$$

Where $Z_{ij} = 0$ for $\{i, j\} = 1, 2, \dots, m$ and $z_i = 0$ for $i = 1, 2, \dots, m$. Through the Equation. (3.32) it is possible to obtain the non-constant coefficients $\boldsymbol{a}(\boldsymbol{x}_I)$ and $\boldsymbol{b}(\boldsymbol{x}_I)$:

$$\begin{Bmatrix} \boldsymbol{a(x_I)} \\ \boldsymbol{b(x_I)} \end{Bmatrix} = \boldsymbol{M_T^{-1}} \begin{Bmatrix} \boldsymbol{u_s} \\ \boldsymbol{z} \end{Bmatrix} \tag{3.32}$$

After substituting the solution from Equation. (3.32) in Equation. (3.19) it is possible to re-write Equation. (3.19) and obtain the following equation:

$$u^h(\boldsymbol{x_I}) = \{\boldsymbol{r(x_I)}^T \quad \boldsymbol{p(x_I)}^T\} \boldsymbol{M_T^{-1}} \begin{Bmatrix} \boldsymbol{u_s} \\ \boldsymbol{z} \end{Bmatrix} \tag{3.33}$$

Since the field variable value for an interest point $\boldsymbol{x}_I$ is interpolated using the shape function values obtained at the nodes inside the influence cell of the interest point, it is possible to identify the interpolation function vector $\varphi(\boldsymbol{x}_I)$, with size n, through the Equation. (3.33):

$$\boldsymbol{u^h(x_I)} = \{\boldsymbol{r(x_I)}^T \quad \boldsymbol{p(x_I)}^T\} \boldsymbol{M_T^{-1}} \begin{Bmatrix} \boldsymbol{u_s} \\ \boldsymbol{z} \end{Bmatrix} = \{\boldsymbol{\varphi(x_I)}^T \quad \boldsymbol{\psi(x_I)}^T\} \begin{Bmatrix} \boldsymbol{u_s} \\ \boldsymbol{z} \end{Bmatrix} \tag{3.34}$$

Where, $\boldsymbol{\psi(x_I)^T}$ is a by-product vector, that only exists if a polynomial basis is considered, otherwise not. Therefore, the interpolation function vector can be defined as:

$$\boldsymbol{\varphi(x_I)} = \{\boldsymbol{r(x_I)}^T \quad \boldsymbol{p(x_I)}^T\} \boldsymbol{M_T^{-1}} \tag{3.35}$$

The first order partial derivative of this function in respect to a generic variable ξ can be written as follows:

$$\frac{\partial \varphi(\boldsymbol{x_I})}{\partial \xi} = \left\{ \frac{\partial r(\boldsymbol{x_I})^T}{\partial \xi} \quad \frac{\partial p(\boldsymbol{x_I})^T}{\partial \xi} \right\} \boldsymbol{M_T^{-1}} \tag{3.36}$$

Being the MQ partial derivative:

$$\frac{\partial r_i(\boldsymbol{x_I})}{\partial \xi} = -2p(\xi_i - \xi_I)\left(d_{il}^2 + (\gamma d_a)\right)^{p-1} \tag{3.37}$$

Chapter 4

SOLID MECHANICS FUNDAMENTALS

4.1. 3D CLASSICAL DEFORMATION THEORY

This chapter presents the fundamentals for Solid Mechanics, specifically for three-dimensional solids. For a better understanding of the information presented below, it is important to remember that the numerical application used in this work pertains to the case of 3D-solids.

4.1.1. Continuum Formulation

Continuum mechanics are the foundation of nonlinear numerical analysis. The stresses that appear in solids and structures are due to loads or forces applied to them. Strains – deformations or relative displacements - are the consequence of stresses.

Solid Mechanics work, for a given solid and boundary conditions (external forces and displacement constraint) with the relationship between stress and strain and, consequently, with the relationship between strain and displacement. Depending on the material with which one works, the solid can show different behaviours and thus, different stress-strain curves. When the work is applied to elastic material, a deformation appears with the load and disappears entirely when the solid is unloading. Otherwise, the plastic material would maintain the residual deformation as well when the solid is entirely unloading.

The material properties of the solid can be isotropic or anisotropic.This depends on whether the properties vary with the direction or not. In short, an anisotropic material -when the load is applied in one direction - the deformation will not be the same as when the load is applied in another direction – as is the case for isotropic materials. This means that, for isotropic materials, only two independent material properties are needed, the Young's modulus and the Poisson's ratio.

4.1.2. Kinematics

Kinematics is the study of motion regardless of the forces responsible for that motion. The application of a load can lead to the movement of an object. The equations characterising this movement are called the equations of motion. They compute the displacement of an object by measuring how far it has moved from its initial location (Capaldi, 2012).

The motion can be mathematically described by a mapping function Φ between initial and current particle position:

$$\boldsymbol{x} = \Phi(\boldsymbol{X}, t) \tag{4.1}$$

If the deformation map Equation. (4.1) is a continuous function in time, providing the equation of motion for the body. The equation need not be continuous in time since the deformation map may be established between two configurations that are discontinuous in time.

Continuous mechanics can be used to describe the response of gaseous, fluid, and solid systems. Whereas the underlying physics governing the behaviour of these is the same, it is usually formulated descriptions of solid systems using the Lagrange description and using an Eulerian description for fluid systems. Within the Lagrange description, also known as the material description, the reference position and the time are independent variables.

4.1.3. Stress and Strain

Consider the 3D solid that it is shown in Figure 32, with volume Ω and boundary Γ. The surface, where the external forces $\bar{t}$ are applied, is called natural boundary Γ_t. On the essential boundary the displacements are constrained, Γ_u. The loads that can be applied on the solid are body forces, b and/or surface forces, $\bar{t}$.

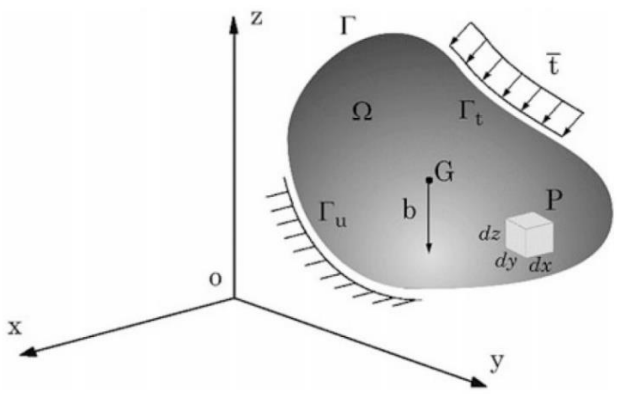

Figure 32 3D solid with body and surface forces applied (Belinha 2014)

If considering any point of the solid that it is represented by the infinitesimal cubic volume shown in Figure 33, it is possible to visualise the six distinct stress components at any point of the solid.

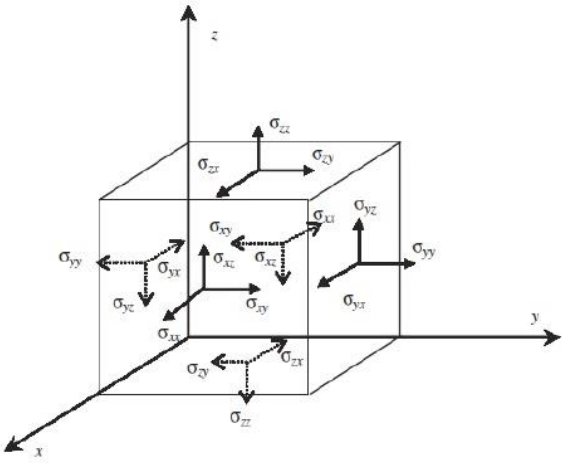

Figure 33 Infinitesimal cubic volume with the six-independent stress component (Patarata, 2017)

These six stress components are usually called the stress tensor and can be written, in the vector form as:

$$\boldsymbol{\sigma}^T = \{\sigma_{xx} \quad \sigma_{yy} \quad \sigma_{zz} \quad \tau_{xy} \quad \tau_{xz} \quad \tau_{yz}\} \tag{4.2}$$

At any point of the solid, there are also six strain components corresponding to the previous six stress components:

$$\boldsymbol{\varepsilon}^T = \{\varepsilon_{xx} \quad \varepsilon_{yy} \quad \varepsilon_{zz} \quad \gamma_{xy} \quad \gamma_{xz} \quad \gamma_{yz}\} \tag{4.3}$$

The displacement field is composed of the displacements in the x, y and z directions:

$$\boldsymbol{u} = \begin{Bmatrix} u(x,y,z) \\ v(x,y,z) \\ w(x,y,z) \end{Bmatrix} \tag{4.4}$$

The strain components are obtained from the derivatives of the displacement field in the way shown below:

$$\begin{gathered} \varepsilon_{xx} = \frac{\partial u}{\partial x} \qquad \varepsilon_{yy} = \frac{\partial v}{\partial y} \qquad \varepsilon_{zz} = \frac{\partial w}{\partial z} \\ \gamma_{xy} = \frac{\partial u}{\partial y} + \frac{\partial v}{\partial x} \qquad \gamma_{xz} = \frac{\partial u}{\partial z} + \frac{\partial w}{\partial x} \qquad \gamma_{yz} = \frac{\partial v}{\partial z} + \frac{\partial w}{\partial y} \end{gathered} \tag{4.5}$$

Also, the strain field can be represented amatrix form as a product between the matrix of partial differential operators $\boldsymbol{L}$ and the displacement field $\boldsymbol{u}$:

$$\boldsymbol{\varepsilon} = \boldsymbol{L}\boldsymbol{u} \tag{4.6}$$

where $\boldsymbol{L}$ is given by:

$$\boldsymbol{L} = \begin{bmatrix} \partial/\partial x & 0 & 0 & \partial/\partial y & \partial/\partial z & 0 \\ 0 & \partial/\partial y & 0 & \partial/\partial x & 0 & \partial/\partial z \\ 0 & 0 & \partial/\partial z & 0 & \partial/\partial x & \partial/\partial y \end{bmatrix}^T \tag{4.7}$$

4.1.4. Constitutive Equations

The constitute equation give the relations between strain and stress. The generalised Hooke's Law can define this relation:

$$\boldsymbol{\sigma} = \mathbf{c}\boldsymbol{\varepsilon} \tag{4.8}$$

Considering the definition of isotropic material, one can adequately define the material constants using only the material Young's Modulus, E, and the Poisson's ratio, v. Thus, the matrix of material constants, $\boldsymbol{c}$, for isotropic materials are defined per Equation. (4.9) :

$$\boldsymbol{c} = \frac{E}{(1+v)(1-2v)}\begin{bmatrix} 1-v & v & v & 0 & 0 & 0 \\ & 1-v & v & 0 & 0 & 0 \\ & & 1-v & 0 & 0 & 0 \\ & sym & & \frac{1-2v}{2} & 0 & 0 \\ & & & & \frac{1-2v}{2} & 0 \\ & & & & & \frac{1-2v}{2} \end{bmatrix} \tag{4.9}$$

In a fully anisotropic material, the matrix of materials constants, $\boldsymbol{c}$, has 21 independent material constants.

4.1.5. Static Equilibrium Equations

In order to obtain the static equilibrium equations through a force balance, it is necessary to consider all the directions. The static equilibrium equations for an infinitesimal solid volume are given by:

$$\frac{\partial \sigma_{xx}}{\partial x} + \frac{\partial \tau_{xy}}{\partial y} + \frac{\partial \tau_{xz}}{\partial z} + F_x = 0 \tag{4.10}$$

$$\frac{\partial \tau_{xy}}{\partial x} + \frac{\partial \sigma_{yy}}{\partial y} + \frac{\partial \tau_{yz}}{\partial z} + F_y = 0 \tag{4.11}$$

$$\frac{\partial \tau_{xz}}{\partial x} + \frac{\partial \sigma_{yz}}{\partial y} + \frac{\partial \sigma_{zz}}{\partial z} + F_z = 0 \tag{4.12}$$

The equilibrium Equations (4.10, 4.11, 4.12) can also be written in the matrix form, using the matrix $\boldsymbol{L}$ as:

$$\boldsymbol{L}^T\boldsymbol{\sigma} + \boldsymbol{F}_b = 0 \tag{4.13}$$

Considering $\boldsymbol{F}_b$ the vector of external body forces in the directions x, y and z.

Applying the displacement, this means using the Equations (4.6, 4.8), it is possible to write the static equilibrium Equation (4.13) as:

$$\boldsymbol{L}^T\boldsymbol{c}\boldsymbol{L}\boldsymbol{u} + \boldsymbol{F}_b = 0 \tag{4.14}$$

4.1.6. Boundary Conditions

Regarding boundary conditions, there are two types: displacement (essential) and force (natural) boundary conditions (G. R. Liu & Quek, 2003). The displacement boundary conditions can be directly written as:

$$u = \bar{u} \quad and/or \quad v = \bar{v} \quad and/or \quad w = \bar{w} \tag{4.15}$$

Frequently, the displacement is used to describe the support or constraints on the solid and, usually, the prescribed displacement values are zero.

The force boundary conditions are often written as:

$$\boldsymbol{n}\boldsymbol{\sigma} = \bar{\boldsymbol{t}} \tag{4.16}$$

Where **n** is given by:

$$\boldsymbol{n} = \begin{bmatrix} n_x & 0 & 0 & 0 & n_z & n_y \\ 0 & n_y & 0 & n_z & 0 & n_x \\ 0 & 0 & n_z & n_y & n_x & 0 \end{bmatrix} \tag{4.17}$$

For which $n_i (i = x,\ y,\ z)$ are cosines of the outward normal on the boundary.

4.2. STRONG AND WEAK FORM FORMULATION

The static equilibrium equations, which constitute the partial differential equations system, are the strong form of a static solid mechanics problem (Zienkiewicz & Taylor, 2000).

The strong form formulation can be efficiently applied to problems with simple geometries and boundary conditions. The ideal situation would be obtaining the exact solution from strong form system equations. However, this is usually very difficult to obtain as it causes considerable engineering practical problems: it requires strong continuity on the field variables and the functions must be differentiable up to the order of the strong form partial differential equations (Zienkiewicz & Taylor, 2000).

Nevertheless, the formulations based on weak forms are more often used in engineering problems because they can generate a set of discretised systems of algebraic equations that allow for obtaining an approximate solution for problems with higher complexity (G. R. Liu & Quek, 2003).

4.2.1. Weak Form of Galerkin

The Galerkin weak form is a variational principle based on Hamilton's energy principle. This principle was chosen because it is simple and can be used for dynamics problems. Hamilton's principle allows one to assume any set of displacement, as long as it satisfies three possible conditions. These conditions are the compatibility equations, the essential boundary conditions (kinematical and displacement) and the initial and final time conditions. When these conditions are met, the configuration thats minimises the Lagrangian function L correspond to the real solution (G. R. Liu & Quek, 2003).

The Lagrangian functional consist of:

$$L = T - U + W_f \tag{4.18}$$

where T represents the kinetic energy, U the strain energy and W_f the work produced by external forces.

The kinetic energy is defined by:

$$T = \frac{1}{2}\int_{\Omega} \rho \dot{\boldsymbol{u}}^T \dot{\boldsymbol{u}}\, d\Omega \tag{4.19}$$

where ρ is the density of the solid mass and $\dot{\boldsymbol{u}}$ is the displacement's first derivative in order to time, velocity.

The strain energy, for an elastic material, is expressed as:

$$U = \frac{1}{2}\int_{\Omega} \boldsymbol{\varepsilon}^T \boldsymbol{\sigma}\, d\Omega \tag{4.20}$$

being $\boldsymbol{\varepsilon}$ the strain vector and $\boldsymbol{\sigma}$ the stress vector.

Finally, the work produced by the external forces can be expressed as:

$$W_f = \int_{\Omega} \boldsymbol{u}^T \boldsymbol{b}\, d\Omega + \int_{\Gamma_t} \boldsymbol{u}^T \bar{\boldsymbol{t}}\, d\Gamma \tag{4.21}$$

where $\boldsymbol{u}$ is the displacement, $\boldsymbol{b}$ the body forces and Γ_t is the traction boundary where the external forces $\bar{\boldsymbol{t}}$ are applied (Figure 32).

After applying some mathematical manipulation to Equation. (4.18), using the constitutive equation $\boldsymbol{\sigma} = \boldsymbol{c\varepsilon}$ and the symmetric property of the material matrix, $\boldsymbol{c^T} = \boldsymbol{c}$, it is possible to conclude with the following expression, known as the 'Galerkin weak form', which can also be viewed as the principle of virtual work:

$$-\rho \int_{\Omega} (\delta \boldsymbol{u}^T \ddot{\boldsymbol{u}}) d\Omega - \int_{\Omega} (\delta \boldsymbol{\varepsilon}^T \boldsymbol{\sigma}) d\Omega + \int_{\Omega} (\delta \boldsymbol{u}^T \boldsymbol{b}) d\Omega + \int_{\Gamma_t} \boldsymbol{u}^T \bar{\boldsymbol{t}}\, d\Gamma = 0 \tag{4.22}$$

This principle of virtual work announces that, if there is equilibrium in a solid body, the virtual work produced by the inner body stresses and external forces applied to the body should vanish when the body experiments a virtual displacement.

Taking that into account, the stress-strain relation, $\boldsymbol{\sigma} = \boldsymbol{c\varepsilon}$, and the strain-displacement relation, $\boldsymbol{\varepsilon} = \boldsymbol{Lu}$, the Equation. (4.22) can be written as:

$$\int_{\Omega} \delta(\boldsymbol{Lu})^T c(\boldsymbol{Lu}) d\Omega - \int_{\Omega} \boldsymbol{u}^T \boldsymbol{b}\, d\Omega - \int_{\Gamma_t} \boldsymbol{u}^T \bar{\boldsymbol{t}}\, d\Gamma + \int_{\Omega} \rho(\delta \boldsymbol{u}^T \ddot{\boldsymbol{u}}) d\Omega = 0 \tag{4.23}$$

Equation (4.23) is the generic Galerkin weak form, written in terms of displacement.

4.2.2. Discrete System of Equations

Based on meshless methods, the discrete system of equations is obtained through the principle of virtual work using, as trial functions, the meshless shape functions.

The trial function $\boldsymbol{u}(\boldsymbol{x_i})$ for the meshless method can be expressed as:

$$\boldsymbol{u}(\boldsymbol{x_i}) = \sum_{\boldsymbol{i=1}}^{\boldsymbol{n}} \varphi_i(\boldsymbol{x_I}) \boldsymbol{u_i} \tag{4.24}$$

where, $\boldsymbol{\varphi_i}(\boldsymbol{x_I})$ is the interpolation function, or meshless method approximation function and $\boldsymbol{u_i}$ are the nodal displacements for each n node that belongs to the influence-domain of the interest point $\boldsymbol{x_I}$.

Considering Equaiton. (4.24), the virtual displacement can be written as:

$$\delta \boldsymbol{u}(\boldsymbol{x_i}) = \sum_{\boldsymbol{i=1}}^{\boldsymbol{n}} \varphi_i(\boldsymbol{x_I}) \delta \boldsymbol{u_i} \tag{4.25}$$

Substituting the Equations (4.24) and (4.25) on the "Galerkin weak form" equation for static problems comes:

$$-\int_{\Omega}\left(\sum_{i=1}^{n}\varphi_i(\boldsymbol{x_I})\delta\boldsymbol{u_i}\right)^T\boldsymbol{L}^T\boldsymbol{c}\boldsymbol{L}\left(\sum_{i=1}^{n}\varphi_i(\boldsymbol{x_I})\boldsymbol{u_i}\right)d\Omega+\int_{\Omega}\left(\sum_{i=1}^{n}\varphi_i(\boldsymbol{x_I})\delta\boldsymbol{u_i}\right)^T\boldsymbol{b}\,d\Omega+$$
$$+\int_{\Gamma^t}\left(\sum_{i=1}^{n}\varphi_i(\boldsymbol{x_I})\delta\boldsymbol{u_i}\right)^T\bar{\boldsymbol{t}}\,d\Gamma=0 \tag{4.26}$$

To eliminate the summative operator, it is possible to replace them with a matrix equation.

Considering 3D problems, it is possible to define the matrix of approximation/interpolation functions for the interested point $\boldsymbol{x_I}$ as:

$$\varphi_i(\boldsymbol{x_I})=\begin{bmatrix}\varphi_1(\boldsymbol{x_I}) & 0 & 0 & \varphi_2(\boldsymbol{x_I}) & 0 & 0 & \cdots\varphi_n(\boldsymbol{x_I}) & 0 & 0\\ 0 & \varphi_1(\boldsymbol{x_I}) & 0 & 0 & \varphi_2(\boldsymbol{x_I}) & 0 & \cdots & 0 & \varphi_n(\boldsymbol{x_I}) & 0\\ 0 & 0 & \varphi_1(\boldsymbol{x_I}) & 0 & 0 & \varphi_2(\boldsymbol{x_I})\cdots & 0 & 0 & \varphi_n(\boldsymbol{x_I})\end{bmatrix} \tag{4.27}$$

Equation (4.26) can also be written in a matrix form as:

$$-\delta\boldsymbol{u_I}^T\int_{\Omega}[(\boldsymbol{\varphi}(\boldsymbol{x_I}))^T\boldsymbol{L}^T]\boldsymbol{c}[\boldsymbol{L}\,\boldsymbol{\varphi}(\boldsymbol{x_I})]d\Omega\boldsymbol{u_I}+\int_{\Omega}(\boldsymbol{\varphi}(\boldsymbol{x_I}))^T\boldsymbol{b}\,d\Omega+$$
$$+\delta\boldsymbol{u_I}^T\int_{\Gamma^t}(\boldsymbol{\varphi}(\boldsymbol{x_I}))^T\bar{\boldsymbol{t}}\,d\Gamma=0 \tag{4.28}$$

where $\boldsymbol{u_I}$ is the nodal displacement vector of all the n nodes inside the influence domain. This vector can be written as:

$$\boldsymbol{u_I}=\{u_1,v_1,w_1,u_2,v_2,w_{2,\dots},u_n,v_n,w_n\}^T \tag{4.29}$$

Then, the matrix of partial differential operator $\boldsymbol{L}$, Equation. (4.7), should be recalled. It is possible to define the deformability matrix $\boldsymbol{B}(\boldsymbol{x_I})$ for the interest point $\boldsymbol{x_I}$ as the matrix multiplication between $\boldsymbol{L}$ and $\boldsymbol{\varphi}(\boldsymbol{x_I})$, being:

$$\boldsymbol{B_i}(\boldsymbol{x_I})=\boldsymbol{L}\boldsymbol{\varphi}_i(\boldsymbol{x_I})=\begin{bmatrix}\dfrac{\partial\varphi_{\mathrm{i}}(\boldsymbol{x_I})}{\partial x} & 0 & 0 & \dfrac{\partial\varphi_{\mathrm{i}}(\boldsymbol{x_I})}{\partial y}\dfrac{\partial\varphi_{\mathrm{i}}(\boldsymbol{x_I})}{\partial z} & 0\\ 0 & \dfrac{\partial\varphi_{\mathrm{i}}(\boldsymbol{x_I})}{\partial y} & 0 & \dfrac{\partial\varphi_{\mathrm{i}}(\boldsymbol{x_I})}{\partial x} & 0 & \dfrac{\partial\varphi_{\mathrm{i}}(\boldsymbol{x_I})}{\partial z}\\ 0 & 0 & \dfrac{\partial\varphi_{\mathrm{i}}(\boldsymbol{x_I})}{\partial z} & 0 & \dfrac{\partial\varphi_{\mathrm{i}}(\boldsymbol{x_I})}{\partial x}\dfrac{\partial\varphi_{\mathrm{i}}(\boldsymbol{x_I})}{\partial y}\end{bmatrix} \tag{4.30}$$

Matrix $\boldsymbol{B}(\boldsymbol{x_I})$ is composed by all of the n $\boldsymbol{B_i}(\boldsymbol{x_I})$ matrixes, one for each node in the influence-domain.

Finally, introducing the deformation matrix in Equation. (4.28), the expression takes the form:

$$-\delta\boldsymbol{u_I}^T\int_{\Omega}(\boldsymbol{B_i}(\boldsymbol{x_I}))^T\boldsymbol{c}\boldsymbol{B_i}(\boldsymbol{x_I})\,d\Omega\boldsymbol{u_I}+\int_{\Omega}(\boldsymbol{\varphi}(\boldsymbol{x_I}))^T\boldsymbol{b}\,d\Omega+$$
$$+\delta\boldsymbol{u_I}^T\int_{\Gamma^t}(\boldsymbol{\varphi}(\boldsymbol{x_I}))^T\bar{\boldsymbol{t}}\,d\Gamma=0 \tag{4.31}$$

That leads to the local static equilibrium equation for the influence-domain corresponding to the interest point $\boldsymbol{x_I}$:

$$\int_{\Omega} (\boldsymbol{B_i}(\boldsymbol{x_I}))^T \boldsymbol{c} \boldsymbol{B_i}(\boldsymbol{x_I})\, d\Omega \boldsymbol{u_I} - \int_{\Omega} (\boldsymbol{\varphi}(\boldsymbol{x_I}))^T \boldsymbol{b}\, d\Omega +$$

$$-\delta \boldsymbol{u_I}^T \int_{\Gamma^t} (\boldsymbol{\varphi}(\boldsymbol{x_I}))^T \bar{\boldsymbol{t}}\, d\Gamma = 0 \tag{4.32}$$

where the first integral corresponds to the local stiffness matrix, $\boldsymbol{K}_I$ and the other two integrals can be grouped constituting the local force vector $\boldsymbol{F}_I$.

Therefore, considering nodal connectivity, the previous local matrixes should be assembled, leading to the discrete global system of equations:

$$\boldsymbol{K}\,\boldsymbol{u} = \boldsymbol{F} \tag{4.33}$$

where $\boldsymbol{K}$ is the global stiffness matrix, $\boldsymbol{u}$ is the global nodal displacement vector and $\boldsymbol{F}$ is the global force vector.

4.2.3.Stiffness Matrix

Regarding the material properties, whose information is kept in the stiffness matrix, means that each element has its local stiffness matrix that is grouped, in the end, in a global stiffness matrix which is the sum of all the local stiffness matrices. To calculate the local stiffness matrix of one element, the first step is to create its deformation matrix [B] for each Gauss point:

$$\underbrace{\mathrm{B_I}}_{[3\times 2n]} = \begin{bmatrix} \frac{\partial N_1}{\partial x} & 0 & \cdots & \frac{\partial N_n}{\partial x} & 0 \\ 0 & \frac{\partial N_1}{\partial y} & \cdots & 0 & \frac{\partial N_n}{\partial y} \\ \frac{\partial N_1}{\partial y} & \frac{\partial N_1}{\partial x} & \cdots & \frac{\partial N_n}{\partial y} & \frac{\partial N_n}{\partial x} \end{bmatrix} \tag{4.34}$$

Having built the deformation matrix for a Gauss point, is possible to calculate the stiffness matrix for that Gauss point.This requires the constitutive matrix, and its form is going to depend on the theory that is used.

Therefore, the local stiffness matrix for the integration point I is given by:

$$\underbrace{[K_I]}_{[2n\times 2n]} = W_I \cdot [B_I]^T \cdot [c] \cdot [B_I] \tag{4.35}$$

This expression will give the stiffness matrix for the nodes of the elements that correspond to that integration point. Finally, the global stiffness matrix is constructed by adding the stiffness matrices of all the integration points:

$$\underbrace{K_{global}}_{[2N\times 2N]} = \sum_{I=1}^{Q} [K_I] \tag{4.36}$$

where Q is the total number of integration points of the domain and N is the total number of nodes of the domain.

4.2.4. Natural Boundary Conditions

In order to apply a force along a boundary line Γ, the nodes on that boundary have to be identified, calling this set of nodes in the boundary X_Γ. Then, a new set of integration points

along the boundary has to be created Q_Γ, because the integration points discretising the domain cannot be used to integrate a function along the boundary line.

The process to obtain the shape function values at the integration points is the same as described in 3.1.2, but in this case, the elements of the boundary line are 1D, not 2D.

The shape functions are then used to create the matrix $[H]$ for the integration point I:

$$\underbrace{[\mathrm{H_I}]}_{[2\times 2n]} = \left[\begin{array}{cc:c:cc} \varphi_1 & 0 & \cdots & \varphi_n & 0 \\ 0 & \varphi_1 & \cdots & 0 & \varphi_n \end{array}\right] \tag{4.37}$$

The following Equation (4.38) shows how the boundary external force vector can be calculated:

$$f_e = \sum_{I=1}^{Q} w_I^\Gamma \, H_I^T \, \bar{t_c}(q_I) \tag{4.38}$$

where $\bar{t_c}(q_I)$ is a vector dependent on the position of the integration point, composed by the function that defines the forces applied to the boundary in the all the Cartesian directions.

4.2.5. Essential Boundary Conditions

Of the many different ways to impose essential boundary conditions, one of the most common methods is the "penalty method" or the "direct imposition method".

In this work, the definition of boundary conditions was carried out using the direct imposition method according to the detailed description provided in (Jorge Belinha, 2014).

Using the direct imposition method, the essential boundary conditions can be implemented directly into the system of equations $\boldsymbol{Ku} = \boldsymbol{f}$ by modifying both the global stiffness matrix and the global force vector.

The group of nodes that are constrained in the boundary conditions are called X_Γ. Considering a general case where each field node x has m degrees of freedom, the field node $x_I \in X_\Gamma$ has a displacement constraint $\bar{u}$ on the Jth degree of freedom. As in the natural boundary conditions, the first step here is to identify the nodes in the boundary. Then the essential boundary condition can be imposed by these modifications to the stiffness matrix and the force vector:

$$K_{(m\cdot i-(m-n)),(m\cdot j-(m-k))} = \begin{cases} 0 & if\ i = I\ \wedge n = J \\ 1 & if\ i = j = I\ \wedge n = k = J \\ K_{(m\cdot i-(m-n))(m\cdot j-(m-k))} & if\ i \neq I \vee (i = I\ \wedge n \neq J) \end{cases} \tag{4.39}$$

$$f_{(m\cdot i-(m-n))} = \begin{cases} \bar{u} & if\ i = I\ \wedge n = J \\ f_{(m\cdot i-(m-n))} & if\ i \neq I \vee (i = I\ \wedge n \neq J) \end{cases} \tag{4.40}$$

where $\{i, j\} = \{1,2,\dots,N\}$ and $\{n, k\} = \{1,2,\dots,m\}$.

4.2.6. Strain, Stress and Displacement

The displacement vector, $\boldsymbol{u}$, is calculated using Equation. (4.41):

$$\boldsymbol{u} = \boldsymbol{K}^{-1}\,\boldsymbol{f} \tag{4.41}$$

where $\boldsymbol{K}$ is the stiffness matrix with the imposed constraints and $\boldsymbol{f}$ the force vector with the imposed constraints and the applied external forces.

Then, the strain is calculated for each integration point using Equation. (4.42):

$$\varepsilon_I = [B_I]\boldsymbol{u}_e \tag{4.42}$$

where $[B_I]$ is the matrix from Equation. (4.34) and $\boldsymbol{u}_e$ is the displacement vector of the element in which that integration point is located. The relationship between the stress and the strains at a Gauss point is:

$$\sigma_I = [D]\varepsilon_I \tag{4.43}$$

4.2.7.Continuum procedure

The implementation of the NNRPIM is similar to the FEM method. To build the stiffness matrix in NNRPIM, Section 4.2.3 can be followed by the shape functions and its derivatives being substituted by the shape functions and derivatives presented in Section 3.2.6, while and taking into account that the parameter $\mathrm{B_I}$ that would be built based on the number of nodes inside the element is now based on the number of nodes inside the influence cell of the interest point.

The natural boundary conditions can also be imposed following Section 4.2.4 but using the shape functions from Section 3.2.6 as explained before.

Because the RPI shape functions have the Kronecker delta property, the essential boundary conditions can also be imposed accroding to Section 4.2.5.

Finally, stresses, strains and displacements can be calculated following the work presented in Section 4.2.6.

4.3. YIELD CRITERION FOR SOLID AND CELLULAR MATERIALS

A yield criterion, usually expressed as yield surface, is a hypothesis concerning the limit of elasticity under any combination of stresses. The yield criterion depends on: stress state, loading history, hardening parameter and the yield tension of the material.

The yield criterion can be generally expressed as:

$$F(\boldsymbol{\sigma}, \boldsymbol{\varepsilon}_P, k) = f(\boldsymbol{\sigma}, \boldsymbol{\varepsilon}_P, k) - \sigma_Y(k) = 0 \tag{4.44}$$

where $f(\boldsymbol{\sigma}, \boldsymbol{\varepsilon}_P, k)$ is the yield function.

Considering that the yield tension is constant and the material isotropic and also that the yield stress is independent of the hardening parameter, it is possible to simplify Equation (4.44):

$$F(\boldsymbol{\sigma}) = f(\boldsymbol{\sigma}) - \sigma_Y = 0 \tag{4.45}$$

Many yield criteria are expressed regarding the invariants of the stress tensor, invariants of the deviatoric tensor or regarding mean stress and equivalent stress.

The stress tensor:

$$[\sigma_{ij}] = \begin{bmatrix} \sigma_{11} & \sigma_{12} & \sigma_{13} \\ \sigma_{21} & \sigma_{22} & \sigma_{23} \\ \sigma_{31} & \sigma_{32} & \sigma_{33} \end{bmatrix} \tag{4.46}$$

is a symmetric tensor ($\sigma_{ij} = \sigma_{ji}$).

$$
\begin{aligned}
I_1 &= \sigma_{xx} + \sigma_{yy} + \sigma_{zz} \\
I_2 &= -{\sigma_{xy}}^2 - {\sigma_{xz}}^2 - {\sigma_{yz}}^2 + \sigma_{xx}\sigma_{yy} + \sigma_{xx}\sigma_{zz} + \sigma_{yy}\sigma_{zz} \\
I_3 &= \sigma_{xx}\sigma_{yy}\sigma_{zz} + 2\sigma_{xy}\sigma_{yz}\sigma_{zx} - \sigma_{xx}{\sigma_{yz}}^2 - \sigma_{yy}{\sigma_{xz}}^2 - \sigma_{zz}{\sigma_{xy}}^2
\end{aligned}
\tag{4.47}
$$

where I_1, I_2 and $I_3$are the invariants of the stress tensor. This allows to obtain the stress tension by calculating the roots σ of the characteristic equation:

$$
\sigma^3 - I_1\sigma^2 + I_2\sigma - I_3 = 0 \tag{4.48}
$$

Solving the characteristic equation, it becomes possible to obtain the values of the principal stresses σ_1, σ_2 and σ_3. The meaning of the principal stresses indicates the stress state that is studied. In the case of $\sigma_1 \neq 0$ and $\sigma_2 = \sigma_3 = 0$, the stress state is uniaxial. If $\sigma_1 \neq \sigma_2 \neq 0$ and $\sigma_3 = 0$ the stress state is in plane and if $\sigma_{1the} \neq \sigma_2 \neq \sigma_3 \neq 0$, the stress state is tri-dimensional. Also, if the $\sigma_1 = \sigma_2 = \sigma_3 \neq 0$ the stress state is hydrostatic, and the stress state is cylindrical if $\sigma_1 = \sigma_2 \neq 0 \neq \sigma_3$ or if $\sigma_1 = \sigma_3 \neq 0 \neq \sigma_2$ and finally if $\sigma_2 = \sigma_3 \neq 0 \neq \sigma_1$.

The invariants of the principal stress are:

$$
\begin{aligned}
I_1 &= \sigma_1 + \sigma_2 + \sigma_3 \\
I_2 &= \sigma_1\sigma_2 + \sigma_2\sigma_3 + \sigma_3\sigma_1 \\
I_3 &= \sigma_1\sigma_2\sigma_3
\end{aligned}
\tag{4.49}
$$

Thus, the yield function can be written as $f(\sigma_{i,}) = f(\sigma_{1,}\sigma_{2,}\sigma_3) = 0$. Also, the yield function can be written in function of the invariant $f(\sigma_{i,}) = f(I_1, J_2, J_3) = 0$.

It has been observed, experimentally, that in the plastic flow of metals the hydrostatic tension has minimum influence. Therefore, it is possible to consider the yield function independent of I_1 (Owen & Hinton, 1980).

The mean stress or hydrostatic pressure is usually defined as:

$$
\sigma_m = \frac{I_1}{3} = \frac{(\sigma_{xx} + \sigma_{yy} + \sigma_{zz})}{3} \tag{4.50}
$$

Moreover, knowing that the deviatoric stress state is defined as $S_{ij} = \sigma_{ij} - \sigma_m$, it is possible to calculate de invariant of the deviatoric tensor. Consequently, the yield function is now independent of I_1 and that means no volumetric changes. So finally, the yield function ix expressed as:

$$
f(\sigma) = f(J_2, J_3) = 1 \tag{4.51}
$$

where J_2 and J_3 are the invariants of the deviatoric stress tensor $\boldsymbol{S_{ij}}$ and 1 is a normalising factor that depends on the criteria.

Analysing Equation. (4.51) it is possible to state that:

If $f < 1$, the material shows linear elastic behaviour.
If $f = 1$, the material is between the elastic and the plastic behaviours.
If $f > 1$, the material is already showing plastic behaviour.

4.3.1. Yielding Criteria for Continuum Solid

Strain energy density depends on I_1 and J_2, leading to the development of a number of failure or yield criteria based on stress invariants. Bridgman (1947) showed, that, for metals, yielding is independent of the hydrostatic pressure. Therefore, a number of criteria written regarding the stress invariants are independent of I_1.

This section, presents two criteria for isotropic materials, von Mises and Tresca (Abrate, 2008).

von-Mises yield criteria

The von Mises yield criterion (also known as the Maximum Distortion Energy Theory of Failure) announce that yielding of a ductile material begins when the second invariant deviatoric J_2 reaches a critical value C_2. The second deviatoric invariant in terms of the principal stresses is:

$$J_2 = \frac{1}{6}\{(\sigma_1 - \sigma_2)^2 + (\sigma_2 - \sigma_3)^2 + (\sigma_3 - \sigma_1)^2\} = C_2 \tag{4.52}$$

Through a uniaxial tensile test, it was possible to obtain the critical value. This value is $C_2 = \frac{1}{6}2\sigma_{ced}^2$. Once this value is obtained, the equivalent stress or von Mises is defined as:

$$\sigma_{ced} = \frac{1}{\sqrt{2}}\sqrt{(\sigma_1 - \sigma_2)^2 + (\sigma_2 - \sigma_3)^2 + (\sigma_3 - \sigma_1)^2} \tag{4.53}$$

and the octahedral shear stress is defined as:

$$\tau_{oct} = \frac{1}{3}\sqrt{(\sigma_1 - \sigma_2)^2 + (\sigma_2 - \sigma_3)^2 + (\sigma_3 - \sigma_1)^2} \tag{4.54}$$

Tresca yield criteria

The Tresca criteria ennunciate that the yielding of material begins at the point of the solid where the maximum shear stress is located. At this point, the material reaches the critical value C_4:

$$max|\tau_r| = C_4 \tag{4.55}$$

knowing that the maximum value of the shear stress is given by:

$$max|\tau_r| = \left|\frac{\max(\sigma_1, \sigma_2, \sigma_3) - \min(\sigma_1, \sigma_2, \sigma_3)}{2}\right| \tag{4.56}$$

Through a uniaxial tensile test, it was possible to obtain the critical value. This value is $C_4 = \frac{\sigma_{ced}}{2}$. Once this value is obtained, the expression of the Tresca's criterion that is as follows:

$$\sigma_{ced} = |\max(\sigma_1, \sigma_2, \sigma_3) - \min(\sigma_1, \sigma_2, \sigma_3)| \tag{4.57}$$

Hosford generalised yield criteria

Additionally, W.F.Hosford (1972), proposed a generalised criterion with the form:

$$\left[\frac{|\sigma_1 - \sigma_2|^n + |\sigma_2 - \sigma_3|^n + |\sigma_3 - \sigma_1|^n}{2}\right]^{\frac{1}{n}} = \sigma_{ced} \tag{4.58}$$

where the exponent n need not be an integer. This criterion reduces to von Mises' criterion when $n = 2$ and to Tresca's criterion when $n = 1$. This expression serves as a basis for a number of yield criteria used to model the behaviour of anisotropic metals.

4.3.2. Yielding Criteria for Cellular Solids

Yielding or failure of isotropic foams depends on the hydrostatic stress, a feature that these materials share with many polymers, concrete and soils. Growing demand to use them in primary load bearing members and taking into account the objective to exploit the full potential of this lightweight material under complex loading situation requires an advanced understanding and accurate modelling of their yield behaviour under multiaxial stress states. A few models reflect and capture both the pressure-dependence of these highly porous materials and their inherent anisotropy associated with fabrication techniques.

Gibson, L. J., Ashby, M. F. and Triantafillou (1989) developed equations (GAZT model) that attempt to predict the yield surface of low-density isotropic foams with relative densities of approximately 0.1. This model fundamentally relies on the fact that the average bending moment in cell walls is proportional to the product of macroscopic deviatoric stress and the cube of average cell size while the axial stress in struts is proportional to the mean stress normalised by the relative density.

Furthermore, the GAZT model was extended to anisotropic foams defining additional brittle facture caps to trim the yield surface in the tension-tension quadrant. Zhang et al. (1997) implemented uniaxial, hydrostatic compression and shear experiments on polyurethane and polypropylene foams with 5% relative density and proposed a quadratic yield surface in the effective stress-mean stress space by using three material parameters. Miller (2000) performed an extension of the Drucker & Prager (1952) yield criterion, to account for varying responses in hydrostatic compression and tension, adding a quadratic pressure term to include the compressible plastic deformation. Deshpande & Fleck (2000) experimentally investigated the multi-axial yield behaviour of closed and open-cell aluminium foams. This study was done under mostly compressive stress states allowing to conclude that the hydrostatic yield strength is about 20% less than that of uniaxial yield strength. These results were the origin of the yield criterion (DF model). Deshpande & Fleck (2001), also investigated multi-axial yield behaviour of two different densities of PVC foams and proposed the DF limited yield criterion by a maximum compressive principal stress criterion. These studies report that the uniaxial tensile strengths of these PVC foams were comparable with the hydrostatic tensile strength and also that the deformation under tensile loading is governed by cell wall bending while under compressive loading this is achieved by elastic buckling of the cell walls.

Raghava, Caddell, & Yeh (1973) proposed an anisotropic yield criterion for pressure-dependent polymeric solids based on modifications to Hill (1950). Hill proposed a criterion capable of accounting for anisotropic behaviour. It is important to remark that this model is inadequate for modelling foam because the effects of the hydrostatic pressure are not included, though they are significant in tension and compression.

Xue & Hutchinson (2006) proposed a constitutive model that accounts for multi-axial stress states in orthotropic compressible materials. This model is mostly an extension of Hill's incompressible plasticity model for orthotropic materials to compressible foams cores. The model successfully predicts a yield surface under combinations of compression, shear and in-plane stretch, assuming uniform hardening. Tagarielli, Deshpande, Fleck, & Chen (2005) proposed a transversely isotropic yield criterion that is a modification to the anisotropic yield model of Lubliner & Moran (1992) and similar to that of Xue & Hutchinson (2006), where the coefficient of various quadratic terms are modified to reflect the transversely isotropic yield behaviour.

In the literature, it is possible to find similar approaches for constructing yield surfaces for anisotropic cellular solids. It is possible to extend the isotropic yield model by normalizing each stress measure in the yield function with the corresponding uniaxial yield strength (Gioux, McCormack, & Gibson, 2000) and extending the quadratic yield criterion of Hill (1950) for orthotropic incompressible solids to include compressibility (Deshpande & Fleck, 2001). This yield function use tends to overestimate experimental yield data of cellular material, and most of the model's constants have to be determined experimentally, which, in some cases, is not readily available.

Some of the yield criteria that were explained previously are summarised and shown in Table 9.

Table 9 Yield criteria proposed in the literature to define the yield surface of solid foams (Shafiq, Ayyagari, Ehaab, & Vural, 2015).

Model	Yield criterion
GAZT model (1989)	$\pm\frac{\sigma_e}{\sigma_{pl}^*}+0.81\left(\frac{\rho^*}{\rho_s}\right)\left(\frac{\sigma_m}{\sigma_{pl}^*}\right)^2=1, \qquad \sigma_{pl}^*=C_1\left(\frac{\rho^*}{\rho_s}\right)^{3/2}\sigma_{ys}$ $\sigma_e = Equivalent\ stress$ $\sigma_{pl}^* = Yield\ strength$ $\sigma_m = Hydrostatic\ stress$ $\sigma_{ys} = Yiels\ stress$
DF (2000)	$\hat{\sigma}^2=\frac{1}{[1+(\alpha/3)^2]}[\sigma_e^2+\alpha^2\sigma_m^2]-{\sigma_{pl}^*}^2, \qquad \frac{Y_{hyd}}{Y_{uni}}=\frac{\sqrt{1+(\alpha/3)^2}}{\alpha}$ $\sigma_e = von\ Mise's\ effective\ stress$ $\sigma_{pl}^* = Yield\ strength$ $\sigma_m = Mean\ stress$ $\alpha = Parameter\ that\ defines\ the\ shape\ of\ the\ yield\ surface$
Hill (1950)	$\mathrm{H}(\sigma_{11}-\sigma_{22})^2+F(\sigma_{22}-\sigma_{33})^2+G(\sigma_{33}-\sigma_{11})^2+2N\sigma_{12}^2+2L\sigma_{23}^2+2M\sigma_{31}^2=1$ $where, \qquad F=\frac{1}{2}\left\{\frac{1}{\sigma_{2T}^2}+\frac{1}{\sigma_{3T}^2}-\frac{1}{\sigma_{1T}^2}\right\}, \qquad H=\frac{1}{2}\left\{\frac{1}{\sigma_{1T}^2}+\frac{1}{\sigma_{2T}^2}-\frac{1}{\sigma_{3T}^2}\right\},$ $G=\frac{1}{2}\left\{\frac{1}{\sigma_{3T}^2}+\frac{1}{\sigma_{1T}^2}-\frac{1}{\sigma_{2T}^2}\right\}, \qquad L=\frac{1}{2(\tau_{23}^S)^2}, \qquad M=\frac{1}{2(\tau_{31}^S)^2},$

$$N = \frac{1}{2(\tau_{12}^S)^2}$$

$\sigma_{ij} = Components\ of\ the\ strees\ tensor$
$\sigma_{1T}, \sigma_{2T}, \sigma_{3T} = Yield\ strengths\ in\ the\ pricipal\ directions\ of\ anisotropy$
$\tau_{12}^S, \tau_{23}^S, \tau_{31}^S = Yield\ stresses\ with\ respect\ to\ the\ axes\ of\ anisotropy$

$$\mathrm{H}(\sigma_{11} - \sigma_{22})^2 + F(\sigma_{22} - \sigma_{33})^2 + G(\sigma_{33} - \sigma_{11})^2 + 2N_{\tau_{12}^2} + 2L_{\tau_{23}^2} + 2M_{\tau_{31}^2}$$

$$+K_1\sigma_{11} + K_2\sigma_{22} + K_3\sigma_{33} = 1$$

$$where, \quad F = \frac{1}{2}\left\{\frac{1}{\sigma_{2T}^2} + \frac{1}{\sigma_{3T}^2} - \frac{1}{\sigma_{1T}^2}\right\}, \quad H = \frac{1}{2}\left\{\frac{1}{\sigma_{1T}^2} + \frac{1}{\sigma_{2T}^2} - \frac{1}{\sigma_{3T}^2}\right\},$$

$$G = \frac{1}{2}\left\{\frac{1}{\sigma_{3T}^2} + \frac{1}{\sigma_{1T}^2} - \frac{1}{\sigma_{2T}^2}\right\}, \quad L = \frac{1}{2(\tau_{23}^S)^2}, \quad M = \frac{1}{2(\tau_{31}^S)^2},$$

Caddell (1973)

$$N = \frac{1}{2(\tau_{12}^S)^2}$$

$$K_x = \frac{C_x - T_x}{C_x T_x}, \quad K_y = \frac{C_y - T_y}{C_y T_y}, \quad K_z = \frac{C_z - T_z}{C_z T_z}$$

$\sigma_{ij} = Components\ of\ the\ strees\ tensor$
$\sigma_{1T}, \sigma_{2T}, \sigma_{3T} = Yield\ strengths\ in\ the\ pricipal\ directions\ of\ anisotropy$
$\tau_{12}^S, \tau_{23}^S, \tau_{13}^S = Yield\ stresses\ with\ respect\ to\ the\ axes\ of\ anisotropy$
C_x, C_y, C_z
$= Absolute\ values\ of\ compressive\ yield\ strengths\ in\ the\ three\ reference\ direction$
T_x, T_y, T_z
$= Absolute\ values\ of\ tensile\ yield\ strengths\ in\ the\ three\ reference\ direction\mathbf{s}$

$$f_1\sigma_1 + f_3\sigma_3 + f_{11}\sigma_1^2 + f_{33}\sigma_3^2 + 2f_{13}\sigma_1\sigma_3 = 1 - k^2$$

$$where\ f_1 = \frac{1}{\sigma_{1T}} - \frac{1}{\sigma_{1C}}, \quad f_3 = \frac{1}{\sigma_{3T}} - \frac{1}{\sigma_{3C}}, \quad f_{11} = \frac{1}{\sigma_{1T}\sigma_{1C}},$$

$$f_{33} = \frac{1}{\sigma_{3T}\sigma_{3C}}, \quad f_{13} = -\frac{1}{2}(f_{11}f_{33})^{\frac{1}{2}}, \quad k = \frac{\tau_5}{\sigma_{13}^S}$$

Gdoutos (2002)

$\sigma_1 = Normal\ stress\ along\ the\ in - plane\ direction$
$\sigma_3 = The\ applied\ stress\ along\ the\ through - the - thickness\ direction$
$\tau_5 = Shear\ stress\ component$
$\sigma_{13}^S = Shear\ stress\ known\ from\ shear\ tests\ along\ the\ principal\ material\ e$
$\sigma_{1T}, \sigma_{1C}, \sigma_{2T}, \sigma_{2C}, \sigma_{3T}, \sigma_{3C}$
$= Uniaxial\ tension\ and\ compression\ in\ the\ three\ directions\ of\ anisotropy$

XH (2004)

$$2\sigma_e^2 = \alpha_{12}(\sigma_{11} - \sigma_{22})^2 + \alpha_{23}(\sigma_{22} - \sigma_{33})^2 + \alpha_{31}(\sigma_{33} - \sigma_{11})^2 + 6\alpha_{44}\sigma_{12}^2$$

$$+6\alpha_{55}\sigma_{23}^2 + 6\alpha_{66}\sigma_{31}^2 + \alpha_{11}\sigma_{11}^2 + \alpha_{22}\sigma_{22}^2 + \alpha_{33}\sigma_{33}^2$$

	$\alpha_{12} = \alpha_{23} = \alpha_{31} = \dfrac{9 - 2\alpha^2}{9 + \alpha^2}$ $\alpha_{44} = \alpha_{55} = \alpha_{66} = \dfrac{9}{9 + \alpha^2} \qquad \alpha = 3\left(\dfrac{\frac{1}{2} - v^P}{1 + v^P}\right)^{\frac{1}{2}}$ $\alpha_{11} = \alpha_{22} = \alpha_{33} = \dfrac{6\alpha^2}{9 + \alpha^2}$ $\sigma_{ij} = Components\ of\ the\ strees\ tensor$ $\sigma_e = Effective\ stress$ $\alpha = Parameter\ chosen\ to\ produce\ a\ specific\ platic\ Poisson's\ ratio\ v^P$
BD (1996)	$\sigma_e^2 + \alpha^2(\sigma_m - p_0)^2 = B^2, where\ \alpha = \dfrac{3k}{\sqrt{(3k_t + k)(3 - k)}}, k = \dfrac{\sigma_c^0}{p_c^0}, k_t = \dfrac{p_t}{p_c^0}$

In the case of the GAZT model, it is interesting to remark that the results in the quartic equation in biaxial principal stress space. The yield surface is parabolic in $\sigma_d - \sigma_m$ space. As mentioned previsouly, the DF model is an elliptic yield criterion for isotropic foams, where the shape parameter α is the ratio of shear to hydrostatic yield strength. It is also alternatively defined as a function of plastic Poisson's ratio obtained from uniaxial compression.

The model of Gdoutos (Gdoutos, Daniel, & Wang, 2002)(Gdoutos, 2013) is mostly the Tsai-Wu failure criterion (Tsai & Wu, 1971) that is widely used for composite materials, which are highly anisotropic and have very different strength in terms of tension and compression. The model XH (Xue & Hutchinson, 2006) requires six parameters for computing the yield surface. This anisotropic yield criterion does not account for differences in yield in terms of tension and compression values, thereby requiring buckling caps to be defined.

Finally, the last model that appears in *Table 9* is the BD model (Nuscholtz, Bilkhu, Founas, & Du Bois, 1996). It requires difficult-to-obtain hydrostatic compression and tension data along with uniaxial compression data to allow the prediction of the yield behaviour.

4.4. ELASTOPLASTIC ANALYSIS

The plasticity theory has the purpose of providing the mathematical relationships between strains and stresses that occur in a study material with an elastoplastic behaviour. After a certain stress value in the material has been reached and exceeded - which is called yield stress - a permanent strain is going to be obtained and, after unloading, will remain so. This permanent strain is designated as plastic strain. The theoretical formulation of the plasticity theory is based on three fundamental concepts (Lubliner & Moran, 1992)("'Lecture 5: Rate Independent Plasticity,' in ANSYS Mechanical Structural Nonlinearities 13.0 ed. ANSYS Customer Training Material," 2010)(Ziennkiewicz & Taylor, 2005)(Bathe & Saunders, 1984): the yield criterion, already mentioned in Section 4.3, the hardening rule and the plastic flow rule.

In order to define the elastic limit of the study material that is subjected to multiaxial stress, the yield criterion is employed and is defined as a yield surface. The hardening rule describes how the yield surface changes as the result of plastic deformation. The flow rule is related to the plastic flow potential and defines the direction of the plastic strain vector

increment on the strain space. The total strain is divided into two types of deformations: elastic strain and plastic strain, as shown in Figure 34 (Owen & Hinton, 1980)(Souza Neto, Peric, & Owen, 2008).

At the beginning of the loading, the material exhibits linear elastic behaviour that allows the use of the Hooke's law to relate the strain and the stress states. However, when the elastic limit is reached and surpassed, this law no longer applies , hence the stress state is now ruled by the plastic flow. That occurs because plastic deformation is associated with the deformation energy, which is an irreversible process. This makes the plastic deformation dependent on the load history.

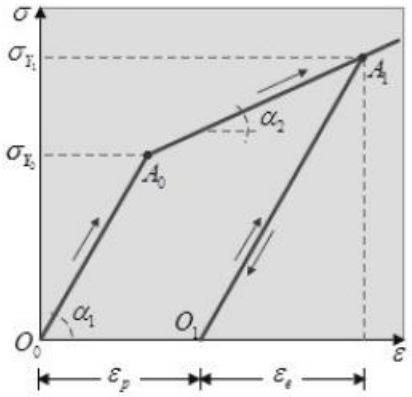

Figure 34 Bilinear elastoplastic model (Moreira, 2013)

4.4.1. Yield Criterion

This subject was already presented in Section 4.3. It is after obtaining Equation (4.51), where the yield function f presented a value equal to the yield stress of the corresponding material, σ_y, that one can observe the problem that arises in the threshold of the elasticity and at the beginning of the plastic behaviour. Since the plastic material domain is reached, the material behaviour will become conditioned by the variation of the yield function with respect to the stress state, $\boldsymbol{\sigma}$.

This variation is given by :

$$df = \left(\frac{df}{d\boldsymbol{\sigma}}\right)^T d\boldsymbol{\sigma} \tag{4.59}$$

Where $df/d\boldsymbol{\sigma}$ is a normal vector to the yield surface for a given stress state.

- If $df < 0$, the material is in elastic unloading (elastic behaviour) and the stress state is located inside the yield surface.
- If $df = 0$, neutral loading (plastic behaviour for a perfectly plastic material) and the stress point remains on the yield surface.
- If $df > 0$, plastic loading (plastic behaviour for a strain hardening material) and the stress point remains on the expanding yield surface.

4.4.2. Hardening rule

The hardening rule, as mentioned before, describes the behaviour of the yield surface as the result of plastic deformation. There are three types of hardening phenomena: isotropic hardening, kinematic hardening and mixed hardening (Owen & Hinton, 1980)(Souza Neto et al., 2008).

In the Isotropic Hardening Rule, the yield surface increases without any translation movement, this mean that it assumes that the evolution of the yield surface during plastic flow is an expansion of the initial surface with the same origin. It is important to note that the isotropic hardening rule does not consider the Bauschinger effect, as the increase of the yield function has the same effect on tension and compression (Jirásek & Bazant, 2002)(W.-F. Chen and D.-J. Han, 2007).

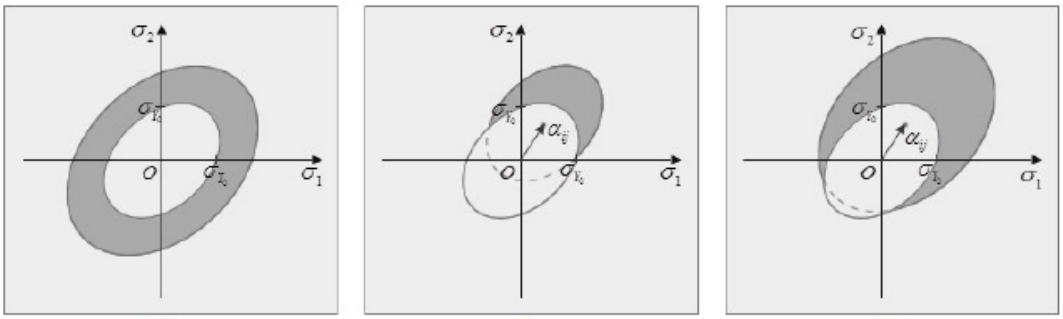

Figure 35 Hardening Rule: (a) Isotropic Hardening; (b) Kinematic Hardening; (c) Independent Hardening (Moreira, 2013)

In the case of the Kinematic Hardening Rule, the yield surface position changes without any changes in size and orientation. In other words, the evolution of the yield surface is just a translation of the surface (new centre defined). In this case, it takes the Bauschinger effect into consideration (W.-F. Chen and D.-J. Han, 2007).

Finally, there is the Independent Hardening Rule, that is a combination between the kinematic and isotropic rules. In this case, the yield surface suffers not only an expansion but also a translation and/or a rotation. The Bauschinger effect is also considered.

4.4.3. Plastic flow

The plastic flow rule establishes a connection between the yield function f and the relationship between strain/stress for a material with elastoplastic characteristics. Applying the Prandtl-Reuss flow rule to the yield function leads to Equation (4.60). Figure 36 shows a schematic representation of the plastic flow (Crisfield et al., 2000):

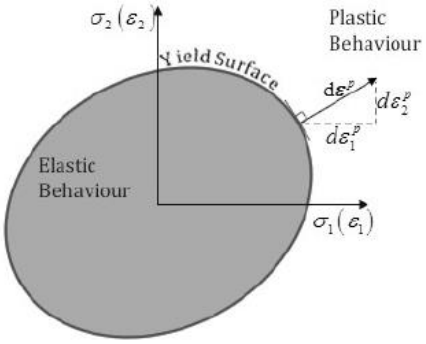

Figure 36 Flow rule (normality principle)(Moreira, 2013)

$$d\boldsymbol{\varepsilon}_P = d\lambda \frac{df}{d\boldsymbol{\sigma}} \tag{4.60}$$

where $d\lambda$ is the plastic strain-rate multiplier.

From the analysis of Figure 36, it is possible to identify the following situations (Bathe & Saunders, 1984)(J. A. Belinha, 2004b):

- If $d\lambda < 0$, the situation is elastic unloading. This means that the stress state returns to the inside of the yield surface. Also, Hooke's law applies.

- If $d\lambda = 0$, the stress state is on the yield surface. In the case where the material has not undergone a hardening process, σ_y is independent of k, meaning the occurrence perfectly plastic models. On the other hand, if the material has suffered hardening, the situation corresponds to the beginning of the plasticity.

- If $d\lambda > 0$, the stress state is on a constantly expanding yield surface.

4.4.4. Mathematical Expressions

As stated previously, Hooke's law is no longer valid when the material enters in the plastic domain. This is because the total strain is now composed by elastic and plastic strains. When the material is located in the elastic zone, the tangent to the curve stress-strain is equal to the Young's Modulus, E, but when the material enters in the plastic domain, the tangent of the curve is called the elastoplastic modulus or tangent modulus, E_T, which is continuously changing (J. A. Belinha, 2004b).

The hardening rule is defined, in plasticity, according to the effective stress and strain:

$$\boldsymbol{\sigma_Y} = H(\boldsymbol{\varepsilon}_P) \tag{4.61}$$

where H is the hardening function.

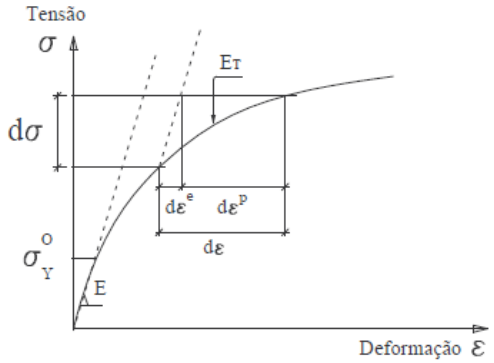

Figure 37 Elastoplastic behaviour with hardening in a uniaxial test (J. A. Belinha, 2004a)

Differentiating Equation (4.61) and considering an uniaxial load:

$$\frac{\partial \boldsymbol{\sigma_Y}}{\partial \boldsymbol{\varepsilon}_P} = H'(\boldsymbol{\varepsilon}_P) \tag{4.62}$$

Through Equation (4.62) and Figure 37, the hardening rule is defined as:

$$H'(\varepsilon_P) = \frac{\partial \sigma_Y}{\partial \varepsilon_P} = \frac{d\sigma_Y}{d\varepsilon - d\varepsilon_e} = \frac{1}{\frac{d\varepsilon}{d\sigma_Y} - \frac{d\varepsilon_e}{d\sigma_Y}} = \frac{1}{\frac{1}{E_T} - \frac{1}{E}} = \frac{E_T}{1 - \frac{E_T}{E}} \tag{4.63}$$

Thus, the hardening parameter can be determined experimentally with a simple uniaxial yield test (Owen & Hinton, 1980).

Returning to the yield function, Equation (4.44), and differentiating :

$$dF = \left(\frac{\partial f}{\partial \boldsymbol{\sigma}}\right)^T d\boldsymbol{\sigma} - \frac{\partial \sigma_Y}{\partial k} dk = 0 \tag{4.64}$$

or

$$\boldsymbol{a}^T d\boldsymbol{\sigma} - A d\lambda = 0 \tag{4.65}$$

where $\boldsymbol{a}$ is the flux vector, that for the three-dimensional situation can be defines as follows:

$$\boldsymbol{a} = \frac{\partial f}{\partial \boldsymbol{\sigma}} = \left[\frac{\partial f}{\partial \sigma_{xx}}, \frac{\partial f}{\partial \sigma_{yy}}, \frac{\partial f}{\partial \sigma_{zz}}, \frac{\partial f}{\partial \tau_{xy}}, \frac{\partial f}{\partial \tau_{yz}}, \frac{\partial f}{\partial \tau_{zx}}\right]^T \tag{4.66}$$

where A is the defined by the expression:

$$A = \frac{1}{d\lambda} \frac{\partial \sigma_Y}{\partial k} dk \tag{4.67}$$

It is important to remark that this parameter dependens on considering the hardening rule to be completed defined.

In order to determine A, the isotropic work hardening is going to be considerered. Through Equation (4.44), the yield stress becomes a function of the plastic work, $\sigma_Y(k = W_P)$, being W_P the plastic work given by the following model:

$$k = W_P = \int \sigma_Y d\varepsilon_P = \int \boldsymbol{\sigma}^T d\boldsymbol{\varepsilon}_P = \int d\lambda \boldsymbol{\sigma}^T \boldsymbol{a} \tag{4.68}$$

Thus, the plastic work rate is given by:

$$dk = dW_P = \sigma_Y d\varepsilon_P = \boldsymbol{\sigma}^T d\boldsymbol{\varepsilon}_P = d\lambda \boldsymbol{\sigma}^T \boldsymbol{a} \tag{4.70}$$

Substituting, Equation (4.70) in Equation (4.67), the hardening constant can be written as:

$$A = \boldsymbol{\sigma}^T \boldsymbol{a} \frac{\partial \sigma_Y}{\partial k} \tag{4.71}$$

In order to have a totally defined value of A, the explicit relation between the uniaxial stress (σ_Y) and the hardening parameter k has to be defined. This relation can be written showing the variables related with the plastic strain $\boldsymbol{\varepsilon}_P$:

$$\frac{\partial \sigma_Y}{\partial k} = \frac{\partial \sigma_Y}{\partial \varepsilon_P} \frac{\partial \varepsilon_P}{\partial k} \tag{4.72}$$

Substituting Equation (4.70) in Equation (4.72), the following expression is obtained :

$$\frac{\partial \sigma_Y}{\partial k} = \frac{\partial \sigma_Y}{\partial \varepsilon_P} \frac{1}{\sigma_Y} \tag{4.73}$$

From the uniaxial stress/plastic strain relationship between σ_Y and ε_P, Equation (4.74) can be obtained using Equations (4.63) and (4.73):

$$\frac{\partial \sigma_Y}{\partial k} = \frac{H'}{\sigma_Y} \tag{4.74}$$

Therefore, the hardening constant A, is defined as :

$$A = \frac{H' \boldsymbol{\sigma}^T \boldsymbol{\sigma}}{\sigma_Y} \tag{4.75}$$

Since the yield is a first order homogeneousfunction, the Euler's theorem (Owen & Hinton, 1980) shows that :

$$\frac{\partial f^T}{\partial \boldsymbol{\sigma}} \boldsymbol{\sigma} = \boldsymbol{a}^T \boldsymbol{\sigma} = \sigma_Y \tag{4.76}$$

Hence, $A = H'$.

Returning to the relation stress and strain, the variation of the stress state can be developed taking into account Equations (4.60) and (4.64) :

$$d\boldsymbol{\sigma} = \boldsymbol{c} d\boldsymbol{\varepsilon}_e = \boldsymbol{c} d\boldsymbol{\varepsilon} - \boldsymbol{c} d\boldsymbol{\varepsilon}_P = \boldsymbol{c} d\boldsymbol{\varepsilon} - d\lambda \boldsymbol{c}\boldsymbol{a} \tag{4.77}$$

Combining Equation (4.65) and (4.77), it is possible to define the plastic strain-rate multiplier :

$$d\lambda = \frac{\boldsymbol{a}^T \boldsymbol{c} d\boldsymbol{\varepsilon}}{A + \boldsymbol{a}^T \boldsymbol{c} \boldsymbol{a}} \tag{4.78}$$

Substituting Equation (4.78) in Equation (4.60), the expression for the plastic strain is obtained:

$$\boldsymbol{\varepsilon}_P = d\lambda \boldsymbol{a} = \frac{\boldsymbol{a}^T \boldsymbol{c} d\boldsymbol{\varepsilon}}{A + \boldsymbol{a}^T \boldsymbol{c}\boldsymbol{a}} \boldsymbol{a} \tag{4.79}$$

Considering the results obtained, it is possible to present the mathematical relation between stress and strain:

$$d\boldsymbol{\sigma} = \boldsymbol{c}^{\boldsymbol{ep}} d\boldsymbol{\varepsilon} = \left(\boldsymbol{c} - \frac{\boldsymbol{c}\boldsymbol{a}\, \boldsymbol{a}^T \boldsymbol{c}}{A + \boldsymbol{a}^T \boldsymbol{c}\boldsymbol{a}} \right) d\boldsymbol{\varepsilon} \tag{4.80}$$

where $\boldsymbol{c}^{\boldsymbol{ep}}$ is the elastoplastic constitutive matrix:

$$\boldsymbol{c}^{\boldsymbol{ep}} = \boldsymbol{c} - \frac{\boldsymbol{c}\boldsymbol{a}\, \boldsymbol{a}^T \boldsymbol{c}}{A + \boldsymbol{a}^T \boldsymbol{c}\boldsymbol{a}} \tag{4.81}$$

4.4.5. Nonlinear Solution Algorithms

Elastoplastic studies require nonlinear equations that cannot be solved directly. Because of that, the use of incremental methods is required in order to obtain the solution to those equations. The incremental methodss apply successive loads increments to achieve an approximate solution of the problem.

(a) Stress Returning Algorithm

During the implementation of the equation from the yield criteria in the numerical program, it is necessary to ensure that the stresses remain under the yield surface or very close to the yield surface, in order to avoid cumulative error and overpredicted loads. To solve this problem, stress returning algorithms are applied (Owen & Hinton, 1980). The procedure employed to return the stress to the yield surface is the designated the 'Backward-Euler scheme', Figure 38.

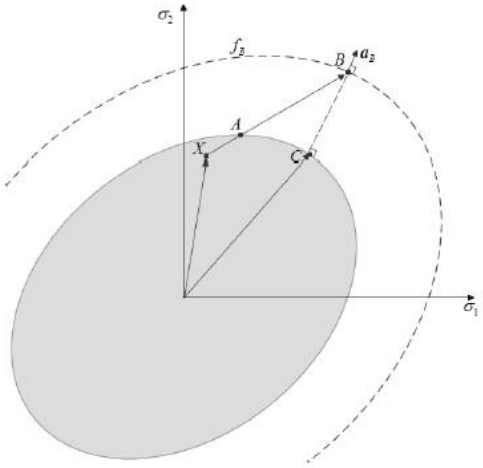

Figure 38 Backward-Euler scheme (Moreira, 2013)

This method acts on the Gauss point level in order to solve the nonlinear equation. After each incremental load and for each Gauss point, the stress state is verified on whetherit falls inside or outside of the yield surface. In order to do this verification, the stress state for each Gauss point is compared with the yield criterion, as shown in Equation (4.82), with $f(\boldsymbol{\sigma})$ defined

as the yield surface defined as presented in Section 4.4.1. The parameters σ_Y^* and $\bar{\varepsilon}_{i-1}^p$ are the updated yield stress and the accumulated effective plastic strain from the previous increment $(i-1)$. In the situation where the Gauss point has not entered in plasticity yet, the accumulated effective plastic strain is null. Therefore, the updated yield stress will be equal to the reference yield stress :

$$f(\boldsymbol{\sigma}) \leq \sigma_Y^* \tag{4.82}$$

$$\sigma_Y^* = \sigma_Y + \left[E_T\, \bar{\varepsilon}_{i-1}^p\right] \tag{4.83}$$

This algorithm is required every time Equation (4.82) is not verified. In this case, point B of Figure 38 has to be pushed to point C, which is on the yield surface. To accomplish that, the algorithm starts with a predictor that simulates that point B is under a yield function f_B. For point B, the flow vector is calculated and the yield function in point B is given by $f_B = \bar{\sigma}_B - \sigma_Y^*$. The following step is to calculate the plastic multiplier $d\lambda$ using Equation (4.84) :

$$d\lambda = \frac{f_B}{\boldsymbol{a}_B^T \boldsymbol{c} \boldsymbol{a}_B + H'} \tag{4.84}$$

being H' calculated through Equation (4.63).

Having defined these terms,it is thus possible to estimate the value of the stress in point C, as a starting estimate :

$$\boldsymbol{\sigma}_C = \boldsymbol{\sigma}_B - d\lambda \boldsymbol{c} \boldsymbol{a}_B \tag{4.85}$$

To calculate the stress point in C, it is necessary to use the flow vector of the same point.

$$\boldsymbol{\sigma}_C = \boldsymbol{\sigma}_B - d\lambda \boldsymbol{c} \boldsymbol{a}_C \tag{4.86}$$

The flow vector C requires more information apart from the data with respect to points X and B. For this, it is necessary to use an iterative procedure, using the data from B, to approximate point B to point C. The effective plastic strain is updated in each iteration in order to apply Equation (4.83). At the end of the routine, point B will be close of point C, so the flow vectors for each point would be almost the same. The stopping point of the criterion is determined via a pre-defined tolerance.

(b) Nonlinear solution algorithm: Modified Newton-Raphson (KT0), (KT1) and (KTALL).

Figure 39(a) show how to obtain the displacement u for each load increment Δf, through Equation (4.87).

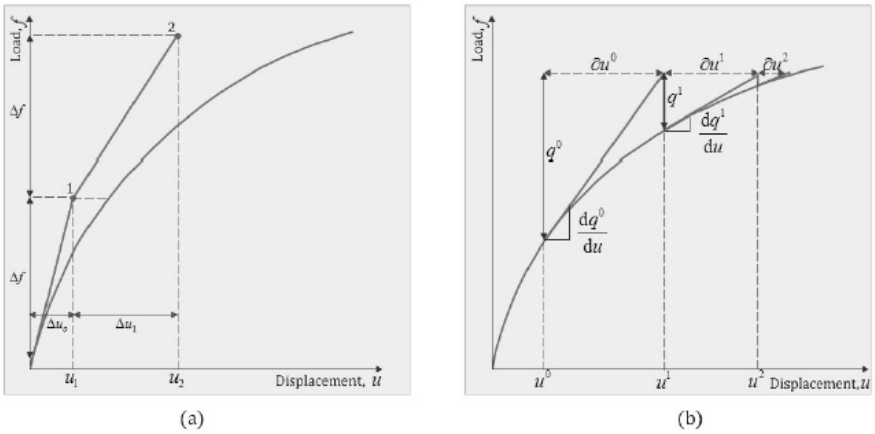

Figure 39 (a) Incremental (Euler) solution scheme; (b) Newton-Raphson method(Moreira, 2013)

$$\Delta u = \left(\frac{df}{du}\right)^{-1} \Delta f = K_T^{-1} \Delta f \tag{4.87}$$

The incremental method presents small errors that will accumulate in the several load stages due to the lack of equilibrium. This, inevitably, moves away from the solution for the true equilibrium curve. It is also expected that the more nonlinear the solution $(df/du \to 0)$, the more deteriorated the results obtained will be.

In order to solve this contingency, an iterative solution such as the Newton-Raphson method can be used. Taking into account the simple form of the Newton-Raphson method, it is only provided with the displacement u of a fixed load f, as shown in Figure 39(b). The iterative j changes follow Equation (4.88) :

$$\partial u^j = \left(\frac{dq^j}{du}\right)^{-1} q^j(u^j) \tag{4.88}$$

The successive displacements are given by the following expression:

$$u^j = u^{j-1} + \partial u^{j-1} \tag{4.89}$$

The iterative Newton-Raphson method can be combined with the incremental method, allowing to obtain the problem response and the reduction of the lack of equilibrium.

In this combination (Figure 40(a)), the incremental method acts as a predictor, generating the starting solution u_i^0 for the iterative procedure. The advantage of this combination is that using the predictor through the incremental method allows to improve the convergence of the iterative procedure, thereby reducing the number of iterations.

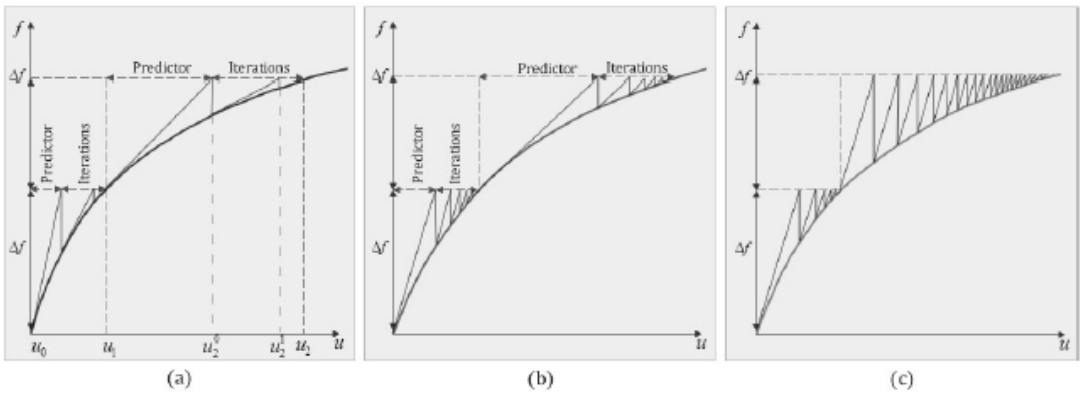

Figure 40 (a) Combined incremental and Newton-Raphson method; (b) Combination of the incremental predictor with modified Newton-Raphson iterations (KT1); (c) Initial stress method combined with an incremental solution (KT0) (Moreira, 2013)

Also, this procedure requires constant calculations of the stiffness matrix and its inverse, a procedure that becomes slow and costly in terms of computational time and resources.

The simplest of these methods is the one designated as KT0, where the tangent stiffness matrix is considered the same for all the increments and iterative processes. It is represented in Figure 40(c). One of the problems with this method is the long computational time that is required for converging to the solution.

The other method is called KT1, and the principal difference with respect to the KT0 method is that, in this case, the tangent stiffness matrix is updated and inverted in the first iteration of each incremento of the incremental load. This method is represented in Figure 40(b). Also, the inconvenience of this method is the need to update and invert the tangent stiffness matrix, a process that cost computational time. However, the positive aspect is that the convergence to the solution is faster than with the KT0 method.

Finally, the last method and the one that was used in this work is the '*Full Newton-Raphson method (KTALL)*'. This method updates and inverts the tangent stiffness matrix in each iteration of the increment, allowing the procedure to converge to the solution faster than using the other two methods. In terms of computational costs, it present a high-level computational requirement in order to calculate and invert the tangent stiffness matrix in each iteration.

Chapter 5

NUMERICAL METHOD: BACKGROUND

5.1. FINITE ELEMENT METHOD

The Finite Element Method (FEM) emerged in the aeronautical and civil areas in order to solve problems with complex behaviour. This method appeared for the first time in 1941, by A. Hrennikoff (1941), who proposed that the continuum structure could be discretised in elements connected by a finite number of points (the nodes). Through the torsional problems of Courant in 1943, the FEM was developed for the next year and in 1956 was the designated, for the first time,"Finite Element Method" by Clough (1956). Although the finite element method was initially developed mostly based on intuition and physical arguments, the method was recognised as a form of the classical Rayleigh-Ritz method in the early 60s. At the beginning of the 70s, digital computers provided a rapid means of performing the many calculations involved in the finite element analysis and caused the application of the finite element method to progress exponentially. Zienkiewicz & Cheung (1967) presented the broad interpretation of the method and its applicability to any general field problem. J.S. Przemieniecki (1967) presented the finite element method as applied to the solution of stress analysis problems.

Through this interpretation of the method, it has been found that the finite element equations can also be derived by using the weighted residual method such as the Galerkin method of the least squares approach. This caught the attention of mathematicians, who then began apply the FEM for solving linear and nonlinear differential equations.

The FEM is a numerical method that seeks for an approximated solution in the distribution of a few field variables within the problem domain. It simplifies complex problems by dividing the problem domain into several elements. These elements are linked by nodes that, together, constitute a mesh. Physical laws are applied to each element and, using the proper principles; it is possible to establish the equations for each element. Finally, it is necessary to connect all the elements, leading to a set of algebraic equations that can be solved to obtain the required field variables (G. R. Liu & Quek, 2003).

On the other hand, even though FEM has been a successful method in many engineering fields, it presents a few limitations related to the mesh dependency. These limitations become apparent in problems that contain large deformations, such as crack propagation, interface between solid-fluid or complex geometries and when highly distorted meshes are present.These situations lead to a significant decrease in the accuracy of the results. In order to solve these situations, the problem uses a remesh in each step, which produces a high computational cost and degradation of the accuracy.

In an attempt to estimate the error without excessively increasing the numerical effort, considerable work has been made towards improving the accuracy of this parameter. Since the exact solution is unknwon, most of the attention is directed to a posteriori error estimates.

This error estimation not only provide information about the accuracy of the solution but also give the distribution within the existing mesh. Because of that, this parameter is employed

as an indicator to refine the mesh. This process was called adaptive FEM and allows to solve the problems related with meshing (L. Li & Bettess, 1997).

5.1.1. FINITE ELEMENT METHOD IN CELLULAR SOLIDS

The finite element method (FEM) is employed widely for the prediction of the mechanical response of fluids and structures. Because of its high versatility that allows for modelling of complex material and structural behaviours, FEM has been applied strongly to simulations of the mechanical behaviour of cellular materials.

Cellular materials exhibit a discrete structure at the microscopic level, with a skeleton of solid material being surrounded by a gas or fluid.

They are also defined by their low relative density, which is typically in the range of a few percentages of the solid volume fraction. A review of the biomechanics of cellular solids can be found in section 2.1 of this work.

The main focus of this contribution lies on Finite Element models of the microstructure of human-made cellular materials such as polymer foams, ceramic foams and metallic foams.

Homogenisation and the Unit Cell Method

This technique that consists in deriving the micro-mechanical properties of a microstructured material from the micro-mechanical behaviour is a process called "*homogenisation*". The opposite process that involves the transition from macro-mechanical stresses or strains to local deformations and micro-mechanical stress and strain fields is called "*localisation*". These two techniques are compared in Böhm, Pahr, & Daxner (2010).

Cellular materials show a limited elastic range, and the mechanical behaviour tends to be dominated by microscopic deformation mechanisms such as bending of struts and buckling of cell walls. These deformation mechanisms are influenced by the micro-geometry, which is typically complex and highly non-uniform in the case of solid foam.

In order to represent the micro-structured material using micromechanical finite element models, the following principal modelling approaches are announced.

- **Multi-cell models of finite samples**. This approach aims to predict the behaviour of an actual foam sample under realistic loading conditions, which, in most cases, corresponds to uni-axial compression.

- **Unit-cell models.** These types of models are more concerned with an efficient treatment of the material as an infinite medium. The unit-cells typically consist of a regular, periodic arrangement of a limited number of base cells, which are modelled in high geometrical detail. Geometrical periodicity and periodicity boundary conditions ensure that the unit cell is space-filling both in the undeformed and the deformed states. These models are suitable for a controlled study of the influence of various geometrical parameters on the effective behaviour.

- **Embedded-cell models** are hybrid models that feature a micro-geometrically fully resolved "core", which is embedded in a matrix of surrounding material.

The effective behaviour of the matrix corresponds closely to the effective behaviour of the embedded cell.

These different modelling strategies, which have well-establish equivalents in continuum micro-mechanics of composite materials, give information about the local deformation mechanisms and the corresponding overall behaviour, which can be obtained by homogenisation.

The unit cell method assumes that the behaviour of an infinite periodic structure can be represented by a model of finite size. This model is a combination of a geometrically representative building block, which allows for a seamless, periodic tiling of space, and appropriate boundary conditions, which ensure the periodicity of the displacement field of the structure. In general, two and three vectors of periodicity are required for the description of periodic 2D and 3D structures. For mechanical problems, the displacement components of those points on the boundary of the unit cell, which can be mapped onto each other by a translation along a linear combination of integer multiples the vectors of periodicity, have to be coupled by kinematic constraints.

Note that the unit cell model is not intended to represent only a regular and geometrically periodic microstructure, but rather a random material with all kinds of irregularities and imperfections. This situation arises from the question of, *how many cells a unit cell model is required to have to be representative of the actual microstructure?*. The answer to this question can be found in Hashin (1983).

Micromechanical Finite Element Models of Cellular Solids

This section focuses on describing the micromechanical finite element models as a suitable representation of the microstructure of cellular materials. First, it will explain the cellular materials that are the result of solidifying a liquid foam, for example, polymer or metal foam.

- **Solidified Liquid Foams**. Liquid foams are governed by the laws of Laplace and Plateau. The law of Laplace states that the mean local curvature of the cell wall is:

$$\mathrm{H} = \frac{1}{2}\left(\frac{1}{R_1} + \frac{1}{R_2}\right) \tag{5.1}$$

where R_1 and R_2 are the minimum and the maximum local radio of curvature, respectively, is proportional to the pressure difference Δp between the cells that are separated by the cell wall.

The cells of the solid foam correspond to bubbles of the liquid foam. These bubbles have the polyhedral shape, with cell walls meeting in edges and edges meeting in vertices. This specific kind of edge geometry is known as Plateau border.

- **Kelvin Cell**. As mentioned in Section 2.1.2. Lord Kelvin proposed polyhedralcells with the same volume and periodic structure as an answer to the question concerning which space-filling arrangement of cells of equal volume had minimal surface area. Figure 6 is possible to use an example of this type of cell.

- **Weaire-Phelan Cells**. This type of cells was also presented previously in Section 2.1.2. They found a periodic structure consisting of two different kinds of polyhedrons of equal volume (Figure 7), which have a slightly smaller surface area than a Kelvin foam.

- **Voronoi Diagrams**. Another popular method for creating models of cellular solids is the Voronoi diagram, that is desceribed in Section 2.1.2 and shown in Figure 11 and Figure 12.

- **Simulation of the Foaming Process**. The foaming process is simulated in order to obtain suitable micro-structural models of the solidified foam. Körner (2008) proposed a 2D aproach and Bikard, Bruchon, Coupez, & Vergnes, (2005) presented a 3D simulation of the evolution of polymer foam during the foaming process.

- **Micro-Computed Tomography**. In order to obtain detailed information about the internal structure of the cellular solids, X-ray computed tomography (XRCT) was developed, which enables a direct and non-destructive 3D characterisation of the foam's microstructure (Salvo, Suéry, Marmottant, Limodin, & Bernard, 2010), (Stock, 2008). An example of this methodology is discussed in the study of Jang, Kraynik, & Kyriakides (2008).

- **Hollow Sphere Structures (HSS)**. A cellular structure with a very well defined micro-geometry can be obtained bonding small hollow spheres together (Augustin & Hungerbach, 2009).

- **Overlapping Issues when using Structural Elements**. Open cell foams and thin cell walls in closed-cell foams are not well suited for being discretised with finite continuum elements because a significant number of elements with unfavourable aspect ratios would be necessary to mesh them. A thorough discussion of different approaches to modelling open-cell foam can be found in Jang et al. (2008).

- **Models of Sample Finite Size**. Because of the large computational effort that is necessary to simulate a structure with hundreds of individual cells, these models have so far been restricted to 2D problems (honeycombs), open-cell 3D models, for which 3D beam models can be employed, (Gong & Kyriakides, 2006), and continuum element models in the elastic regime, (Kirca, Gül, Ekinci, Yardim, & Mugan, 2007).

Open and Closed Cell Foams

One of the most important differentiations in the cellular solid world is the one between open cell and closed cell structures. Also, this distinction is applied in FE to create a different model and choosing the best type of element to depend on the structure.

The type of element selected is important to obtain an accurate model. Some of the most used are cubic elements, beams or wall elements and tetrahedral elements.

Cubic FE for Open and Closed Cell -Foams

The use of cubic elements consists in translating one voxel into an element of the mesh. This meshing technique has been used on polymer, metal or ceramic cellular materials, mainly for the determination of Young's modulus and Poisson's ratio by Saadatfar, Arns, Knackstedt, & Senden (2005), Garboczi & Day (1995) and Arns, Knackstedt, Pinczewski, & Garboczi (2002). It has also been used for determining thermal conductivity of metal hollow sphere structures (Fiedler, Hosseini, Belova, Murch, & Öchsner, 2009) or the influence of oxidation of nuclear graphite on mechanical properties (Berre et al., 2008).

The main difficulty of this meshing technique is representing the details of the sample microstructure. The cubic elements do not correctly follow the curved surface. Different solutions exist to increase mesh resolution (at high computational cost), such as adopting an FE program to mesh large samples (Roberts & Garboczi, 2001) or using a fast Fourier transform technique (Escoda, Willot, Jeulin, Sanahuja, & Toulemonde, 2016). This technique that is increasingly being replaced by meshing with noncubic elements, allowing for shorter computation times.

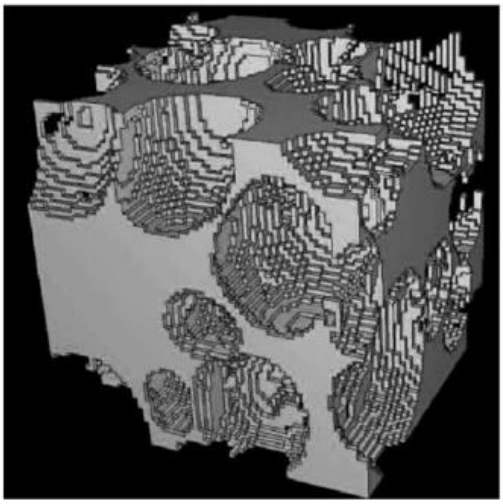

Figure 41 Voxel mesh of PU foam (Maire et al., 2003)

Beam FE for Open-Cell Foams.

Beam elements are the natural choice for the discretisation of open-cell foams. This is because they are computationally inexpensive and can be used to compose models with many cells. However, it is important to consider and avoid the issues that arise from overlapping beam elements in the vertices. Also, beam-to-beam contact can cause problems in high-strain compression situations. Most studies involving 3D beam models of open-cell foam deal with the latter (hyper-)elastic properties. Indeed, relevant studies use a circular cross-section in the elastic-plastic regime, (Jang & Kyriakides, 2009).

Shulmeister, Van Der Burg, Van Der Giessen, & Marissen (1998), investigated the nonlinear tension/compression test for open-cell Kelvin foam, a rhombic dodecahedron structure and a random Voronoi foam, using different elastic material laws.

H. Zhu, Hobdell, & Windle (2000) investigated the influence of cell shape regularity in periodic Voronoi unit cell models on the elastic properties. H. X. Zhu & Windle (2002) crushed

periodic Voronoi foam models with linear elastic strut material to up to 60% of compressive strain.

Gan, Chen, & Shen (2005) predicted elastic properties of random, periodic Voronoi models in the presence of imperfections. K. Li, Gao, & Subhash (2006) investigated regular and irregular periodic models of carbon foams concerning the influence of cell disorder and the shape of the strut cross-section. L. Gong & Kyriakides (2006) studied the collapse of large-scale Kelvin foam models using nonlinear springs as substitutes for severe contact conditions. Jang et al. (2008) investigated the elastic properties of polyester urethane and Duocel aluminium foam using different FE models, offering the opportunity to compare results obtained by different modelling approaches.

Shell FE for Closed-Cell Foams

Finite shell elements are an efficient means for modelling closed-cell foams. It is important to take shell thickness into account in order to avoid the virtual overlapping of material where the faces meet. In order to introduce the stiffness of Plateau borders into the model, the superposition of a finite beam element model along the edges of the shell model must be included. The earliest finite shell element model was proposed by Santosa & Wierzbicki (1998).

Simone & Gibson (1998) proposed a sophisticated shell model of a closed-cell Kelvin foam for predicting the influence of curved and wavy cell walls on the elastic stiffness and the limit load. Grenestedt & Tanaka (1999) investigated the influence of irregularity on the elastic stiffness of a Voronoi foam created by disturbing a regular Kelvin foam structure.

Meguid (2002), Czekanski (2005a), Czekanski (2005b) and Kim (2006) proposed a finite shell element models based on intersecting planar faces as well as spheres or ellipsoids. All these models were used to predict the uniaxial force-displacement behaviour of closed-cell foam during crushing. A dry Weaire-Phelan foam model was investigated regarding its elastic properties and its yield surface by Daxner (2006). Taking into account the pressure of the enclosed gas, Mills (2009) presented a shell model for simulating the crushing of two layers of dry Kelvin foam cells.

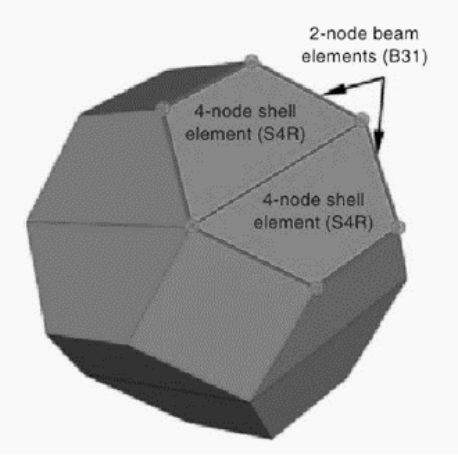

Figure 42 Schematic representation of the meshing of a PVC foam cell with beam and shell (Fischer, Lim, Handge, & Altsťdt, 2009)

Another type of meshing technique involves using beams and shells elements. Both of them can be used for microstructure composed of structural elements. This is very oftenly done for polymer foams (Fischer et al., 2009) and stainless steel hollow sphere foams (Caty, Maire, Youssef, & Bouchet, 2008). The most frequently used is shell elements, where an elastoplastic

law is used to model the behaviour of the solid material constituting the shells. However, the beam element, in some cases, cannot represent correctly the structure of the material because the beams are not well adapted to the struct geometry (Elliott & Windle, 2002).

Continuum Finite Element Models for Open-Cell Foam

Because of the high computational cost that is required for the fine discretisation needed in the slender struts or Plateau border network, continuum solid element model for open-cell foams are rarely produced.

Roberts & Garboczi (2001) presented a voxel-to-element technique for obtaining various random 3D open-cell micro-structures and predicting their elastic properties. Boomsma (2003) and Mills (2005) proposed open-cell models with fully modelled Plateau border geometries in the context of permeability analyses using computational fluid dynamics. Kirca (2007) discussed a large-scale continuum FE model for a whole sample of open-cell carbon foam considering the linear elastic response of the model to uniaxial compression. Kou, Li, Yu, & Cheng (2008) propose a unit cell model for open-cell aluminium foam which is produced by infiltrating closely packed spheres. Sihn & Roy (2004) proposed a similar model for predicting the elastic constants of open-cell carbon foam.

Continuum Finite Element Models for Closed-Cell Foam

The first researchers to propose a continuum finite element model for predicting the influence of the material distribution between the Plateau borders and the cell walls on the effective elastic modulus and the effective peak stress were Simone & Gibson (1998). Using the combination of symmetric and anti-symmetric boundary conditions, they came up with a very small unit cell model that is still a model of showing high numerical accuracy.

Roberts & Garboczi (2001) used a voxel-to-element method for setting up random 3D models of closed-cell foam. Instead of using x-ray tomography was employed rather Voronoi diagrams and Gaussian random field. Wang (2009) used a Kelvin foam model for predicting the stiffening effect of reinforcing a closed-cell polypropylene foam with randomly distributed short fibres. The short fibres were introduced into the model as beam elements.

Maire (2003) demonstrated the use of the voxel-to-element method for creating a model of closed-cell polyurethane foam from CT scans. Youssef, Maire, & Gaertner (2005) also created a model of closed-cell PU foam using an unstructured mesh of second-order tetrahedra. Jeon (2009) discretised x-ray tomography of two small samples of closed-cell aluminium foam in detail. Second-order tetrahedral finite continuum element was used.

Tetrahedral FE for Open and Closed Cell Foams

The meshing technique that describes more precisely the actual structure of cellular solids is using tetrahedral elements. One of the first studies of tetrahedral meshing was carried out on trabecular bones (Ulrich, Van Rietbergen, Weinans, & Rüegsegger, 1998).

Regarding macroscopic properties, Vesenjak, Veyhl, & Fiedler (2012) use the method to demonstrate the influence of the anisotropy and the strain rate sensitivity on the compressive behaviour of aluminium foam. It is important to remark that this technique overestimates the

elastic stiffness (Marcadon et al., 2012) and nowadays, there is still not a clear explanation of why the models are stiffer than the experimental materials.

Another important aspect is to take into account the computation of fluid flow in the porous space of a cellular matrix (Sandino, Planell, & Lacroix, 2008).

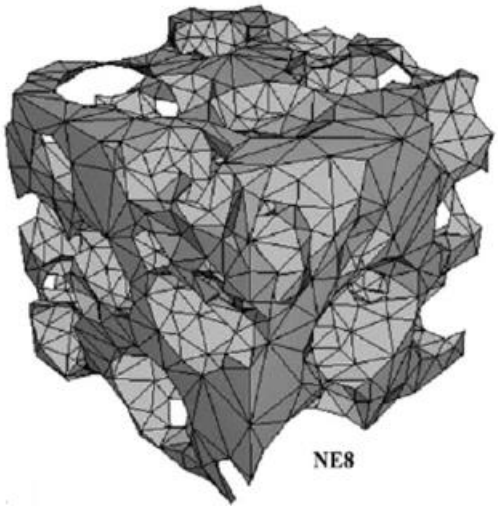

Figure 43 Tetrahedral mesh of polyurethane foam (Youssef et al., 2005)

New numerical methods for Cellular Solids

Other techniques can be used to mesh a cellular solid, such as mixed meshes made of different elements (Veyhl, Belova, Murch, Öchsner, & Fiedler, 2010). First of all, the surface of the solid meshes with triangles. Then, a volume mesh is created with hexahedra. Tetrahedra and pentahedral are added where hexahedra cannot fill the overall volume. The comparison between the different meshes for metallic foam shows that mixed meshes give the most accurate results. Also, the discrete element method was also used to simulate the mechanical behaviour of entangled materials (made of fibres) (Barbier, Dendievel, & Rodney, 2009).

5.2. MESHLESS METHOD

Meshless methods or meshfree methods (MMs) have emerged because of the high computational cost and degradation of the accuracy that more frequently appears in problems discretised by the FE method. Also, one important aspect that drives the initial research towards using the meshless method was the necessity to modify the internal structure of the grid-based FEM to make it more adaptive, versatile and robust. Much effort is concentrated on problems for which the application of conventional FEM is challenging. Such is case of problems with free surfaces, deformable boundaries, large deformations, complex mesh generations, mesh adaptivity and multi-scale resolutions (Belytschko, 1996).

Meshfree methods use a set of nodes scattered within the problem domain as well as a set of nodes scattered on the boundaries of the domain, in order to better represent the problem domain and its boundaries. These set of scattered nodes do not form a mesh, which means that any information between the nodes is required at least for the field variable interpolation. The fundamental aim behind the meshless method is to provide accurate and stable numerical solutions with all types of possible boundary conditions within a set of arbitrarily distributed nodes without using any mesh that proves the connectivity of these nodes.

The approximation function at a point in FEM is constructed at the element-level natural coordinates and then transformed to the global Cartesian coordinates, whereas meshless approximation functions are constructed using only nodal data directly in the global Cartesian coordinate system.

Based on the formulation, meshless methods can be divided into two major categories: methods based on strong form formulations and methods based on weak form formulations. Most of the current meshless applications have been based on the Galerkin (global weak-form) formulation. Galerkin-based meshless methods are similar to FEM in that they both require numerical integration to form the discretised system of equations.

Some of the common methods for generating the basis functions include the moving least square (MLS) method (Krysl & Belytschko, 1999), the reproducing kernel particle method (RKPM) (W. K. Liu & Chen, 1995) and point interpolation method (G. R. Liu, 2003). Galerkin-based meshless methods require higher-order numerical integration and a background mesh (though unlike the mesh in FEM, it is not entirely dependent on the nodes) for the global integration, which tends to increase the computational cost. Additionally, most of the shape functions formulation available for meshless methods do not satisfy the Kronecker delta property (Dinis et al., 2007), which often makes it difficult to directly apply the essential and natural boundary conditions.

The strong form methods, such as point collocation method (Aluru, 2000) and finite point method (Oñate, Idelsohn, Zienkiewicz, & Taylor 1996; Oñate, Perazzo, & Miquel, 2001), have attractive advantages of being simple to implement, computationally efficient and truly meshfree, as they do not even require a background mesh since no integration is necessary to establish the discrete system of equations. Such distinct features facilitate the implementation of the refinement or coarsening scheme since a node can be easily inserted or removed without a great deal of concern regarding the nodal connectivity. However, they are often unstable and less accurate, mainly when irregularly distributed nodes are used for problems that are governed by partial differential equations (PDEs) with Neumann boundary conditions, (Cheng & Cheng, 2005). This is the case for solid mechanics problems with stress (natural) boundary conditions.

On the other hand, weak form methods, such as the EFG method (T. Belytschko, Lu, Gu, & Tabbara, 1995) and meshless local Petrov Galerkin (MLPG) method (Atluri & Zhu, 1998), are well-established methods due to the advantage of excellent stability and accuracy. The Neumann boundary conditions can be naturally satisfied due to the use of the weak form that involves smoothing (integral) operators. However, the weak form method is said not to be "truly" meshfree, as a background mesh (local or global) is required for the integration of the weak form. An extensive overview of these methods can be found in (Belytschko et al., 1996; V. P. Nguyen, Rabczuk, Bordas, & Duflot, 2008; Chen, Hillman, & Chi, 2017).

5.2.1. Relevant Meshless Methods

One of the first Meshfree methods is called the Smooth Particle Hydrodynamics (SPH) method and was developed by Lucy (L. B. Lucÿ, 1977) and Gingold and Monaghan (R. A. Gingold and J. J. Monaghan, 1977) in order to solve astrophysics problems and, later on, fluid dynamics problems (Bonet & Kulasegaram, (2000); Monaghan, (1988); Libersky, Randles, Carney, & Dickinson, (1997)). Libersky (L.D. Libersky, A.G. Petscheck, T.C. Carney, J.R. Hipp, 1993) were the first to employ SPH in solid mechanics (impact). Since its original version, SPH suffered from spurious instabilities and inconsistencies (Swegle, Hicks, & Attaway, (1995); Ted Belytschko, Guo, Liu, & Xiao, (2000); Xiao & Belytschko, (2005)), many improvements were proposed(T. Belytschko et al., (1996); Libersky et al., (1997); Bonet & Kulasegaram, (2000); Johnson & Beissel, (1996)). While SPH and their corrected version were based on a strong form, other methods were developed in the 90s, based on a weak form, most of them in solid mechanic applications. The element-free Galerkin (EFG) method (T. Belytschko et al., 1995) was developed in 1994 and was one of the first meshless method based on a weak global form. This method is one of the most popular meshless methods, and it was developed form the Diffuse Element Method (DEM) (Nayroles, Touzot, & Villon, 1992), which was the first method using the Moving Least Squares (MLS) (Lancaster & Salkauskas, 1981) approximants. One year later, the Reproducing Kernel Particle Method (RKPM) (W. K. Liu, Jun, & Zhang, 1995) was developed.

Another popular approximant meshfree method is the meshless local Petrov-Galerkin method (MLPG) (Atluri & Zhu, 1998) that initially was created to solve linear and nonlinear potential problems. It later evolved towards the Method of the Finite Spheres (MFS) (De & Bathe, 2000).

The Radial Function Method (RBFM) (Kansa, (1990a); Kansa, (1990b)) uses the radial basis functions, respecting an Euclidian norm, to approximate the fields within the entire domain or in small domains.

Throughout the years, many other different meshless methods using approximation shape functions, were successfully developed and applied in computational mechanics. However, some issues regarding the approximants meshless method were still not solved. One of the most relevant issues was the difficulty in imposing the boundary conditions due to the lack of the Kronecker delta function property on the approximation functions (J.Belinha, 2012).

In 2001, Liu (G. R. Liu & Gu, 2001) presented the Point Interpolation Method (PIM) and a year later, in order to avoid the singularities within this method, an improvement was proposed, including radial basis function in addition to the existing polynomial basis functions. This allowed the construction of shape functions with better performances. This new method was called the Radial Point Interpolation Method (RPIM) (J. G. Wang & Liu, 2002a).

Recently, the Natural Neighbour Radial Point Interpolation Method (NNRPIM) (J. Belinha et al., 2009) was created from the combination of the Natural Element Method (NEM) (Sukumar & Belytschko, 1998) and the RPIM.

More recently, the Natural Radial Element Method (NREM) (J. Belinha, (2013); J. Belinha, Dinis, & Natal Jorge, (2013); J. Belinha, Dinis, & Jorge, (2013); J. Belinha, Dinis, & Jorge, (2013)) was developed. The NREM is an efficient and accurate truly meshless method that presents a low order nodal connectivity.

Chapter 6

ELASTIC AND ELASTOPLASTIC ANALYSIS OF AN ALUMINIUM CELLULAR SOLID.

6.1. 2D MODELING OF THE CELLULAR SOLID

The work developed and presented herein concerns the study of the effects of the holes distribution inside a 2D square of aluminium foam. The specimen under study was a square with dimensions of [10 x 10] mm. The distribution was controlled by the equation:

$$n(R\ x\ 2) + (n)\ x\ d = 10 \tag{6.1}$$

Where n is the number of holes in the size of the specimen, d is the distance between holes, and both of them are defined by the user. Finally, the parameter R is the radius of the holes, calculated as a function of the other two variables. All of these parameters are shown clearly in Figure 44.

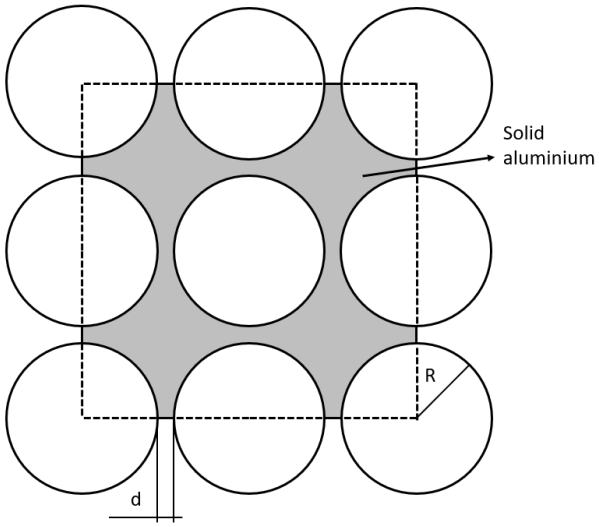

Figure 44 Aluminium cellular solid scheme

Equation (6.1) was used to calculate 16 different models as functions of variables n and d. Consider $n = [2, 3, 4, 5]$ and $d = [0.5, 1, 1.5, 2]$. The values of the radius for the different combinations of n and d are presented in Table 10. The different models that were studied are presented in more detail in ANNEX 1: Cases of the study. They are named using the value of variable '*d*', followed by the value of variable '*n*', continuum with the term '*C*' (meaning '*cheio*' in Portuguese, where the English term is '*filled*'), or '*V*' (meaning '*vazio*' in Portuguese, where the English term is '*void*').

Table 10 Circumference holes radius

		$n = 2$	$n = 3$	$n = 4$	$n = 5$
R	$d = 0.5$	2.25	1.42	1.0	0.75
R	$d = 1.0$	2.0	1.17	0.75	0.50
R	$d = 1.5$	1.75	0.92	0.50	0.25
R	$d = 2.0$	1.50	0.67	0.25	0.0

6.1.1. Material properties

The material employed in this work was aluminium 2014, which has a Young's modulus of 70000 [MPa] and a Poisson's coefficient of 0.33. These properties were applied in the solid part of the cellular solid, Figure 44; air was applied for the holes, in order to simulate an empty space for each hall.

6.1.2. Meshing procedure

In order to create the mesh, four divisions were used for $d = 0.5$ [mm] and all the remaining measures that compose the cellular solid were related to this division. At the beginning of the design process, two divisions were used for $d = 0.5$ [mm], but after obtaining the mesh, it was verified that a few of the circles were not adequately discretised. To create the mesh, the software '*FEMAP (student version)'* was employed. The elements that were applied in the mesh were 2D-T3, that means triangular elements with three nodes in the corners.

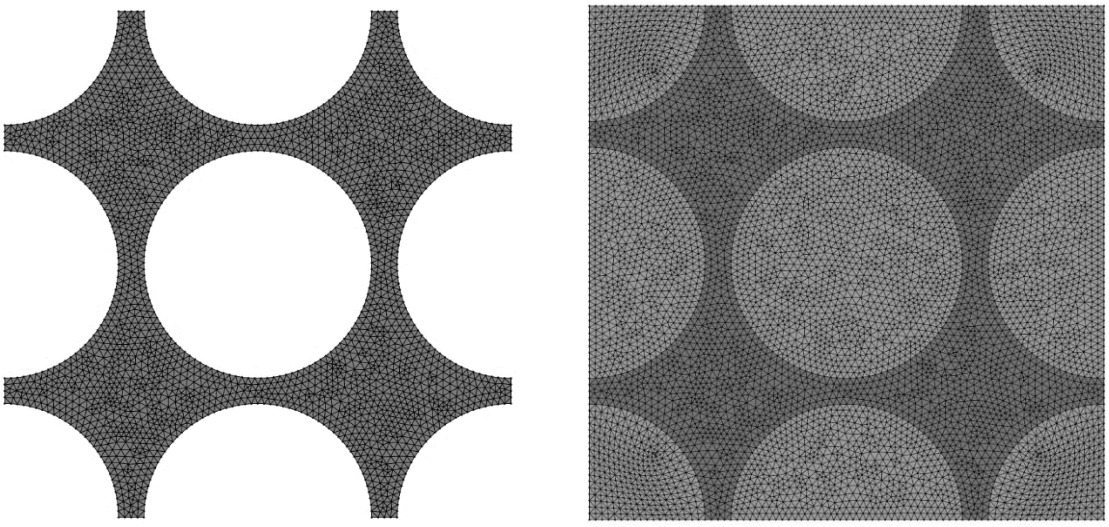

(a) (b)

Figure 45 Cellular solid (mesh) (a) n=2, d=0.5 and no meshing holes (b) n=2, d=0.5 and meshing holes.

As shown in Figure 45, two different types of situations were studied. The first situation corresponds to Figure 45 (a), where the holes were not meshing. The second situation is illustrated in Figure 45 (b), where the holes were meshing. Regarding the results, there is no difference between them, because in the case where the holes were meshing, the properties applied were those of air.

6.2. ELASTIC ANALYSIS.

The elastic analyses were carried out using the FEMAS (Finite Element and Meshless Method Analysis – cmech.webs.com) software, developed by the Professor Jorge Américo Belinha (J Belinha, 2016). For these analyses, two different situations were studied. The first one was a confined study where the lateral parts of the square were restricted in the '*x*' direction, and the base was restricted in the '*y*' direction, as seen in Figure 47(a). The second case has just a restriction of the base in the '*y*' direction allowing to expand in the '*x*' direction for both sides. See Figure 47(b).

These two situations came from the big scale specimen of a sandwich structure where the shell is considered no-confined and the core it is considered confined.

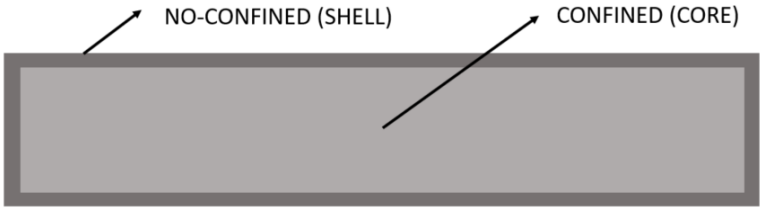

Figure 46 Scheme of a beam composed by a sandwich structure

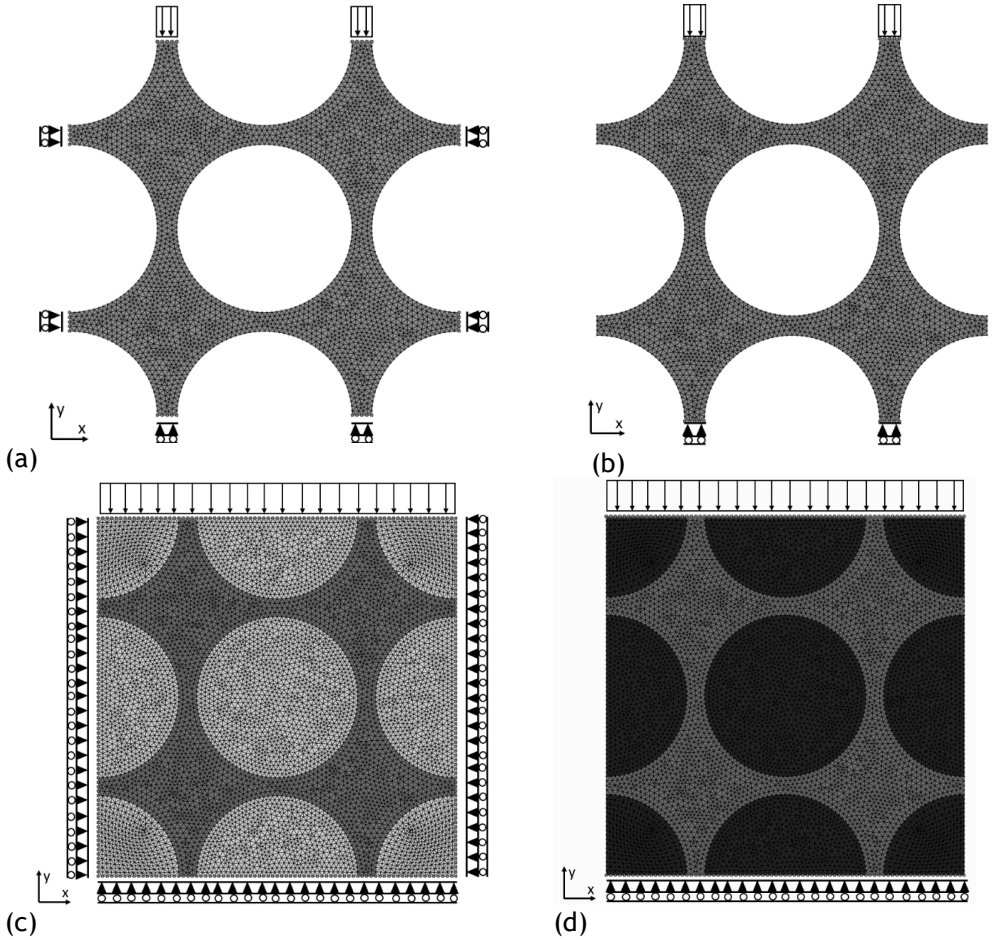

Figure 47 (a) cellular solid with no discretised holes n=2, d=0.5 and confined (b) cellular solid with no discretised holes n=2, d=0.5 and non-confined (c) cellular solid with discretised holes n=2, d=0.5 and confined (d) cellular solid with discretised holes n=2, d=0.5 and non-confined

In order to generate a stress state, an imposed displacement was applied to the top of the square with a value of 0.1% of the vertical length. This produced a 0.001 [mm] displacement in the negative '*y*' direction. These two situations were applied in both cases, where the holes are either discretised or not.

The elastic simulations were performed using the Finite Element Method (FEM) and the meshless Radial Point Interpolation Method (RPIM), for which two different types of formulations were applied. The Natural Neighbour Radial Point Interpolation Method (NNRPIM) was also used. The plane strain deformation assumption was used for every case.

After the first checking of the results, it was noticed that a few of the nodes located in the extremities of the square and the perimeter of the holes, presented residual stress concentrations that increased the difficulty of post-processing of the results. In order to solve this inconvenient, a MATLAB script was created to remove the nodes that were located in the conflict zones. This means that the cellular Young's modulus and Poisson's coefficient were calculated with the remaining nodes for each case.

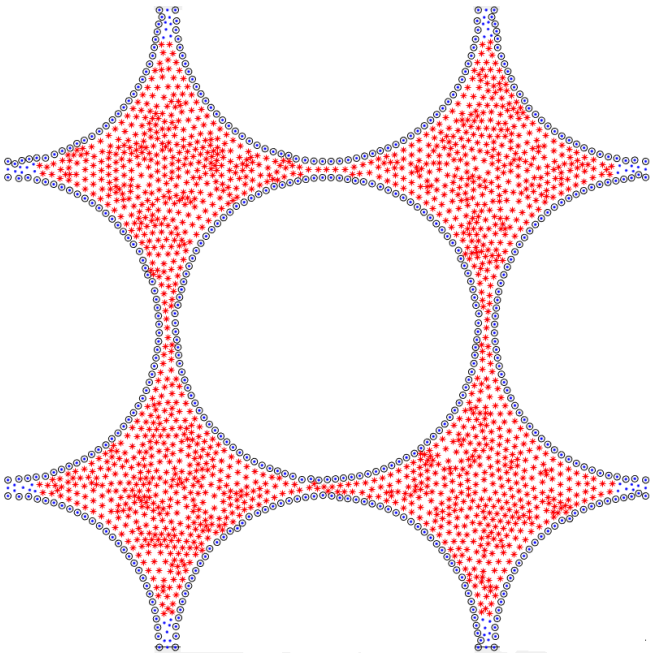

Figure 48 MATLAB elimination nodes code

As presented in Figure 48, it is possible to visualise the nodes used for calculating the parameters (red stars), all the nodes that constitute the cellular solid (blue point) and the nodes that were eliminated to avoid the residual stresses (blue circles).

6.2.1. Calculation of Young's modulus and Poisson's coefficient homogenised.

For the calculation of the Young's modulus and the Poisson's coefficient, a homogenisation technique was used. It was supported by a script in MATLAB where the stress for each node was added in a parameter called medium stress and divided by the total number of nodes experiencing stress. This calculation was done for the '*x*' and the '*y*' directions. The same technique was used to calculate the Poisson's coefficient knowing, beforehand, that it is defined by the strain in '*x*' divided by the strain in '*y*'.

Having calculated all the values for all the cases under study, the next procedure was to calculate the relative density for each situation and the respective areas of solid and holes. The following table shows all the parameters needed to accomplish this step. In order to obtain the $\frac{\rho^*}{\rho_s}$, and because it is a 2D problem, the equation applied was:

$$relative\ density = \frac{\rho^*}{\rho_s} = \frac{A_{solid}}{A_{total}} \tag{6.2}$$

where $A_{total} = 100\ mm^2$ and A_{solid} was calculated by the equation as follows:

$$A_{solid} = A_{total} - A_{holes} \tag{6.3}$$

Table 11 Parameters for the calculation of the relative density

$Radius_{holes}\ [mm]$	$Models$	n	N^oTotal_{holes}	$A_{holes}\ [mm^2]$	$A_{solid}\ [mm^2]$	ρ^*/ρ_s
2.25	0,5d_2n	2	4	63.617	36.383	0.364
1.416	0,5d_3n	3	9	56.745	43.255	0.432
1	0,5d_4n	4	16	50.265	49.734	0.497
0.75	0,5d_5n	5	25	44.178	55.821	0.558
2	1d_2n	2	4	50.265	49.734	0.497
1.166	1d_3n	3	9	38.484	61.515	0.615
0.75	1d_4n	4	16	28.274	71.726	0.717
0.5	1d_5n	5	25	19.635	80.365	0.804
1.75	1,5d_2n	2	4	38.484	61.515	0.615
0.916	1,5d_3n	3	9	23.758	76.242	0.762
0.5	1,5d_4n	4	16	12.566	87.434	0.874
0.25	1,5d_5n	5	25	4.909	95.091	0.950
1.5	2d_2n	2	4	28.274	71.725	0.717
0.666	2d_3n	3	9	12.566	87.434	0.874
0.25	2d_4n	4	16	3.142	96.858	0.968

Obtaining the values for the areas of the solid was necessary in order to correlate them with the values of the corresponding stresses.This was also done because the values given by the software referred to the total area, not just the solid part. To accomplish that, it was just a matter of simply multiplying the value obtained by the value of the solid area and dividing by the total area.

6.2.2. Variation of the properties as a function of the relative density

The next step of the study was to create the graphics that present the variation of Young's modulus and the Poisson's ratio as a function of the relative density and the comparison of the results between the different numerical formulations. The generation of the graphics was split according to the applied boundary condition and whether the hole were filled or not. In the case where the boundary conditions were confined, it was just a matter of calculating Young's modulus because it did not make sense to calculate the Poisson's ratio under this situation where the lateral expansion was restricted.

Figure 49 (a), (b) and (c) show the correlation between the numerical method in the case where the models are composed of filled holes. Figure 50 (a), (b) and (c) present the same correlation between the methods but with the models composed by empty holes.

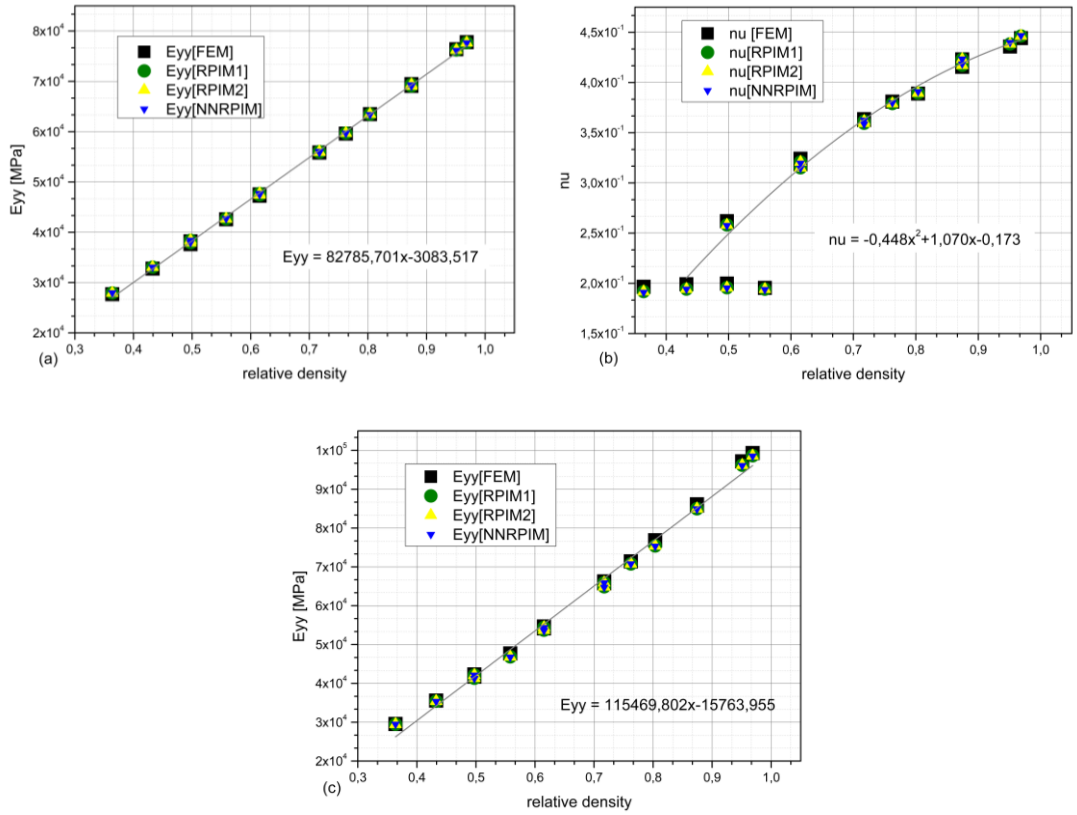

Figure 49 (a) Variation of Young's modulus as a function of the relative density for filled holes, non-confined study (b)Variation of Poisson's coefficient as a function of the relative density for filled holes, non-confined study (c) Variation of the Young's modulus as a function of the relative density for filled holes, confined study.

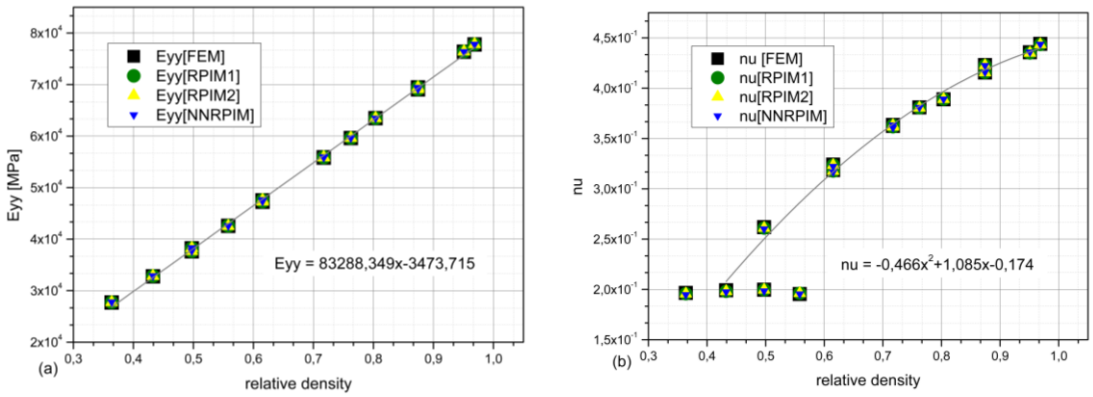

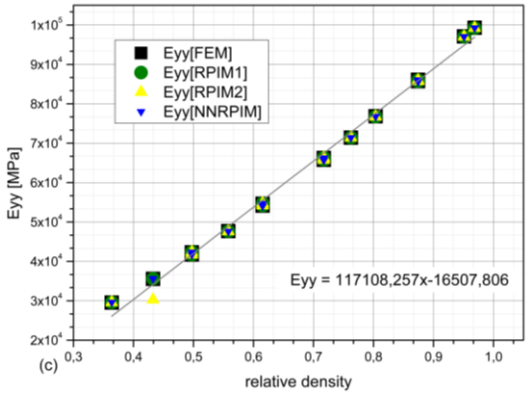

Figure 50 (a) Variation of Young's modulus as a function of the relative density for empty holes, non-confined study (b)Variation of Poisson's coefficient as a function of the relative density for empty holes, non-confined study (c) Variation of the Young's modulus as a function of the relative density for empty holes, confined study.

Through these graphics, it is possible to obtain the expression that defines the behaviour of this aluminium foam as a function of the relative density. It is important to remark that these graphics represent the elastic behaviour of the material - linear in the case of Young's modulus and quadratic for the case of the Poisson's coefficient. As mentioned previously, there are no significant differences between the results with filled and empty holes.

Another aspect that it is necessary to note is that the results obtained with the different methods (FEM, RPIM1, RPIM2, NNRPIM) present correlation values of 0.99%. These correlations values mean that the results obtained are almost the same.

6.3. ELASTOPLASTIC ANALYSIS.

6.3.1. Trial parameter

After studying the elastic behaviour of the cellular solid, the next step was to address the material behaviour zone, the elastoplastic part. In order to apply the nonlinear algorithm, it is necessarily to first define a tangential modulus and the yield strength. Table 12 shows the material parameter employed in the elastoplastic analysis. It was also necessary to define an interest point that was located in the left top part of the model, as seen Figure 51.

Table 12 Aluminium 2014 properties

Parameter	Value
Young's modulus [MPa]	70000
Tangential modulus [MPa]	2486
Poisson's coefficient	0.33
Yield strength [MPa]	399

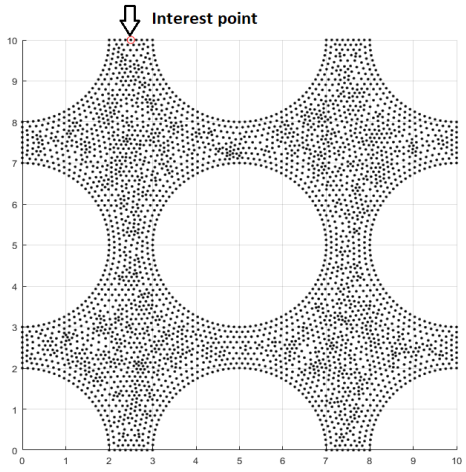

Figure 51 Location of the interest point

Though this interest point is changes its coordinates as a function of the parameter '*d*', it is the middle node in the left side of the top of the solid surface.

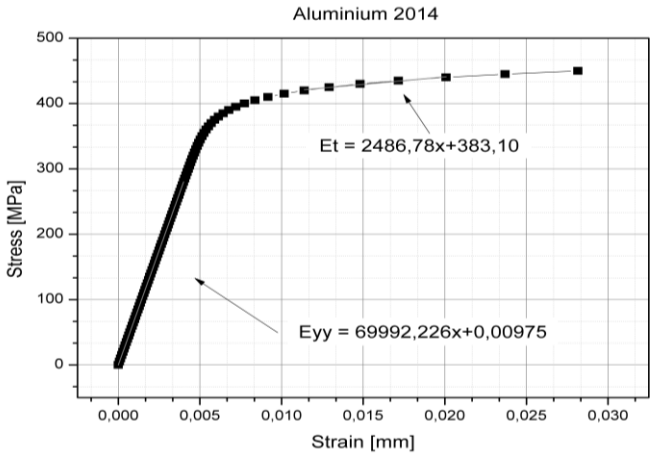

Figure 52 Strain-Stress curve for Aluminium 2014

The value of the tangential modulus was obtained through the stress-strain curve for Aluminium 2014, Figure 52, and using the Ramberg-Osgood equation:

$$\varepsilon = \frac{\sigma}{E} + 0.002\left(\frac{\sigma}{S_{ty}}\right)^{\frac{1}{n}} \tag{6.4}$$

where n is,

$$n = \frac{\log\left(S_{tu}/S_{ty}\right)}{\log\left(\varepsilon_f/0.002\right)} \tag{6.5}$$

and S_{ty} the yield strength, S_{tu} the ultimate strength and ε_f the plastic strain at failure.

For this study, a numerical approximation was applied, as mentioned in Section 4.4. In other to select the most appropriate method to approximate the elastoplastic behaviour, the first case of the model was simulated with the three-different approximated methods, KT0, KT1 and KTALL, where the elastoplastic parameters were generated by default by the FEMAS software.

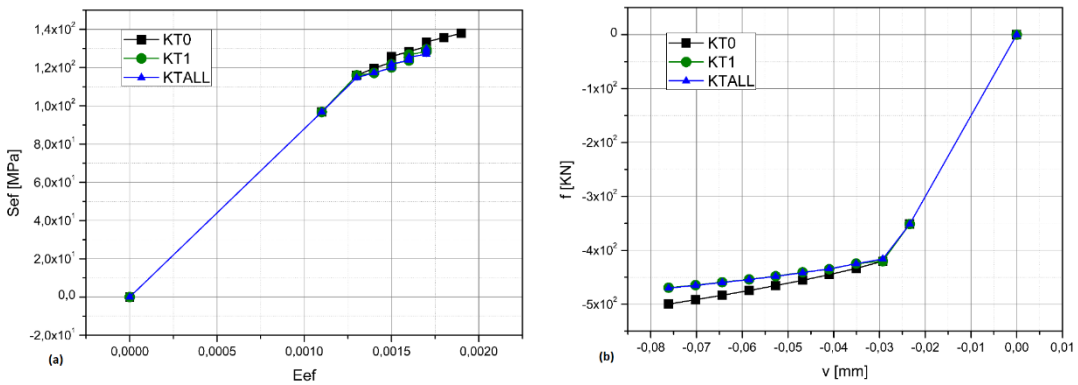

Figure 53 Comparison between the numerical elastoplastic approximation methods applied using the default parameters.

Finally, the method that was employed for all the cases was the KTALL. Then, it was necessary to fix the parameters of the non-linear solution algorithm. For this, different values were tested, for the magnitude of the applied load (with respect to the elastic limit load) imposed, ranging from 2.5 (which was the default mode) to 6 and, 16 load increments were considered. Regarding the yield criterion, it was used the von Mises yield criterium. Thus, it was necessary to employ an increment of 6 times the elastic limit, because with less than that, the approximation curve did not create a long enough plastic section from which to extract the tangential modulus. Table 13 shows all the parameters employed in the elastoplastic simulation.

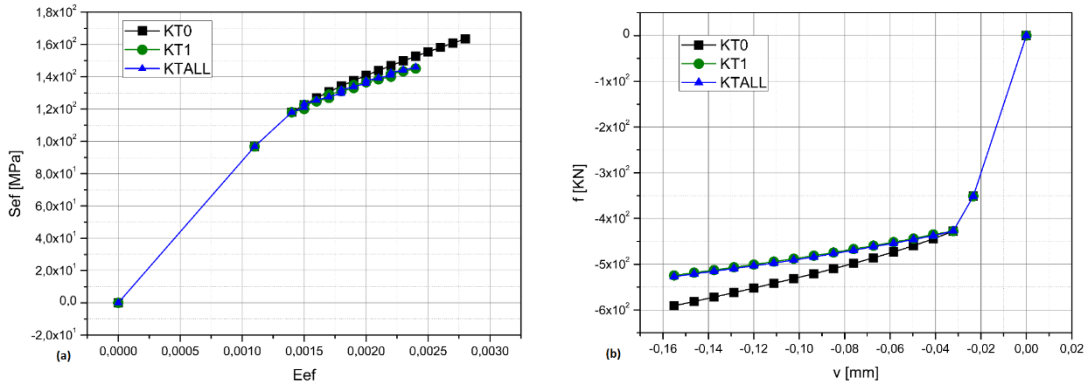

Figure 54 Comparison between the numerical elastoplastic approximation method applied using the selected parameters.

Table 13 Elastoplastic simulation parameters of FEMAS

Parameter of FEMAS	Value
Non-linear Algorithm	KTALL
Kind of imposition	Displacement
Maximum value imposed	6
Tolerance of the convergence in the iterative process	0.001
Maximum number of increments in the nonlinear analysis	16
Maximum percentage of integration points in yielding (%)	90
Yield criterion	Von-Mises
Kind of the analysis	Small-strain + Elastoplastic

6.3.2. Elastoplastic results

The values for the Young's modulus, the tangential modulus and the yield stress were obtained through the stress-strain graphic for the homogeneous case and with the force-displacement graphic in the case of the interest point. All the simulations were carried out assuming plane strain deformation theory, as the previous elastic simulation.

In the case of Young's modulus,the value of the slope was calculated in the elastic region and for the tangent modulus, the slope was calculated in the plastic region. In the case of the

yield stress, it meant finding and selecting the point where the curve changes from the elastic to the plastic region. Equations (5.6) and (5.7) show the parameters applied.

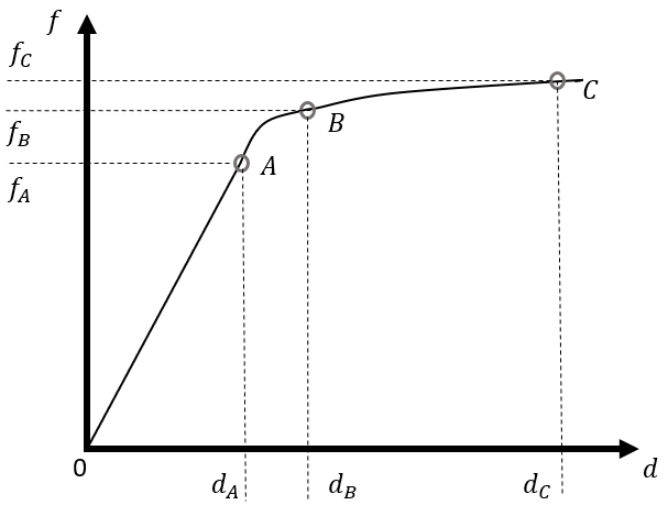

Figure 55 Scheme force-displacement graphic

$$E = \frac{\frac{(f_A - f_0)}{A} = \sigma_A}{\frac{(d_A - d_0)}{L} = \varepsilon_A} \tag{6.6}$$

$$E_T = \frac{\frac{(f_c - f_B)}{A} = \sigma_C - \sigma_B}{\frac{(d_C - d_B)}{L} = \varepsilon_C - \varepsilon_B} \tag{6.7}$$

where $A = 10\ mm^2$ and $L = 10\ mm$.

In total, 120 elastoplastic simulations were performed in order to visualise the difference between the cases and to better understand how the elastic modulus and the tangent modulus behave with the variation of the relative density. It also allowed to analyse the difference in the results obtained through the use of the different numerical methods. Each simulation produced, the graphics of effective stress versus effective strain, homogenised, and the force-displacement graphics, both in the '*y*' direction, with regards to the interest point.

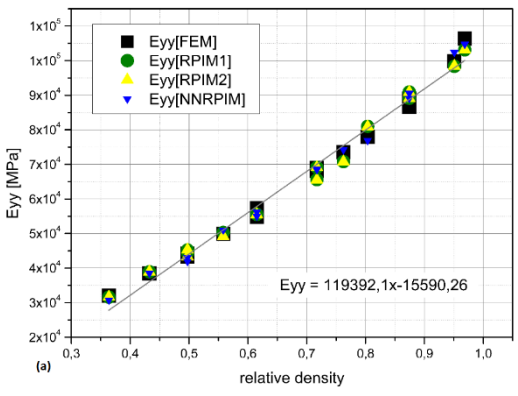

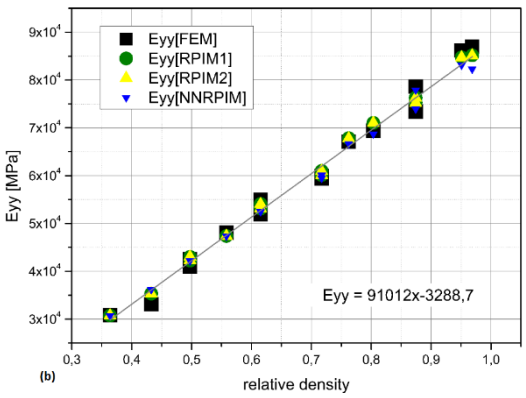

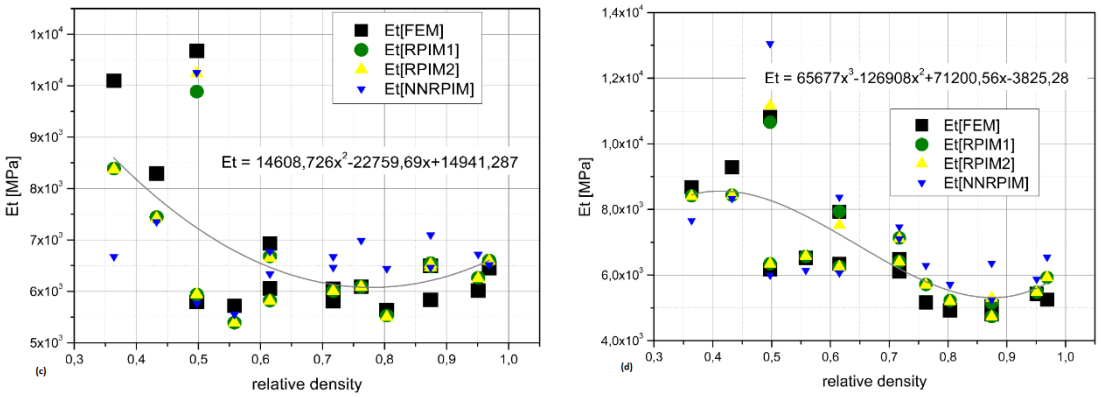

Figure 56 (a) Variation of the homogenous elastic modulus in the confined elastoplastic analyses (b) Variation of the homogenous elastic modulus in the non-confined elastoplastic analyses (c) Variation of the homogenous tangent modulus in the confined elastoplastic analyses (d) Variation of the homogenous tangent modulus in the non-confined elastoplastic analyses.

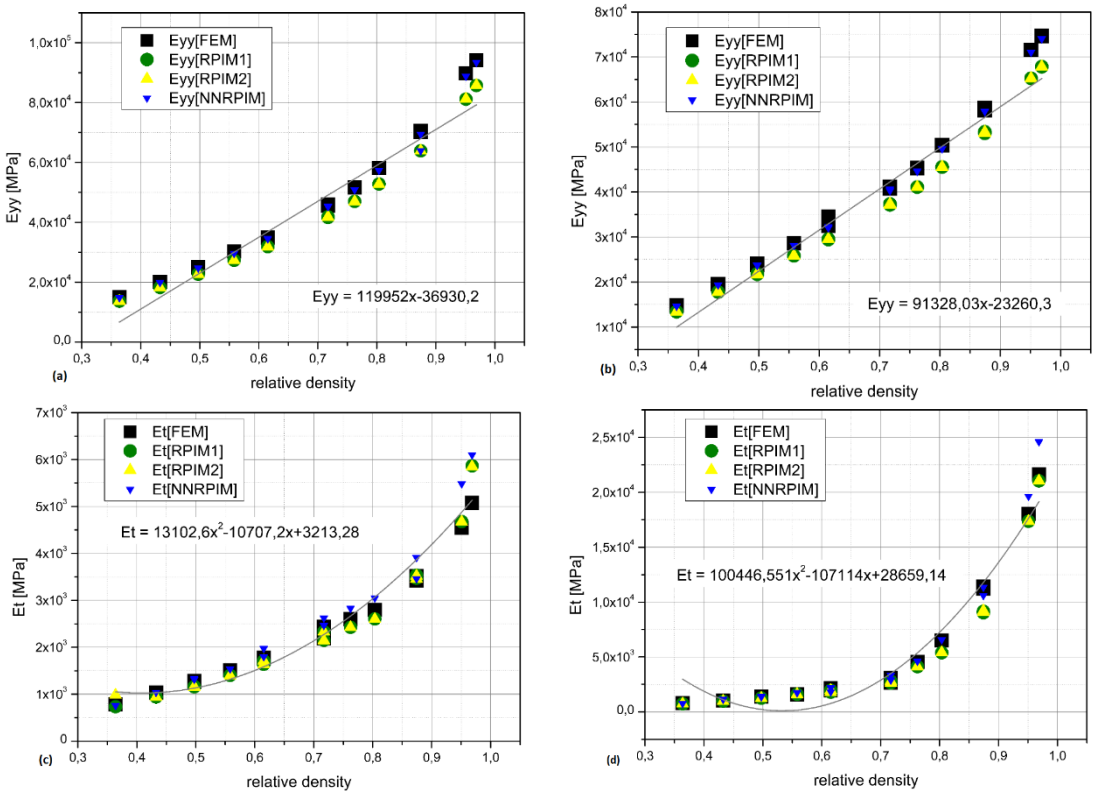

Figure 57 (a) Variation of the elastic modulus (interest point) in the confined elastoplastic analyses (b) Variation of the elastic modulus (interest point) in the non-confined elastoplastic analyses (c) Variation of the tangent modulus (interest point) in the confined elastoplastic analyses (d) Variation of the tangent modulus (interest point) in the non-confined elastoplastic analyses.

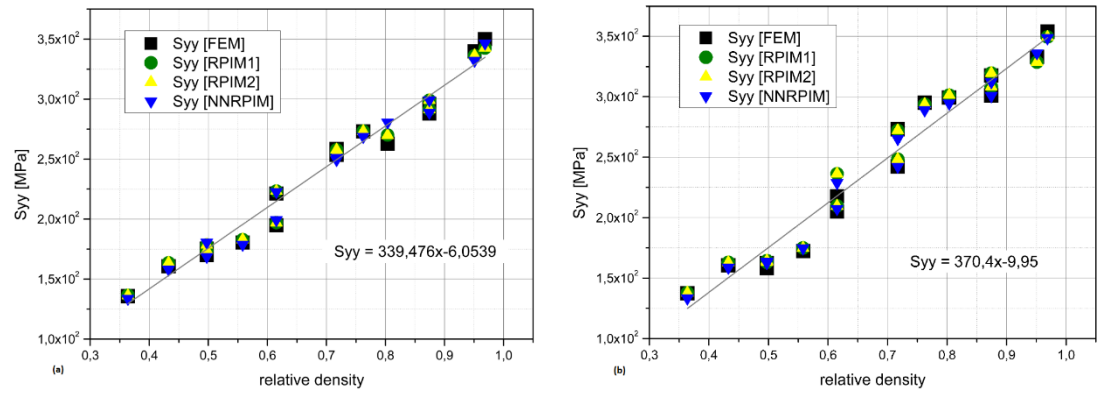

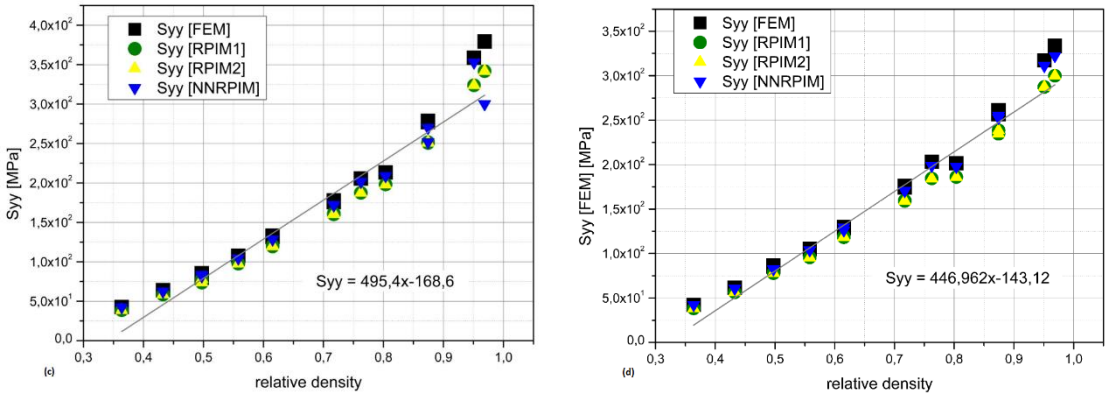

Figure 58 (a) Variation of the homogenous yield stress in the confined elastoplastic analyses (b) Variation of the homogenous yield stress in the non-confined elastoplastic analyses (c) Variation of the yield stress in the interest point and the confined elastoplastic analyses (d) Variation of the yield stress modulus in the interest point, and the non-confined elastoplastic analyses.

Through elastoplastic graphics presented above, it is possible to observe that the results in all the cases exhibit a growth trend when the relative density increases. The expression that defines Young's modulus is linear, and the ones that define the tangente modulus are quadratic, except for the homogenous tangent modulus for the non-confined case (Figure 56d), which is third order.

As for the elastic study, the correlation between the different numerical methods used (FEM, RPIM1, RPIM2, NNRPIM) is concentrated between 0.97%-0.99%, with the exception of the case of homogenous tangent modulus for the confined case (Figure 56c), which is lower.

Regarding the normal behaviour of the tangential modulus, it was expected that the value would increase with the increase of the relative density, but in the case of the homogeneous technique, the behaviour is decreasing, as observed in Figure 56 (c) and (d). However, the behaviour obtained around the interest point for the tangential modulus is incremental with increasing relative density, as expected and presented in Figure 57 (c) and (d). Because of this unexpected behaviour, it was decided to compare the results of the studies with respect to the properties obtained by the homogenisation technique and the ones obtained in the interest point. The discussion is presented in the next section.

Chapter 7

CANTILEVER BEAM COMPOSED BY ALUMINIUM FOAM.

This section presents the analysis of the behavior of a 2D cantilever beam composed of an aluminium solid shell and an homogenous core with different foams of relative densities of 0.4, 0.5, 0.6 and 0.7. Secondly, the beam will be composed of a progressive core where the relative density is going to increase from the centre to the outer part of the beam. These two configurations are shown in Figure 59 (a) and (b) and both of them were simulated in the program *'FEMAP student version'*.

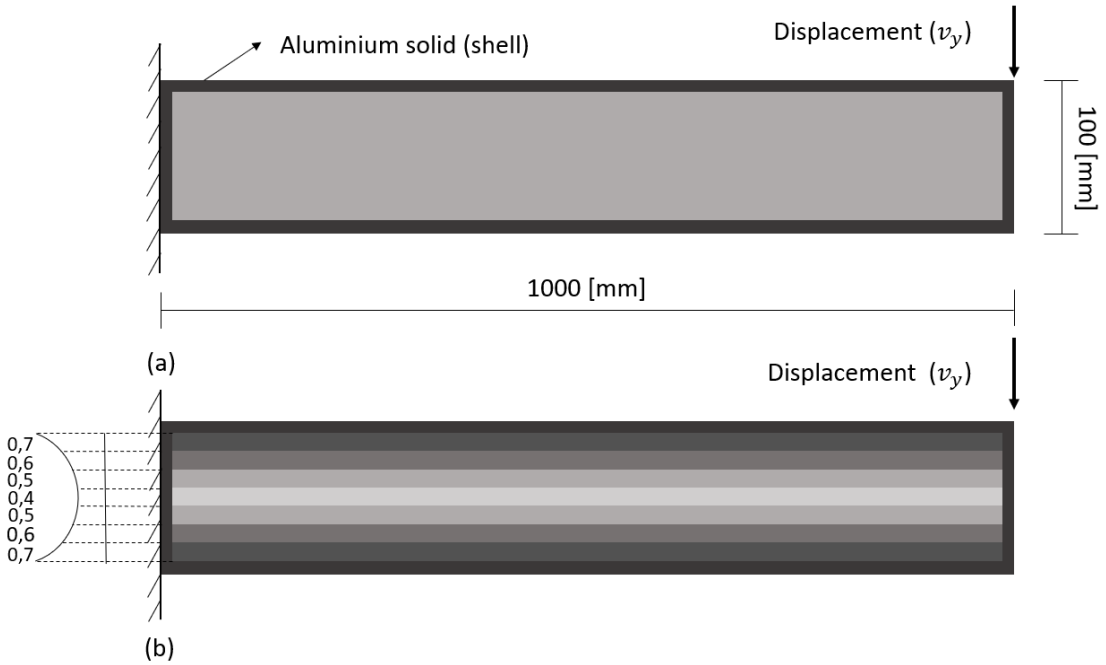

Figure 59 (a) Scheme of the cantilever beam with a homogenous aluminium foam core and a solid aluminium shell (b) Scheme of the cantilever beam with the different layers corresponding to the different values of the relative densities of the aluminium foam.

The displacement v_y is 10 [mm], the shell layer has 10 [mm] of thickness around the foam core, and in the case of the progressive foam core, each layer has 11.43 [mm] of thickness.

7.1. ELASTOPLASTIC ANALYSIS.

The elastoplastic analysis was carried out with the objective to obtain the force-displacement graphic for each case and compare the results between the numerical formulation employed using the FEM, RPIM1, RPIM2, NNRPIM, previously explained in Chapter

5. The aim was also to compare the results obtained via the homogenisation technique and with the values from the interesting point.

The force-displacement graphics were built for each increment of the elastoplastic study, employing a vertical reaction force and a vertical displacement of the node with coordinates [x=1000mm, y=100mm]. This means the displacement was apllied at the node .

For the elastoplastic analysis, the the conditions applied are presented in Table 14. Plane strain assumptions were considered.

Table 14 Elastoplastic simulation FEMAS parameter for the cantilever beam case

Parameter of FEMAS	Value
Non-linear Algorithm	KTALL
Kind of imposition	Displacement
Maximum value imposed	4
Tolerance of the convergence in the iterative process	0.001
Maximum number of increments in the nonlinear analysis	15
Maximum percentage of integration points in yielding (%)	90
Yield criterion	Von-Mises
Kind of the analysis	Small-strain + Elastoplastic

Table 15 Homogenised mechanical properties

Homogenised				
$\boldsymbol{\rho^*/\rho_s}$	$\boldsymbol{S_{yy}}$ $[MPa]$	$\boldsymbol{E}$ $[MPa]$	$\boldsymbol{E_T}$ $[MPa]$	$\boldsymbol{v}$
0.4	129.7365	30335.4968	8174.80716	0.18544
0.5	163.6841	42046.3225	7213.6235	0.252
0.6	197.6317	53757.1482	6544.61436	0.30924
0.7	231.5793	65467.9739	6167.77974	0.35716

Table 16 Interest point mechanical properties

Interest Point				
$\boldsymbol{\rho^*/\rho_s}$	$\boldsymbol{S_{yy}}$ $[MPa]$	$\boldsymbol{E}$ $[MPa]$	$\boldsymbol{E_T}$ $[MPa]$	$\boldsymbol{v}$
0.4	29.56	11050.8	1026.816	0.18544
0.5	79.1	23046.05	1135.33	0.252
0.6	128.64	35041.3	1505.896	0.30924
0.7	178.18	47036.55	2138.514	0.35716

The values of the properties for each relative density were obtained using the equation that defines the behaviour of the properties obtained in Section 5.3.2 for homogenised results and the interest point. These properties are shown in Table 15 and Table 16. It is remarkable how the values of the interest point are considerably lower than the ones obtained with the

homogenisation technique, which means that it is expected that the homogenised results correlate to a more stiff behaviour than for the interest point.

Homogenised | Interest Point

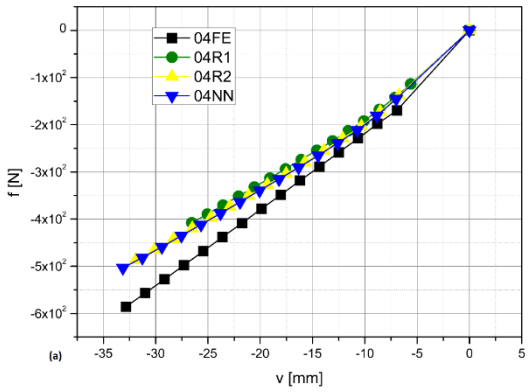

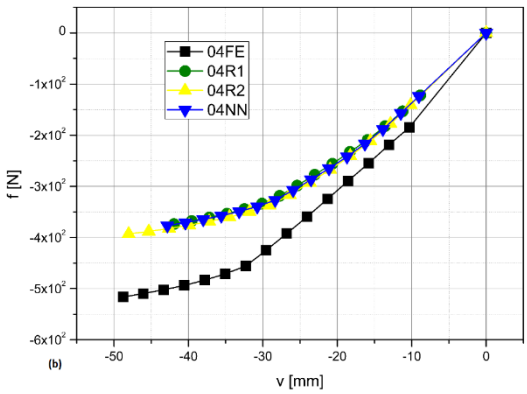

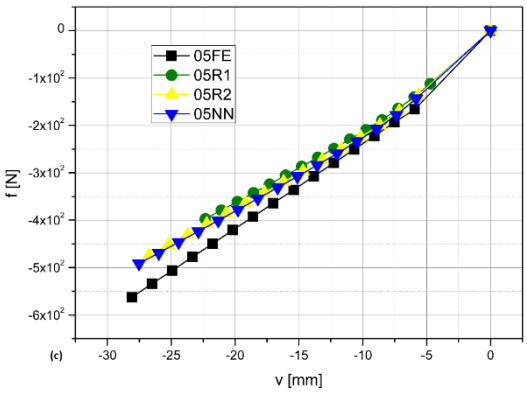

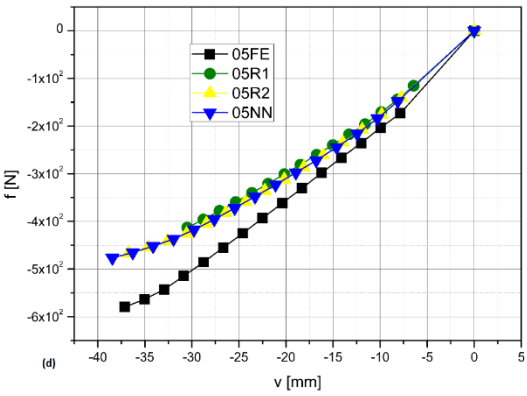

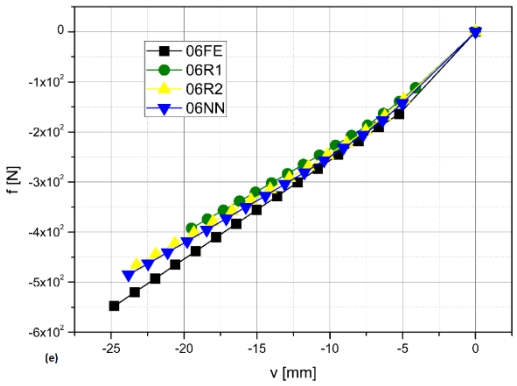

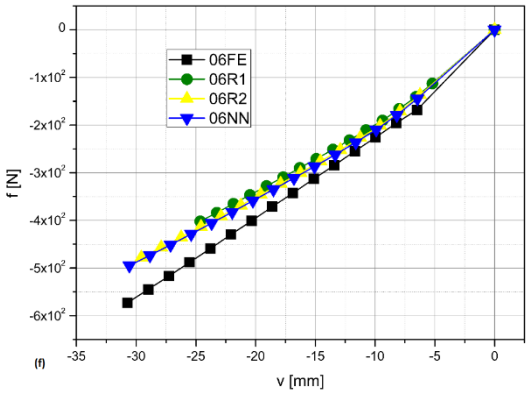

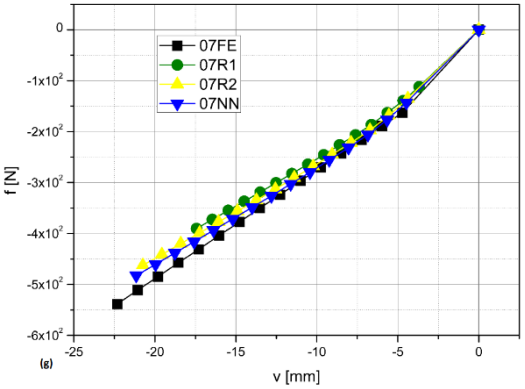

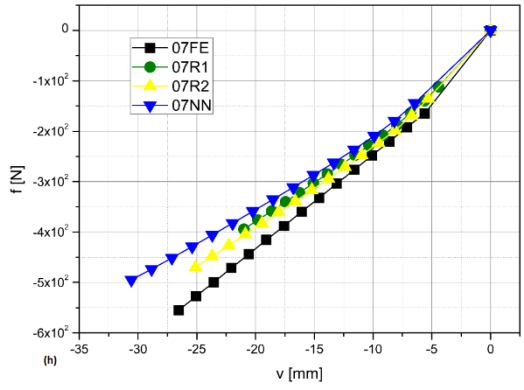

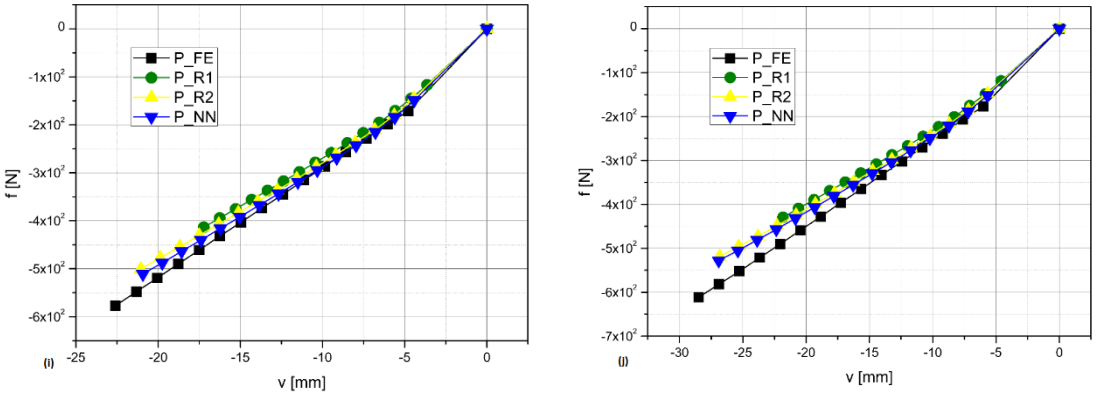

Figure 60 (a) force-displacement 0.4 relative density (homogenised) (b) force-displacement 0.4 relative density (interest point) (c) force-displacement 0.5 relative density (homogenised) (d) force-displacement 0.5 relative density (interest point) (e) force-displacement 0.6 relative density (homogenised) (f) force-displacement 0.6 relative density (interest point) (g) force-displacement 0.7 relative density (homogenised) (h) force-displacement 0.7 relative density (interest point) (i) force-displacement progressive relative density (homogenised) (j) force-displacement progressive relative density (interest point).

Regarding the graphics, it is possible to observe how the value of the displacement decreases with the increase of the relative density. This means that the stiffness of the foam beam core increases with the relative density and, as expected, the homogenised case presents a greater stiffness than the interest point, but without a considerable difference between them. Another aspect is the shape of the graphics that, in the case of the homogenous system, shows values that are similar. Conversely, in the case of of the interest point, the shape of the graphics change with the relative density, exhibiting a greater curvature. Taking into account the comparison between the methods, it is remarkable that in both the homogenised and the interest point cases, the methods do not produce the same values at the last displacement point. Focusing om the homogeneous case, the methods that produces the maximum values is the FEM, then the RPIM with the second formulation and with NNRPIM, and finally the lower value is obtained via the RPIM with the first formulation. Otherwise, in the case of the interest point, the values of the last displacement point change with the relative density and with the method for all the cases.

To represent with more precision, the behaviour of the cantilever beam in ANNEXE 2 is going to be represented the graphics behaviour of the elastoplastic results for the homogeneous and the interest point cases, increasing the maximum value imposed from four to eight and increasing the number of increments from 15 to 20. Also, it is going to be represented the behaviour of the beam for each numerical method applied, increasing the relative density.

Chapter 8

CONCLUSIONS

Now, it is possible to identify a few points that are important for future actions. Starting with the first objective, that it was to determine the behaviour of an aluminium foam with a controlled relative density. This was desired in order latter to apply this knowledge to different situations and for larger scales. Specifcally for this work,, the goal was to apply these properties on a cantilever beam, for which there are some critical situations that need to be studied deeper before completely defining the behaviour of an aluminium foam. One of these situations is the region of relative density lower than 0.4, where the properties are not entirely defined with the studies that were carried out in this project. Also,the same concern is valid in the case of the relative densities higher than 0.7, where Young's modulus present values 15% higher than the proper solid with relative density 1.

Another noteworthy aspect is the behaviour presented in the tangent modulus for the homogeneous case, which was not expected, exhibiting a decreasing behaviour with the increase of the relative density. Conversely, the interest point simulation produced a response of the tangent modulus demonstrated to grow with the relative density. At this point and when comparing the results obtained for the homogeneous and the interest point cases, it appears the latter produces better results. In view of these results, it was concluded that the homogenisation technique requires further study and verification as to gain a further understanding with respect to the diffrence in the results.

The work also compared each result and graphic in terms of the four different numerical methods applied. In the case of the elastic analyses, the results are almost the same as mentioned in section 6.2. However, the elastoplastic analyses produced a few curious situations, where the results obtained using the FEM and the NNRPIM were practically the same between them. Also,the results obtained using the RPIM with the first and the second formulations, were also the same between them. It is curious because a difference was expected, since FEM is a mesh-based method while the remaining RPIM and NNRPIM are meshless

In the case of the elastoplastic analysis using the cantilever beam, the similarity between meshless methods was more pronounced in the case with lower relative densities and more similar with the FEM result with higher relative densities.

This work presented herein corresponds to a total of 400 simulations carried out under various conditions: 340 for the elastic analyses, 120 for the elastoplastic and finally, 40 for the study of the cantilever beam. This means that, in order to understand the behaviour for a cellular solid with the same internal pattern and by just varying its relative density, it becomes necessary to produce much information and long computational times. At this point in time, when the additive manufacturing technologies allow to create bigger scale prototypes with controlled cellular structures and controlled relative densities, it is exciting to reflect on the possibilities and potential for being more ambitious, for building new internal structures, for combining materials and so on.

8.1. FURTHER IMPROVEMENTS

One of the situations that could be studied in the future is how the behaviour of the stress lines inside the cellular solid changes with the increase or decrease of the relative density. The reason behind this recommendation, it was clearly shown that stress lines present a period and symmetric form inside the cellular solid and with a similar shape as the honeycomb structure. It would be interesting to investigate whether the honeycomb structure came from the shape of the stress lines in a cellular solid.

Another aspect that would be interesting to solve is to find out why the properties obtained through the homogenisation technique produce, at a relative density of 0.8 and higher, a Young's modulus with upper values than the properties of the aluminium solid. Also, it would be important to understand the reasons for the behaviour of the tangent modulus for the case of the homogenous values.

Finally, it would be interesting to replicate the work presented, applying the same processs and methodologies, but using different materials. It would be interesting to study the behaviour and how the results are affected, namely changes to the internal structure when the same load and density variations are applied.

References

A. Hrennikoff. (1941). *Solution of Problems of Elasticity by the Frame-Work Method*. Retrieved from https://en.wikipedia.org/wiki/Alexander_Hrennikoff

Abrate, S. (2008). Criteria for Yielding or Failure of Cellular Materials. *Journal of Sandwich Structures & Materials*, *10*(1), 5–51. https://doi.org/10.1177/1099636207070997

Abueidda, D. W., Abu Al-Rub, R. K., Dalaq, A. S., Lee, D. W., Khan, K. A., & Jasiuk, I. (2016). Effective conductivities and elastic moduli of novel foams with triply periodic minimal surfaces. *Mechanics of Materials*, *95*, 102–115. https://doi.org/10.1016/j.mechmat.2016.01.004

Allen, H. G. (Howard G. (1969). Analysis and design of structural sandwich panels, 283.

Aluru, N. R. (2000). A Point Collocation Method Based on the Differential Kernel Approximations, (2000), 70101–70101.

Arns, C. H., Knackstedt, M. A., Pinczewski, W. V., & Garboczi, E. J. (2002). Computation of linear elastic properties from microtomographic images: Methodology and agreement between theory and experiment. *Geophysics*, *67*(5), 1396–1405. https://doi.org/10.1190/1.1512785

Atluri, S. N., & Zhu, T. (1998). A new Meshless Local Petrov-Galerkin (MLPG) approach in computational mechanics. *Computational Mechanics*, *22*(2), 117–127. https://doi.org/10.1007/s004660050346

Augustin, C., & Hungerbach, W. (2009). Production of hollow spheres (HS) and hollow sphere structures (HSS). *Materials Letters*, *63*(13–14), 1109–1112. https://doi.org/10.1016/j.matlet.2009.01.015

B.G.Galerkin. (1915). Galerkin.pdf. *Vestinik Inzhenerov i Tekhnikocv*, *19*, 897–908.

Barbier, C., Dendievel, R., & Rodney, D. (2009). Numerical study of 3D-compressions of entangled materials. *Computational Materials Science*, *45*(3), 593–596. https://doi.org/10.1016/j.commatsci.2008.06.003

Bathe, K. J., & Saunders, H. (1984). Finite Element Procedures in Engineering Analysis. *Journal of Pressure Vessel Technology*. https://doi.org/10.1115/1.3264375

Belinha, J. (2014a). *Meshless Methods in Biomechanics*. Springer. https://doi.org/10.1007/978-94-007-4174-4

Belinha, J. (2014b). *Meshless Methods in Biomechanics Bone Tissue Remodelling Analysis*. https://doi.org/10.1007/978-94-007-4174-4

Belinha, J. (2016). Manual Femas, 1–83.

Belinha, J. A. (2004a). Analise Elasto-Plastica Considerando o Metodo Livre de Elementos de Galerkin.

Belinha, J. A. (2004b). Análise Elasto-Plástica Considerando o Método Livre de Elementos de Galerkin.

Belinha, J., Dinis, L. M. J. S., & Jorge, R. M. N. (2009). The natural neighbour radial point interpolation method: dynamic applications. *Engineering Computations*, *26*(8), 911–949. https://doi.org/10.1108/02644400910996835

Belinha, J., Dinis, L. M. J. S., & Jorge, R. M. N. (2013). Composite laminated plate analysis using the natural radial element method. *Composite Structures*, *103*, 50–67. https://doi.org/10.1016/j.compstruct.2013.03.018

Belinha, J., Dinis, L. M. J. S., & Natal Jorge, R. M. (2013). Analysis of thick plates by the natural radial element method. *International Journal of Mechanical Sciences*, *76*, 33–48. https://doi.org/10.1016/j.ijmecsci.2013.08.011

Belytschko, T., Guo, Y., Liu, W. K., & Xiao, S. P. (2000). A unifieded stability analysis of meshless particle methods. *International Journal for Numerical Methods in Engineering*, *48*(9), 1359–1400. https://doi.org/10.1002/1097-0207(20000730)48:9<1359::AID-NME829>3.0.CO;2-U

Belytschko, T., Krongauz, Y., Organ, D., Fleming, M., & Krysl, P. (1996). Meshless methods: An overview and recent developments. *Computer Methods in Applied Mechanics and*

Engineering, *139*(1–4), 3–47. https://doi.org/10.1016/S0045-7825(96)01078-X
Belytschko, T., Lu, Y. Y., & Gu, L. (1994). Element-free Galerkin methods. *International Journal for Numerical Methods in Engineering*, *37*(2), 229–256. https://doi.org/10.1002/nme.1620370205
Belytschko, T., Lu, Y. Y., Gu, L., & Tabbara, M. (1995). Element-free galerkin methods for static and dynamic fracture. *International Journal of Solids and Structures*, *32*(17–18), 2547–2570. https://doi.org/10.1016/0020-7683(94)00282-2
Berre, C., Fok, S. L., Mummery, P. M., Ali, J., Marsden, B. J., Marrow, T. J., & Neighbour, G. B. (2008). Failure analysis of the effects of porosity in thermally oxidised nuclear graphite using finite element modelling. *Journal of Nuclear Materials*, *381*(1–2), 1–8. https://doi.org/10.1016/j.jnucmat.2008.07.021
Bikard, J., Bruchon, J., Coupez, T., & Vergnes, B. (2005). Numerical prediction of the foam structure of polymeric materials by direct 3D simulation of their expansion by chemical reaction based on a multidomain method. *Journal of Materials Science*, *40*(22), 5875–5881. https://doi.org/10.1007/s10853-005-5022-9
Böhm, H. J., Pahr, D. H., & Daxner, T. (2010). Analytical and Numerical Methods for Modeling the Thermomechanical and Thermophysical Behavior of Microstructured Materials. In V. V Silberschmidt (Ed.), *Computational and Experimental Mechanics of Advanced Materials* (pp. 167–223). Vienna: Springer Vienna. https://doi.org/10.1007/978-3-211-99685-0_5
Bonet, J., & Kulasegaram, S. (2000). Correction and stabilization of smooth particle hydrodynamics methods with applications in metal forming simulations. *International Journal for Numerical Methods in Engineering*, *47*(6), 1189–1214. https://doi.org/10.1002/(SICI)1097-0207(20000228)47:6<1189::AID-NME830>3.0.CO;2-I
Boomsma, K., Poulikakos, D., & Ventikos, Y. (2003). Simulations of flow through open cell metal foams using an idealized periodic cell structure. *International Journal of Heat and Fluid Flow*, *24*(6), 825–834. https://doi.org/10.1016/j.ijheatfluidflow.2003.08.002
Brakke, K. A. (1992). The Surface Evolver. *Experimental Mathematics*, *1*(2), 141–165. https://doi.org/10.1080/10586458.1992.10504253
Bridgman, P. W. (1947). The effect of hydrostatic pressure on the fracture of brittle substances. *Journal of Applied Physics*, *18*(2), 246–258. https://doi.org/10.1063/1.1697610
Budiansky, B., & Kimmel, E. (1987). Elastic Moduli of Lungs. *Journal of Applied Mechanics*, *54*(2), 351. https://doi.org/10.1115/1.3173019
Buffel, B., Desplentere, F., Bracke, K., & Verpoest, I. (2014). Modelling open cell-foams based on the Weaire-Phelan unit cell with a minimal surface energy approach. *International Journal of Solids and Structures*, *51*(19–20), 3461–3470. https://doi.org/10.1016/j.ijsolstr.2014.06.017
Capaldi, F. M. (2012). *Continuum Mechanics: Constitutive Modeling of Structural and Biological Materials*.
Caty, O., Maire, E., Youssef, S., & Bouchet, R. (2008). Modeling the properties of closed-cell cellular materials from tomography images using finite shell elements. *Acta Materialia*, *56*(19), 5524–5534. https://doi.org/10.1016/j.actamat.2008.07.023
Chen, J.-S., Hillman, M., & Chi, S.-W. (2017). Meshfree Methods: Progress Made after 20 Years. *Journal of Engineering Mechanics*, *143*(4), 04017001. https://doi.org/10.1061/(ASCE)EM.1943-7889.0001176
Chen, J., Wu, C., & Yoon, S. (2001). A stabilized conforming nodal integration for Galerkin mesh-free methods. *Int. J. Numer. Meth. Eng*, *0207*(February 2000), 435–466. https://doi.org/10.1002/1097-0207(20010120)50
Cheng, A. H., & Cheng, D. T. (2005). Heritage and early history of the boundary element method, *m*, 268–302. https://doi.org/10.1016/j.enganabound.2004.12.001
Choi, J. B., & Lakes, R. (1992). Non-linear properties of metallic cellular materials with a negative Poisson's ratio. *Journal of Materials Science*, *27*(19), 5375–5381. https://doi.org/10.1007/BF00553421
Choi, J. B., & Lakes, R. S. (1995). Analysis of elastic modulus of conventional foams and of re-entrant foam materials with a negative Poisson's ratio. *International Journal of Mechanical Sciences*, *37*(1), 51–59. https://doi.org/10.1016/0020-7403(94)00047-N
Christensen, R. M. (1996). On the relationship of minimal conditions to low density material microstructures. *Journal of the Mechanics and Physics of Solids*, *44*(12), 2113–2123. https://doi.org/10.1016/S0022-5096(96)00063-4

Christensen, R. M. (1998). Two Theoretical Elasticity Micromechanics Models. *Journal of Elasticity*, *50*, 15–25. https://doi.org/10.1023/A:1007497600857

Christensen, R. M. (2000). Mechanics of cellular and other low-density materials. *International Journal of Solids and Structures*, *37*(1–2), 93–104. https://doi.org/10.1016/S0020-7683(99)00080-3

Clough, R. W. (1956). JOURNAL OF THE AERONAUTICAL SCIENCES Turbulence in Supersonic Flow *. *J. Aeronaut. Sci.*, *23*(9), 657–674,682.

Crisfield, M. a M. a., Jiang, X., Chen, H., Liew, J. Y. R., de Borst, R., Remmers, J. J. C., & Verhoosel, C. V. (2000). Non-linear finite element analysis of solids and structures, Volume 1. *East*, *1*, 193–212. https://doi.org/10.1017/CBO9781107415324.004

Czekanski, A., Attia, M. S., Meguid, S. A., & Elbestawi, M. A. (2005). On the use of a new cell to model geometric asymmetry of metallic foams. *Finite Elements in Analysis and Design*, *41*(13), 1327–1340. https://doi.org/10.1016/j.finel.2004.12.012

Czekanski, A., Elbestawi, M. A., & Meguid, S. A. (2005). On the FE modeling of closed-cell aluminum foam. *International Journal of Mechanics and Materials in Design*, *2*(1–2), 23–34. https://doi.org/10.1007/s10999-005-0518-7

D. Weaire and R. Phelan. (1994). A new counter-example to Kelvin's conjecture on minimal surfaces. *Philosophical Magazine Letters*, *69*(2), 107–110. https://doi.org/10.1080/09500830903022651

Daxner, T., Bitsche, R. D., & Böhm, H. J. (2006). Space-Filling Polyhedra as Mechanical Models for Solidified Dry Foams. *Materials Transactions*, *47*(9), 2213–2218. https://doi.org/10.2320/matertrans.47.2213

De, S., & Bathe, K. J. (2000). The method of finite spheres. *Computational Mechanics*, *25*(4), 329–345. https://doi.org/10.1007/s004660050481

Deshpande, V. S., & Fleck, N. A. (2000). Isotropic constitutive models for metallic foams. *Journal of the Mechanics and Physics of Solids*, *48*(6), 1253–1283. https://doi.org/10.1016/S0022-5096(99)00082-4

Deshpande, V. S., & Fleck, N. A. (2001). Multi-axial yield behaviour of polymer foams. *Acta Materialia*, *49*(10), 1859–1866. https://doi.org/10.1016/S1359-6454(01)00058-1

Dinis, L. M. J. S., Natal Jorge, R. M., & Belinha, J. (2007). Analysis of 3D solids using the natural neighbour radial point interpolation method. *Computer Methods in Applied Mechanics and Engineering*, *196*(13–16), 2009–2028. https://doi.org/10.1016/j.cma.2006.11.002

Drucker, D. C., & Prager, W. (1952). Soil mechanics and plastic analysis or limit design. *Quarterly of Applied Mathematics*, *10*(2), 157–165. https://doi.org/10.1090/qam/48291

Duchon, J. (1977). Splines minimizing rotation-invariant semi-norms in Sobolev spaces. In W. Schempp & K. Zeller (Eds.), *Constructive Theory of Functions of Several Variables* (pp. 85–100). Berlin, Heidelberg: Springer Berlin Heidelberg.

Eaton, A. (2005). *Finite Element Approximation*. https://doi.org/10.1007/978-3-540-85268-1_3

Elliott, J. A., & Windle, A. H. (2002). In-situ deformation of an open-cell flexible polyurethane foam characterised by 3D computed microtomography.pdf, *7*, 1547–1555.

Elmer, W., Chen, J. S., Puso, M., & Taciroglu, E. (2012). A stable, meshfree, nodal integration method for nearly incompressible solids. *Finite Elements in Analysis and Design*, *51*, 81–85. https://doi.org/10.1016/j.finel.2011.11.001

EMMANUEL E. GDOUTOS. (2013). *Recent Advances in Experimental Mechanics* (Vol. 53). https://doi.org/10.1017/CBO9781107415324.004

Escoda, J., Willot, F., Jeulin, D., Sanahuja, J., & Toulemonde, C. (2016). Influence of the multiscale distribution of particles on elastic properties of concrete. *International Journal of Engineering Science*, *98*, 60–71. https://doi.org/10.1016/j.ijengsci.2015.07.010

Evans, A. G., Hutchinson, J. W., & Ashby, M. F. (1998). Cellular metals. *Current Opinion in Solid State and Materials Science*, *3*(3), 288–303. https://doi.org/10.1016/S1359-0286(98)80105-8

Evans, A. G., Hutchinson, J. W., & Ashby, M. F. (1998). Multifunctionality of cellular metal systems. *Progress in Materials Science*, *43*(3), 171–221. https://doi.org/10.1016/S0079-6425(98)00004-8

Fiedler, T., Hosseini, S. M. H., Belova, I. V., Murch, G. E., & Öchsner, A. (2009). A refined finite element analysis on the thermal conductivity of perforated hollow sphere structures.

Computational Materials Science, *47*(2), 314–319. https://doi.org/10.1016/j.commatsci.2009.08.007

Fischer, F., Lim, G. T., Handge, U. A., & Altstädt, V. (2009). Numerical simulation of mechanical properties of cellular materials using computed tomography analysis. *Journal of Cellular Plastics*, *45*(5), 441–460. https://doi.org/10.1177/0021955X09339340

Gan, Y. X., Chen, C., & Shen, Y. P. (2005). Three-dimensional modeling of the mechanical property of linearly elastic open cell foams. *International Journal of Solids and Structures*, *42*(26), 6628–6642. https://doi.org/10.1016/j.ijsolstr.2005.03.002

Garboczi, E. J., & Day, A. R. (1995). An algorithm for computing the effective linear elastic properties of heterogeneous materials: Three-dimensional results for composites with equal phase poisson ratios. *Journal of the Mechanics and Physics of Solids*, *43*(9), 1349–1362. https://doi.org/10.1016/0022-5096(95)00050-S

Gdoutos, E. E., Daniel, I. M., & Wang, K. A. (2002). Failure of cellular foams under multiaxial loading. *Composites - Part A: Applied Science and Manufacturing*, *33*(2), 163–176. https://doi.org/10.1016/S1359-835X(01)00110-5

Gent, A. N., & Thomas, A. G. (1959). The deformation of foamed elastic materials. *Journal of Applied Polymer Science*, *1*(1), 107–113. https://doi.org/10.1002/app.1959.070010117

Gibson, L. J., Ashby, M. F. and Triantafillou, T. C. (1989). Failure surfaces for cellular materials under multixial loads - I. Modelling. *Int. J. Mech. Sci.*, *31*(9), 635–663.

Gibson, L., & Ashby, M. (1997). *[Lorna_J._Gibson,_Michael_F._Ashby]_Cellular_Solid Structure and Properties - Second edition*.

Gibson, L. J. (1989). Modelling the mechanical behavior of cellular materials. *Materials Science and Engineering: A*, *110*, 1–36. https://doi.org/10.1016/0921-5093(89)90154-8

Gibson, L. J. (2005). Biomechanics of cellular solids. *Journal of Biomechanics*, *38*(3), 377–399. https://doi.org/10.1016/j.jbiomech.2004.09.027

Gibson, L. J., & Ashby, M. F. (1982). The Mechanics of Three-Dimensional Cellular Materials. *Proceedings of the Royal Society A: Mathematical, Physical and Engineering Sciences*, *382*(1782), 43–59. https://doi.org/10.1098/rspa.1982.0088

Gibson, L. J., & Ashby, M. F. (1982). The Mechanics of Three-Dimensional Cellular Materials. *Proceedings of the Royal Society of London A: Mathematical, Physical and Engineering Sciences*, *382*(1782), 43–59. https://doi.org/10.1098/rspa.1982.0088

Gibson, L. J., & Ashby, M. F. (1989). Cellular Solids: Structure & Properties. *Advances in Polymer Technology*, *9*(2), 165–166. https://doi.org/10.1046/j.1365-2850.1998.00130.x

Gioux, G., McCormack, T. M., & Gibson, L. J. (2000). Failure of aluminum foams under multiaxial loads. *International Journal of Mechanical Sciences*, *42*(6), 1097–1117. https://doi.org/10.1016/S0020-7403(99)00043-0

Golberg, M. a., Chen, C. S., & Bowman, H. (1999). Some recent results and proposals for the use of radial basis functions in the BEM. *Engineering Analysis with Boundary Elements*, *23*(4), 285–296. https://doi.org/10.1016/S0955-7997(98)00087-3

Gong, L., & Kyriakides, S. (2006). On the Crushing Stress of Open Cell Foams. *Journal of Applied Mechanics*, *73*(5), 807. https://doi.org/10.1115/1.2047608

Grenestedt, J. L. (1998). Influence of wavy imperfections in cell walls on elastic stiffness of cellular solids. *Journal of the Mechanics and Physics of Solids*, *46*(1), 29–50. https://doi.org/10.1016/S0022-5096(97)00035-5

Guest, J. K., & Prévost, J. H. (2006). Optimizing multifunctional materials: Design of microstructures for maximized stiffness and fluid permeability. *International Journal of Solids and Structures*, *43*(22–23), 7028–7047. https://doi.org/10.1016/j.ijsolstr.2006.03.001

Guest, J. K., & Prévost, J. H. (2007). Design of maximum permeability material structures. *Computer Methods in Applied Mechanics and Engineering*, *196*(4–6), 1006–1017. https://doi.org/10.1016/j.cma.2006.08.006

Hashin, Z. (1983). Analysis of Composite Materials—A Survey. *Journal of Applied Mechanics*, *50*(3), 481–505. Retrieved from http://dx.doi.org/10.1115/1.3167081

Hill, R. (1950). The Mathematical Theory of Plasticity. *Oxford University Press Ic., New York*, 62. https://doi.org/10.1002/9780470694626.ch6

J._S._Przemieniecki. (1967). *Theory of Matrix Structural*. London: McGraw-Hill.

J. Belinha, L. M. J. S. D. and R. M. N. J. (2013). The natural radial element method. *International Journal for Numerical Methods in Engineering*, *93*(January), 1286–1313.

https://doi.org/10.1002/nme
Jang, W. Y., Kraynik, A. M., & Kyriakides, S. (2008). On the microstructure of open-cell foams and its effect on elastic properties. *International Journal of Solids and Structures*, *45*(7–8), 1845–1875. https://doi.org/10.1016/j.ijsolstr.2007.10.008
Jang, W. Y., & Kyriakides, S. (2009). On the crushing of aluminum open-cell foams: Part II analysis. *International Journal of Solids and Structures*, *46*(3–4), 635–650. https://doi.org/10.1016/j.ijsolstr.2008.10.016
Jeon, I., Katou, K., Sonoda, T., Asahina, T., & Kang, K. J. (2009). Cell wall mechanical properties of closed-cell Al foam. *Mechanics of Materials*, *41*(1), 60–73. https://doi.org/10.1016/j.mechmat.2008.08.002
Jirásek, M., & Bazant, Z. P. (2002). *Inelastic analysis of structures*.
Joachim L. Grenestedt, & Tanaka, K. (1999). INFLUENCE OF CELL SHAPE VARIATIONS ON ELASTIC STIFFNESS OF CLOSED CELL CELLULAR SOLIDS. *International Journal of Mechanical Sciences*, *40*(1), 71–77.
Johnson, G. R., & Beissel, S. R. (1996). Normalized smoothing functions for sph impact computations. *International Journal for Numerical Methods in Engineering*, *39*(16), 2725–2741. https://doi.org/10.1002/(SICI)1097-0207(19960830)39:16<2725::AID-NME973>3.0.CO;2-9
Kansa, E. J. (1990a). Multiquadrics-A scattered data approximation scheme with applications to computational fluid-dynamics-I surface approximations and partial derivative estimates. *Computers and Mathematics with Applications*, *19*(8–9), 127–145. https://doi.org/10.1016/0898-1221(90)90270-T
Kansa, E. J. (1990b). Multiquadrics-A scattered data approximation scheme with applications to computational fluid-dynamics-II solutions to parabolic, hyperbolic and elliptic partial differential equations. *Computers and Mathematics with Applications*, *19*(8–9), 147–161. https://doi.org/10.1016/0898-1221(90)90271-K
Kapfer, S. C., Hyde, S. T., Mecke, K., Arns, C. H., & Schr??der-Turk, G. E. (2011). Minimal surface scaffold designs for tissue engineering. *Biomaterials*, *32*(29), 6875–6882. https://doi.org/10.1016/j.biomaterials.2011.06.012
Khaderi, S. N., Deshpande, V. S., & Fleck, N. A. (2014). The stiffness and strength of the gyroid lattice. *International Journal of Solids and Structures*, *51*(23–24), 3866–3877. https://doi.org/10.1016/j.ijsolstr.2014.06.024
Kim, A., Tunvir, K., Jeong, G. D., & Cheon, S. S. (2006). A multi-cell FE-model for compressive behaviour analysis of heterogeneous Al-alloy foam. *Modelling and Simulation in Materials Science and Engineering*, *14*(6), 933–945. https://doi.org/10.1088/0965-0393/14/6/004
Kinney, J. H., & Ladd, A. J. C. (1998). The Relationship Between Three-Dimensional Connectivity and the Elastic Properties of Trabecular Bone. *Journal of Bone and Mineral Research*, *13*(5), 839–845. https://doi.org/10.1359/jbmr.1998.13.5.839
Kirca, M., Gül, A., Ekinci, E., Yardim, F., & Mugan, A. (2007). Computational modeling of micro-cellular carbon foams. *Finite Elements in Analysis and Design*, *44*(1–2), 45–52. https://doi.org/10.1016/j.finel.2007.08.008
Ko, W. L. (1965). Deformations of Foamed Elastomers. *Journal of Cellular Plastics*, *1*(1), 45–50. https://doi.org/10.1177/0021955X6500100107
Körner, C. (2008). Foam formation mechanisms in particle suspensions applied to metal foams. *Materials Science and Engineering A*, *495*(1–2), 227–235. https://doi.org/10.1016/j.msea.2007.09.089
Kou, D. P., Li, J. R., Yu, J. L., & Cheng, H. F. (2008). Mechanical behavior of open-cell metallic foams with dual-size cellular structure. *Scripta Materialia*, *59*(5), 483–486. https://doi.org/10.1016/j.scriptamat.2008.04.022
Kraynik, a M., & Warren, W. E. (1994). The elastic behavior of low-density cellular plastics. *Low Density Cellular Plastics*, 187–225. https://doi.org/10.1007/978-94-011-1256-7_7
Kraynik, A. M. (1998). FOAM MICROMECHANICS.
Krysl, P., & Belytschko, T. (1999). The element free Galerkin method for dynamic propagation of arbitrary 3-D cracks. *International Journal for Numerical Methods in Engineering*, *44*(6), 767–800. https://doi.org/10.1002/(SICI)1097-0207(19990228)44:6<767::AID-NME524>3.0.CO;2-G
L. B. Lucÿ. (1977). A numerical approach to the testing of the fission hypothesis L., *82*(12), 1013–1024.

L.D. Libersky, A.G. Petscheck, T.C. Carney, J.R. Hipp, F. A. A. (1993). High Strain Lagrangian Hydrodynamics: a three-dimensional SPH code for Dynamic Material Response, *109*, 67–75.

Lancaster, P., & Salkauskas, K. (1981). Surfaces generated by moving least squares methods. *Mathematics of Computation*, *37*(155), 141–141. https://doi.org/10.1090/S0025-5718-1981-0616367-1

"Lecture 5: Rate Independent Plasticity," in ANSYS Mechanical Structural Nonlinearities 13.0 ed. ANSYS Customer Training Material. (2010), 47. Retrieved from http://anibal.gyte.edu.tr/hebe/abldrive/68431132/w/storage/101_2011_1_321_68431132/downloads/week-4.pdf

Lee, M. G., Lee, J. W., Han, S. C., & Kang, K. (2016). Mechanical analyses of "shellular", an ultralow-density material. *Acta Materialia*, *103*, 595–607. https://doi.org/10.1016/j.actamat.2015.10.040

Lee, W., Kang, D.-Y., Song, J., Moon, J. H., & Kim, D. (2016). Controlled Unusual Stiffness of Mechanical Metamaterials. *Scientific Reports*, *6*(1), 20312. https://doi.org/10.1038/srep20312

Li, K., Gao, X. L., & Subhash, G. (2006). Effects of cell shape and strut cross-sectional area variations on the elastic properties of three-dimensional open-cell foams. *Journal of the Mechanics and Physics of Solids*, *54*(4), 783–806. https://doi.org/10.1016/j.jmps.2005.10.007

Li, L., & Bettess, P. (1997). Adaptive Finite Element Methods: A Review. *Applied Mechanics Reviews*, *50*(10), 581. https://doi.org/10.1115/1.3101670

Libersky, L. D., Randles, P. W., Carney, T. C., & Dickinson, D. L. (1997). Recent improvements in SPH modeling of hypervelocity impact. *International Journal of Impact Engineering*, *20*(6–10), 525–532. https://doi.org/10.1016/S0734-743X(97)87441-6

Liu, G. R. (2003). *Mesh free method: moving beyond the finite element method*.

Liu, G. R., & Gu, Y. T. (2001). A local radial point interpolation method (LRPIM) for free vibration analyses of 2-D solids. *Journal of Sound and Vibration*, *246*(1), 29–46. https://doi.org/10.1006/jsvi.2000.3626

Liu, G. R., & Quek, S. (2003). The finite element method: a practical course, 433. Retrieved from http://books.google.com/books?hl=en&lr=&id=_xbugmEwQz8C&oi=fnd&pg=PR9&dq=The+finite+element+method+a+practical+course&ots=mYrSYjZtYF&sig=cq-J04WtkYL7NaK4z2EUz1EvJD4

Liu, W. K., & Chen, Y. (1995). Wavelet and multiple scale reproducing kernel methods. *International Journal for Numerical Methods in Fluids*, *21*(10), 901–931. https://doi.org/10.1002/fld.1650211010

Liu, W. K., Jun, S., & Zhang, Y. F. (1995). Reproducing kernel particle methods. *International Journal for Numerical Methods in Fluids*, *20*(8–9), 1081–1106. https://doi.org/10.1002/fld.1650200824

Lubliner, J., & Moran, B. (1992). Plasticity Theory. *Journal of Applied Mechanics*, *59*(1), 245. https://doi.org/10.1115/1.2899459

M.F. Ashby, A.G. Evans, N.A. Fleck, L.J. Gibson, J. W. H. and H. N. G. W. (n.d.). Metal Foams : A Design Guide Metal Foams : A Design Guide.

M.Naghdi, P. (2013). *Theoretical,Experimental and Numerical contributions to the mechanics of fluids and solids*. *Journal of Chemical Information and Modeling* (Vol. 53). https://doi.org/10.1017/CBO9781107415324.004

Maire, E., Fazekas, A., Salvo, L., Dendievel, R., Youssef, S., Cloetens, P., & Letang, J. M. (2003). X-ray tomography applied to the characterization of cellular materials. Related finite element modeling problems. *Composites Science and Technology*, *63*(16), 2431–2443. https://doi.org/10.1016/S0266-3538(03)00276-8

Marcadon, V., Davoine, C., Passilly, B., Boivin, D., Popoff, F., Rafray, A., & Kruch, S. (2012). Mechanical behaviour of hollow-tube stackings: Experimental characterization and modelling of the role of their constitutive material behaviour. *Acta Materialia*, *60*(15), 5626–5644. https://doi.org/10.1016/j.actamat.2012.06.045

Maxwell, J. C., & (Plateau). (1874). On Soap Bubbles. *Nature*, *X*(252), 119. Retrieved from http://books.google.com/books?hl=en&lr=&id=s4c77H5ThCgC&oi=fnd&pg=PA251&dq=On+Soap-Bubbles&ots=vD-zeSI4aM&sig=Ido41H7L-

yPZSLF-i_ZFf7dcDCM%5Cnhttp://books.google.com/books?hl=en&lr=&id=s4c77H5ThCgC&oi=fnd&pg=PA25
Meguid, S. A., Cheon, S. S., & El-Abbasi, N. (2002). FE modelling of deformation localization in metallic foams. *Finite Elements in Analysis and Design*, *38*(7), 631–643. https://doi.org/10.1016/S0168-874X(01)00096-8
Miller, R. E. (2000). Continuum plasticity model for the constitutive and indentation behaviour of foamed metals. *International Journal of Mechanical Sciences*, *42*(4), 729–754. https://doi.org/10.1016/S0020-7403(99)00021-1
Mills, N. J. (2005). The wet Kelvin model for air flow through open-cell polyurethane foams. *Journal of Materials Science*, *40*(22), 5845–5851. https://doi.org/10.1007/s10853-005-5018-5
Mills, N. J., Stämpfli, R., Marone, F., & Brühwiler, P. A. (2009). Finite element micromechanics model of impact compression of closed-cell polymer foams. *International Journal of Solids and Structures*, *46*(3–4), 677–697. https://doi.org/10.1016/j.ijsolstr.2008.09.012
Monaghan, J. J. (1988). An introduction to SPH. *Computer Physics Communications*, *48*(1), 89–96. https://doi.org/10.1016/0010-4655(88)90026-4
Moreira, S. F. (2013). Elastoplastic analysis using the Natural Neighbour Radial Point Interpolation Method by, (July).
Nayroles, B., Touzot, G., & Villon, P. (1992). Generalizing the finite element method: Diffuse approximation and diffuse elements. *Computational Mechanics*, *10*(5), 307–318. https://doi.org/10.1007/BF00364252
Nguyen, B. D., Cho, J. S., & Kang, K. (2016). Optimal design of "Shellular", a micro-architectured material with ultralow density. *Materials and Design*, *95*, 490–500. https://doi.org/10.1016/j.matdes.2016.01.126
Nguyen, V. P., Rabczuk, T., Bordas, S., & Duflot, M. (2008). Meshless methods: A review and computer implementation aspects. *Mathematics and Computers in Simulation*, *79*(3), 763–813. https://doi.org/10.1016/j.matcom.2008.01.003
Nuscholtz, G., Bilkhu, M., Founas, M., & Du Bois, P. (1996). A simple elastoplastic model for foam materials. In *STAP conference, Alberquerque*.
Oñate, E., Idelsohn, S., Zienkiewicz, O. C., & Taylor, R. L. (1996). A finite point method in computational mechanics. Applications to convective transport and fluid flow. *International Journal for Numerical Methods in Engineering*, *39*(22), 3839–3866. https://doi.org/10.1002/(SICI)1097-0207(19961130)39:22<3839::AID-NME27>3.0.CO;2-R
Oñate, E., Perazzo, F., & Miquel, J. (2001). A finite point method for elasticity problems. *Computers and Structures*, *79*(22–25), 2151–2163. https://doi.org/10.1016/S0045-7949(01)00067-0
Overaker, D. D. W., Cuitino, A. M., & Langrana, N. A. (1998). Effects of morphology and orientation on the behavior of two-dimensional hexagonal foams and application in a re-entrant foam anchor model. *Mechanics of Materials*, *29*(1), 43–52. https://doi.org/10.1016/S0167-6636(98)00004-0
Owen, D. R. J., & Hinton, E. (1980). Finite elements plasticity: Theory and Practice, 603.
Papka, S. D., & Kyriakides, S. (1998). Biaxial crushing of honeycombs*Part I: Experiments. *International Journal of Solids and Structures*, 4367–4396. https://doi.org/10.1016/S0020-7683(98)00224-8
Patarata, V. S. (2017). Structural simulation of 3D limb prostheses using meshless methods, (September).
Penrose, R. (1979). Pentaplexity A Class of Non-Periodic Tilings of the Plane. *The Mathematical Intelligencer*, *2*(1), 32–37. https://doi.org/10.1007/BF03024384
R. A. Gingold and J. J. Monaghan. (1977). Smoothed particle hydrodynamics: theory and application to non-spherical stars, *181*, 375–389.
Raghava, R., Caddell, R. M., & Yeh, G. S. Y. (1973). The macroscopic yield behaviour of polymers. *Journal of Materials Science*, *8*(2), 225–232. https://doi.org/10.1007/BF00550671
Richard M. Christensen. (1993). Effective properties of composite materials containing voidst. *Mathematical and Physical Sciences*, *440*, 461–473. https://doi.org/10.1098/rspa.1993.0027
Roberts, A. P., & Garboczi, E. J. (2001). Elastic Moduli of Model Random Three- Dimensional

Closed-Cell Cellular Solids. *Acta Mater*, *49*(2), 189–197. https://doi.org/http://dx.doi.org/10.1016/S1359-6454(00)00314-1

Saadatfar, M., Arns, C. H., Knackstedt, M. A., & Senden, T. (2005). Mechanical and transport properties of polymeric foams derived from 3D images. *Colloids and Surfaces A: Physicochemical and Engineering Aspects*, *263*(1–3 SPEC. ISS.), 284–289. https://doi.org/10.1016/j.colsurfa.2004.12.040

Salvo, L., Suéry, M., Marmottant, A., Limodin, N., & Bernard, D. (2010). 3D imaging in material science: Application of X-ray tomography. *Comptes Rendus Physique*, *11*(9–10), 641–649. https://doi.org/10.1016/j.crhy.2010.12.003

Sandino, C., Planell, J. A., & Lacroix, D. (2008). A finite element study of mechanical stimuli in scaffolds for bone tissue engineering. *Journal of Biomechanics*, *41*(5), 1005–1014. https://doi.org/10.1016/j.jbiomech.2007.12.011

Santosa, S., & Wierzbicki, T. (1998). On the modeling of crush behavior of a closed-cell aluminum foam structure. *Journal of the Mechanics and Physics of Solids*, *46*(4), 645–669. https://doi.org/10.1016/S0022-5096(97)00082-3

Scherer, G. W., Smith, D. M., & Stein, D. (1995). Deformation of aerogels during characterization. *Journal of Non-Crystalline Solids*, *186*, 309–315. https://doi.org/10.1016/0022-3093(95)00058-5

Shafiq, M., Ayyagari, R. S., Ehaab, M., & Vural, M. (2015). Multiaxial yield surface of transversely isotropic foams: Part I - Experimental. *Journal of the Mechanics and Physics of Solids*, *76*, 224–236. https://doi.org/10.1016/j.jmps.2014.10.009

Shulmeister, V., Van Der Burg, M. W. D., Van Der Giessen, E., & Marissen, R. (1998). A numerical study of large deformations of low-density elastomeric open-cell foams. *Mechanics of Materials*, *30*(2), 125–140. https://doi.org/10.1016/S0167-6636(98)00033-7

Sihn, S., & Roy, A. K. (2004). Modeling and prediction of bulk properties of open-cell carbon foam. *Journal of the Mechanics and Physics of Solids*, *52*(1), 167–191. https://doi.org/10.1016/S0022-5096(03)00072-3

Simone, A. E., & Gibson, L. J. (1998). The effects of cell face curvature and corrugations on the stiffness and strength of metallic foams. *Acta Materialia*, *46*(11), 3929–3935. https://doi.org/10.1016/S1359-6454(98)00072-X

Souza Neto, E. de, Peric, D., & Owen, D. R. J. (2008). *Computational Methods for Plasticity*. *Computational methods for plasticity-theory and applications* (Vol. 55). https://doi.org/10.1002/9780470694626

Stock, S. R. (2008). Recent advances in X-ray microtomography applied to materials. *International Materials Reviews*, *53*(3), 129–181. https://doi.org/10.1179/174328008X277803

Sugimura, Y., Rabiei, a, Evans, a. ., Harte, a. ., & Fleck, N. . (1999). Compression fatigue of a cellular Al alloy. *Materials Science and Engineering: A*, *269*(1–2), 38–48. https://doi.org/10.1016/S0921-5093(99)00147-1

Sukumar, N., & Belytschko, T. (1998). The natural element method in solid mechanics. *International Journal for Numerical Methods in Engineering*, *43*(5), 839–887. https://doi.org/10.1002/(SICI)1097-0207(19981115)43:5<839::AID-NME423>3.0.CO;2-R

Swegle, J. W., Hicks, D. L., & Attaway, S. W. (1995). Smoothed Particle Hydrodynamics Stability Analysis. *Journal of Computational Physics*, *116*(1), 123–134. https://doi.org/10.1006/jcph.1995.1010

Tagarielli, V. L., Deshpande, V. S., Fleck, N. A., & Chen, C. (2005). A constitutive model for transversely isotropic foams, and its application to the indentation of balsa wood. *International Journal of Mechanical Sciences*, *47*(4–5 SPEC. ISS.), 666–686. https://doi.org/10.1016/j.ijmecsci.2004.11.010

Thomson, W. (2008). On the division of space with minimum partitional area. *Philosophical Magazine Letters*, *88*(2), 103–114. https://doi.org/10.1080/09500830701698298

Torquato, S. (2005). Microstructure Optimization. *Handbook of Materials Modeling*, 2379–2396. https://doi.org/10.1007/978-1-4020-3286-8_124

Torquato, S., Gibiansky, L. V., Silva, M. J., & Gibson, L. J. (1998). Effective mechanical and transport properties of cellular solids. *International Journal of Mechanical Sciences*, *40*(1), 71–82. https://doi.org/10.1016/S0020-7403(97)00031-3

Torquato, S., Hyun, S., & Donev, A. (2002). Multifunctional Composites: Optimizing Microstructures for Simultaneous Transport of Heat and Electricity. *Physical Review*

Letters, *89*(26), 266601. https://doi.org/10.1103/PhysRevLett.89.266601
Tsai, S. W., & wu, E. M. (1971). A General Theory of Strength for Anisotropic Materials. *Journal of Composite Materials*, *5*(1), 58–80. https://doi.org/10.1177/002199837100500106
Ulrich, D., Van Rietbergen, B., Weinans, H., & Rüegsegger, P. (1998). Finite element analysis of trabecular bone structure: A comparison of image-based meshing techniques. *Journal of Biomechanics*, *31*(12), 1187–1192. https://doi.org/10.1016/S0021-9290(98)00118-3
Vesenjak, M., Veyhl, C., & Fiedler, T. (2012). Analysis of anisotropy and strain rate sensitivity of open-cell metal foam. *Materials Science and Engineering A*, *541*, 105–109. https://doi.org/10.1016/j.msea.2012.02.010
Veyhl, C., Belova, I. V., Murch, G. E., Öchsner, A., & Fiedler, T. (2010). On the mesh dependence of non-linear mechanical finite element analysis. *Finite Elements in Analysis and Design*, *46*(5), 371–378. https://doi.org/10.1016/j.finel.2009.12.003
Vinson. (1999). The Behavior of Sandwich Structure of Isotropic and Composite Materials.
W.-F. Chen and D.-J. Han. (2007). *Plasticity for Structure*. Florida.
W.F.Hosford. (1972). A Generalized Isotropic Yield Criterion. *Journal of Applied Mechanics*, *39*, 607–609.
Wang, B., Wang, R., & Wu, Y. (2009). The Young's moduli prediction of random distributed short-fiber-reinforced polypropylene foams using finite element method. *Science in China, Series E: Technological Sciences*, *52*(1), 72–78. https://doi.org/10.1007/s11431-008-0282-7
Wang, J. G., & Liu, G. R. (2002a). A point interpolation meshless method based on radial basis functions. *International Journal for Numerical Methods in Engineering*, *54*(11), 1623–1648. https://doi.org/10.1002/nme.489
Wang, J. G., & Liu, G. R. (2002b). On the optimal shape parameters of radial basis functions used for 2-D meshless methods. *Computer Methods in Applied Mechanics and Engineering*, *191*(23–24), 2611–2630. https://doi.org/10.1016/S0045-7825(01)00419-4
Warren, W. E., & Kraynik, A. M. (1997). Linear Elastic Behavior of a Low-Density Kelvin Foam With Open Cells. *Journal of Applied Mechanics*, *64*(4), 787. https://doi.org/10.1115/1.2788983
Xiao, S. P., & Belytschko, T. (2005). Material stability analysis of particle methods. *Advances in Computational Mathematics*, *23*(1–2), 171–190. https://doi.org/10.1007/s10444-004-1817-5
Xue, Z., & Hutchinson, J. W. (2006). Crush dynamics of square honeycomb sandwich cores. *International Journal for Numerical Methods in Engineering*, *65*(13), 2221–2245. https://doi.org/10.1002/nme.1535
Yang, G., Kabel, J., Van Rietbergen, B., Odgaard, A., Huiskes, R., & Cowin, S. C. (1998). Anisotropic Hooke's law for cancellous bone and wood. *Journal of Elasticity*, *53*(2), 125–146. https://doi.org/10.1023/A:1007575322693
Youssef, S., Maire, E., & Gaertner, R. (2005). Finite element modelling of the actual structure of cellular materials determined by X-ray tomography. *Acta Materialia*, *53*(3), 719–730. https://doi.org/10.1016/j.actamat.2004.10.024
Zhang, J., Lin, Z., Wong, A., Kikuchi, N., Li, V, C., Yee, A, F., & Nusholtz, G, S. (1997). Constitutive Modeling and Material Cliaracterization of Polymeric Foams. *Journal of Engineering Materials and Technology*, *119*(July 1997), 284–291.
Zhu, H., Hobdell, J. R., & Windle, A. H. (2000). EFFECTS OF CELL IRREGULARITY ON THE ELASTIC PROPERTIES OF OPEN-CELL FOAMS. *Acta Materialia*, *48*(4), 4893–4900. https://doi.org/10.1016/S0022-5096(00)00046-6
Zhu, H. X., Mills, N. J., & Knott, J. F. (1997). Analysis of the high strain compression of open-cell foams. *Journal of the Mechanics and Physics of Solids*, *45*(11–12), 1875–1904. https://doi.org/10.1016/S0022-5096(97)00027-6
Zhu, H. X., & Windle, A. H. (2002). Effects of cell irregularity on the high strain compression of open-cell foams. *Acta Materialia*, *50*(5), 1041–1052. https://doi.org/10.1016/S1359-6454(01)00402-5
Zienkiewicz, O. C., & Cheung, Y. K. (1967). *The finite element method in structural and continuum mechanics: numerical solution of problems in structural and continuum mechanics*. McGraw-Hill. Retrieved from https://books.google.pt/books?id=YJwoAQAAMAAJ
Zienkiewicz, O. C., & Taylor, R. L. (2000). The Finite Element Method Volume 1 : The Basis.

Methods, *1*, 708.
Ziennkiewicz, O. C., & Taylor, R. L. (2005). The finite element method for solid and structural mechanics. *Elsevier*, 631.

ANNEX 1: Cases of the study

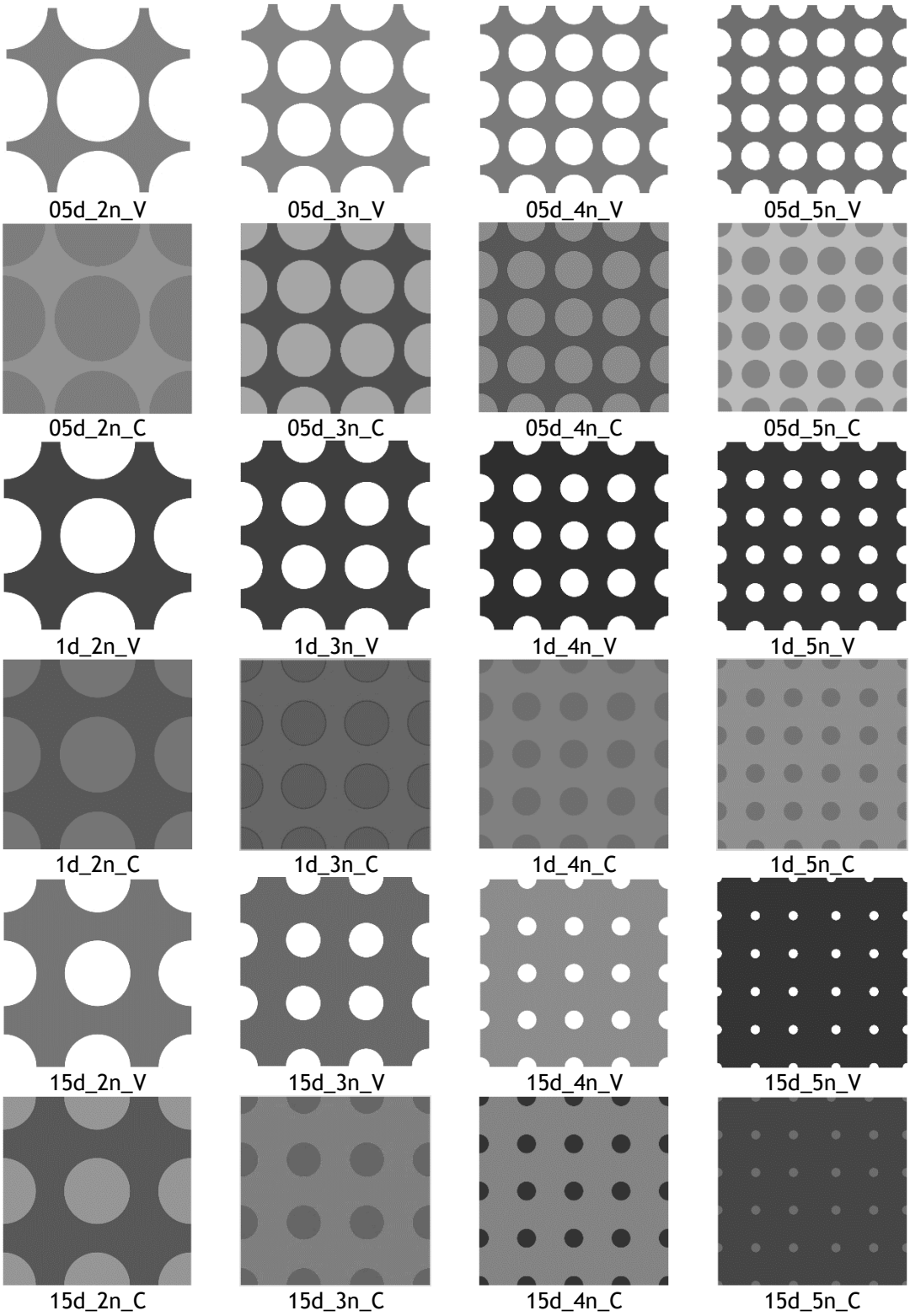

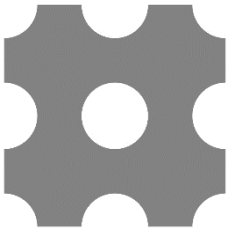

2d_2n_V

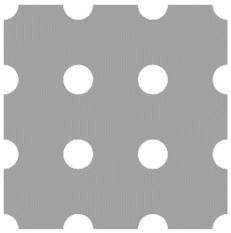

2d_3n_V

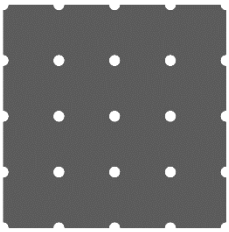

2d_4n_V

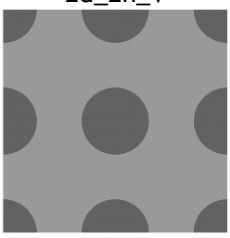

2d_2n_C

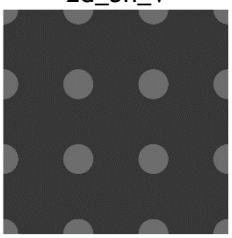

2d_3n_C

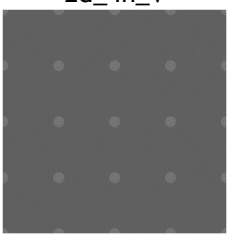

2d_4n_C

ANNEX 2: Elastoplastic graphics

Homogenised

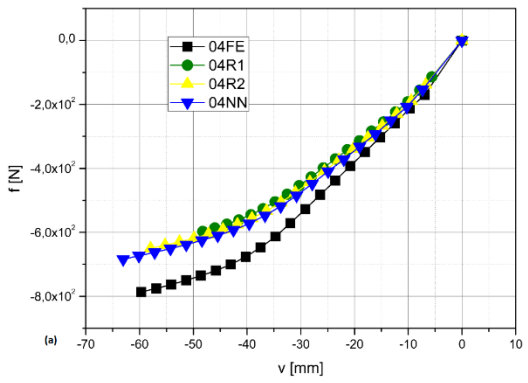

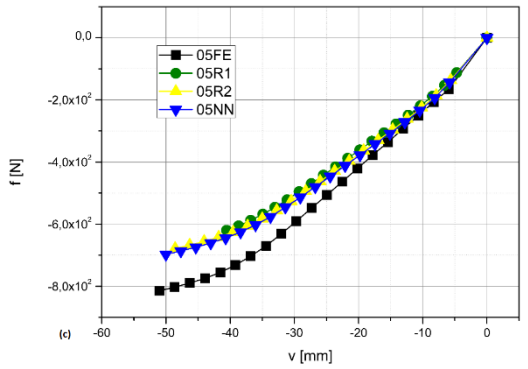

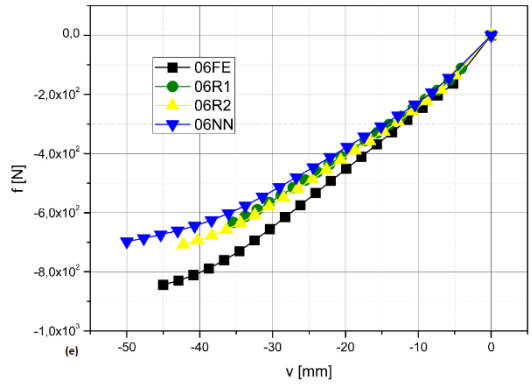

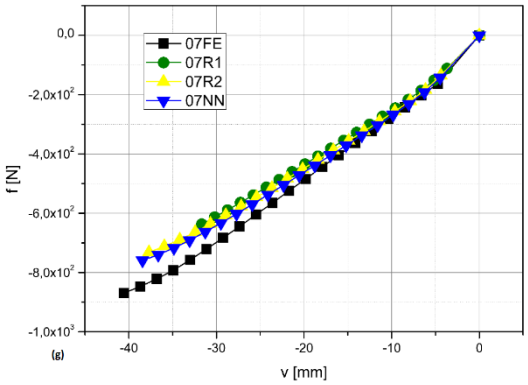

Interest Point

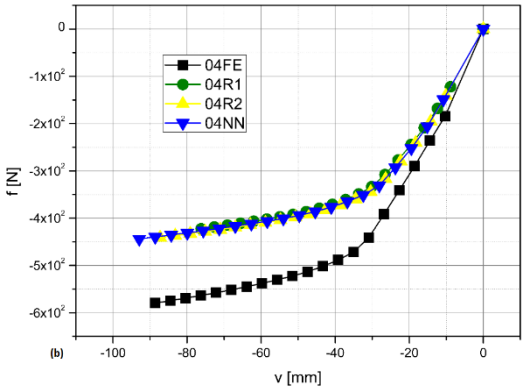

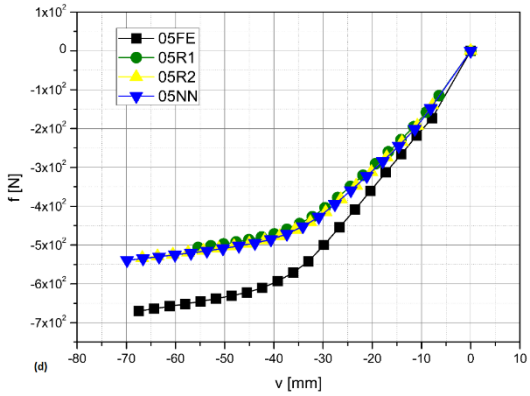

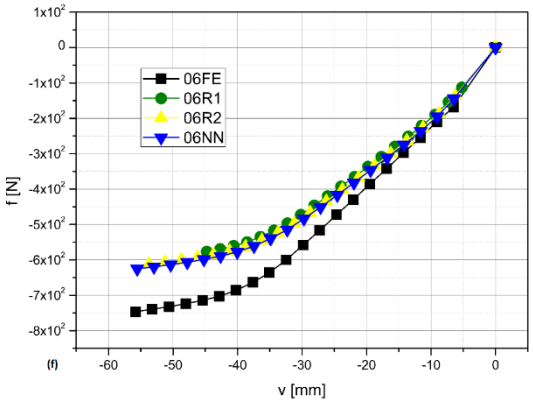

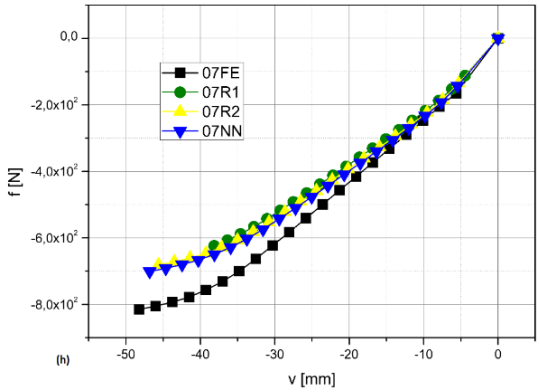

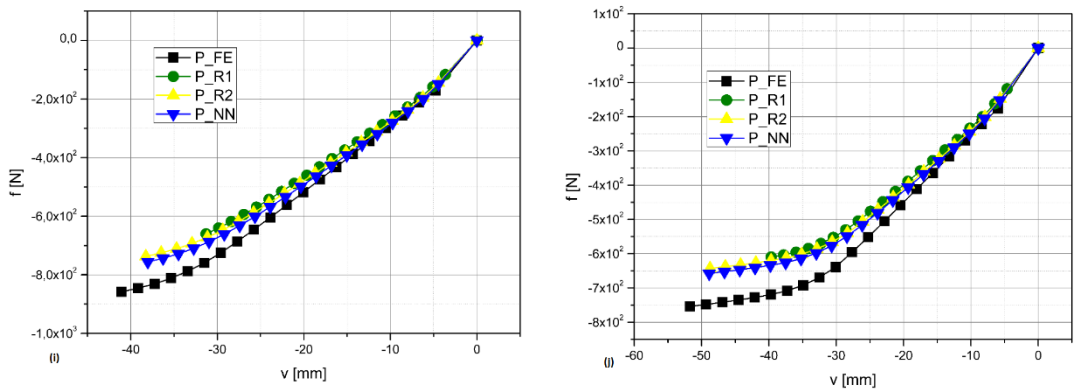

Figure 61 Comparison between the numerical method and the homogenous and interest point elastoplastic results for the values obtained increasing the maximum value imposed from four to eight and increase the number of increment from 15 to 20.

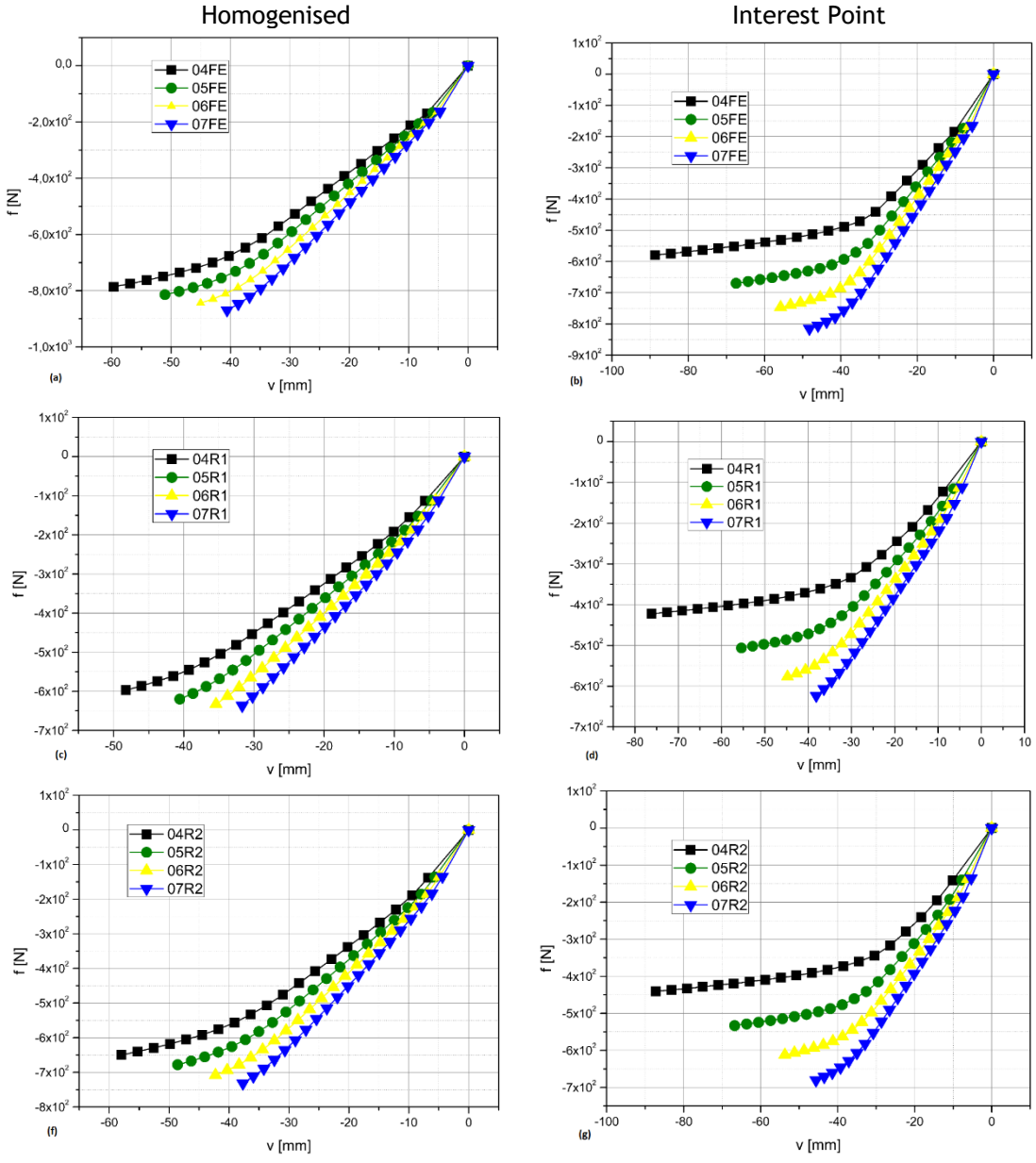

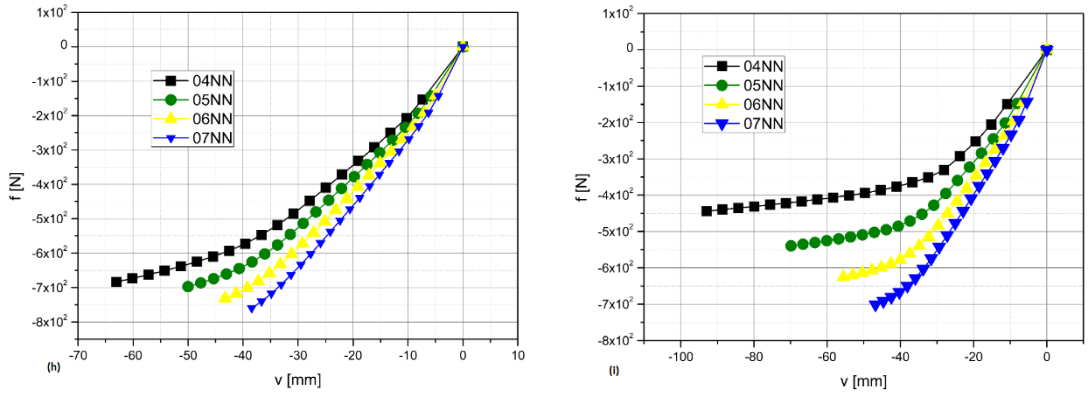

Figure 62 Comparison of the response in each numerical method when the relative density increase for the homogenous and interest point elastoplastic results.